

TWO DIMENSIONAL MODELING OF ELECTROMAGNETIC
RADIATION AND SCATTERING BY SPECTRAL ELEMENT METHOD

A THESIS SUBMITTED TO
THE GRADUATE SCHOOL OF NATURAL AND APPLIED SCIENCES
OF
MIDDLE EAST TECHNICAL UNIVERSITY

BY

IBRAHIM MAHARIQ

IN PARTIAL FULFILLMENT OF THE REQUIREMENTS
FOR
THE DEGREE OF DOCTOR OF PHILOSOPHY
IN
ENGINEERING SCIENCES

JULY 2014

Approval of the thesis:

**TWO DIMENSIONAL MODELING OF ELECTROMAGNETIC
RADIATION AND SCATTERING BY SPECTRAL ELEMENT METHOD**

Submitted by **IBRAHIM MAHARIQ** in partial fulfilment of the requirements for
the degree of **Doctor of Philosophy in Engineering Sciences, Middle East
Technical University** by,

Prof. Dr. Canan Özgen _____
Dean, Graduate School of **Natural and Applied Sciences**

Prof. Dr. Murat Dicleli _____
Head of Department, **Engineering Sciences**

Prof. Dr. Hakan I. Tarman _____
Supervisor, **Engineering Sciences Dept., METU**

Prof. Dr. Mustafa Kuzuoğlu _____
Co-Supervisor, **Electrical and Electronics Eng. Dept.,
METU**

Examining Committee Members:

Prof. Dr. Zülfü Aşık _____
Engineering Sciences Dept., METU

Prof. Dr. Hakan I. Tarman _____
Engineering Sciences Dept., METU

Prof. Dr. Gönül Sayan _____
Electrical and Electronics Engineering Dept., METU

Assoc. Prof. Dr. Hamza Kurt _____
Electrical and Electronics Engineering Dept., TOBB ETU

Assist. Prof. Dr. Cüneyt Sert _____
Mechanical Engineering Dept., METU

Date: 14 July 2014

I hereby declare that all information in this document has been obtained and presented in accordance with academic rules and ethical conduct. I also declare that, as required by these rules and conduct, I have fully cited and referenced all material and results that are not original to this work.

Name, Last Name: IBRAHIM MAHARIQ

Signature:

ABSTRACT

TWO DIMENSIONAL MODELING OF ELECTROMAGNETIC RADIATION AND SCATTERING BY SPECTRAL ELEMENT METHOD

MAHARIQ, Ibrahim

PhD, Department of Engineering Sciences

Supervisor: Prof. Dr. Hakan I. TARMAN

Co-Supervisor: Prof. Dr. Mustafa KUZUOĞLU

2014, 121 pages

In this thesis, the spectral element method is utilized in numerical modeling of two-dimensional, frequency-domain electromagnetic scattering and radiation problems. We perform domain truncation by the well-known perfectly matched layer (PML) and provide the corresponding formulation. The attenuation factor associated with the PML formulation is optimized so that the best accuracy is achieved for a wide range of Gauss-Legendre-Lobatto grids per wavelength. The optimality of the provided attenuation factor is verified by several numerical demonstrations and by comparing the numerical solutions with those obtained under the absence of PML in problems whose analytical solutions are available. Further, these values of attenuation are applied to solve electromagnetic scattering by dielectric micro cylinders (photonic nanojets). Some interesting cases that contribute to whispering gallery modes are reported where finite-difference time-domain method is found to fail in numerical modeling of such cases. In addition, the resulting linear system of equations is also approached iteratively and a comparison among successive over relaxation, Jacobi and incomplete LU preconditioners is presented.

Keywords: electromagnetic, scattering, radiation, spectral element method, perfectly matched layer, photonic nanojets.

ÖZ

SPEKTRAL ELEMENT METHODUYLA İKİ BOYUTLU ELEKTROMANYETİK RADYASYON VE SAÇILMA MODELLENMESİ

MAHARIQ, Ibrahim

PhD, Mühendislik Bilimleri Bölümü

Danışman: Prof. Dr. Hakan I. TARMAN

Yardımcı Danışman: Prof. Dr. Mustafa KUZUOĞLU

2014, 121 sayfa

Bu tezde, spektral elemanlar metodu iki boyutlu frekans bölgesi elektromanyetik yayılımı ve radyasyon problemlerinin modellenmesinde kullanılmıştır. Bölge kesme işlemini çok bilinen mükemmel uyumlu tabaka (PML) yöntemi ile yaparak ilgili formülasyon elde edilmiştir. PML formülasyonu ile ilintili azalma faktörü optimize edilmiş ve her bir dalgaboyu için geniş aralıklı Gauss-Legendre –Lobatto ağı için çok yüksek doğruluk elde edilmiştir. Sağlanan azalma faktörünün eniyilemesi, sayısal deneylerle ve analitik çözümü olmayan PML yöntemi uygulanmayan problemlerin sayısal çözümleriyle karşılaştırılarak kanıtlanmıştır. Bunun yanında, bu azalma faktörleri, dielektrik mikro silindirler (fotonik nanojetler) ile oluşmuş elektromanyetik dağılımın çözümünde kullanılmıştır. Bu çalışmada, sonlu-farklar zaman-alan metodu ile elde edilemeyen akustik galeri yöntemlerine katkıda bulunan bazı farklı durumlar da rapor edilmiştir. Ayrıca, elde edilen doğrusal denklem sistemleri; ardışık aşırı rahatlatma, Jacobi ve eksik LU önşartlandırıcı iteratif yöntemlerle çözülmüş ve karşılaştırılmıştır.

Anahtar Kalimeler: elektromanyetik, saçılma, radyasyon, spektral element metodu, mükemmel uyumlu tabaka, fotonik nanojetler.

Starting from elementary school up to this moment, I have been doing my best every year in order to have a distinct certificate, show it to my aged parents, and hear from them: “Well done, Ibrahim”.

Dedicated to my parents:

Mohammed Mahariq

Naima Mahariq

ACKNOWLEDGMENTS

First of all, I thank my God who gave me the ability and led me to do this work.

I am really indebted to my supervisor Prof. Dr. Hakan I. Tarman for his guidance, suggestions, criticism, encouragement during the time of research and writing of this thesis.

I would like to express my deepest gratitude to my co-supervisor Prof. Dr. Mustafa Kuzuođlu for his guidance, motivation, belief in my ability, and everlasting friendly attitude throughout the development of this thesis.

I would also like to express my sincere thanks to Assoc. Prof. Dr. Hamza Kurt for his guidance in some part of my thesis. In fact, in addition to being my teacher and my inspiration, I consider him as my best friend. I would like to thank Prof. Dr. Turgut Tokdemir and Assist. Prof. Dr. Cüneyt Sert for their evaluations and concerns during the development of this thesis. I also thank all committee members for their criticism.

I would like to express my special thanks to my Parents, Azhar Mahariq, Ahmed Mahariq, Labib Mahariq, Atheer Mahariq, my borthers and my sisters for their support, encouragement and giving me the time that I had to spend with them to accomplish this work.

Finally, I would like to thank Esra Tüzün, Assis. Prof. Dr. Ibrahim Arpacı, Zeynep Barcin, Bülent Körođlu and many other turkish friends for their help, encouragement, and friendship.

This study was partially supported by The Scientific and Technological Research Council of Turkey (TÜBİTAK).

TABLE OF CONTENTS

PLAGIARISM.....	i
ABSTRACT	iv
ÖZ.....	vi
ACKNOWLEDGMENTS	viii
TABLE OF CONTENTS	ix
LIST OF TABLES	xii
LIST OF FIGURES	xiii
LIST OF ABBREVIATIONS	xvi
CHAPTER	
1. INTRODUCTION.....	1
1.1 Electromagnetic Modeling	1
1.2 Literature Review	3
1.3 Contributions of this Thesis	8
1.4 Arrangement of this Thesis	9
2. ELECTROMAGNETIC SCATTERING/RADIATION AND DOMAIN TRUNCATION	11
2.1 Electromagnetic Scattering Problems	11
2.1.1 Perfect Electric Conducting Cylinders	12
2.1.2 Dielectric cylinders.....	15
2.2 Electromagnetic radiation.....	16
2.3 Domain truncation	18
2.4 Derivation of the Equations Governing the PML	21

2.5 Choices for the PML parameters	24
3. SPECTRAL ELEMENT FORMULATION OF ELECTROMAGNETIC SCATTERING/RADIATION PROBLEMS	29
3.1 Introduction	29
3.2 The governing PDEs.....	30
3.3 SEM formulation	33
3.4 SEM accuracy in a single-element domain	38
3.4.1 Elemental Deformation.....	38
3.4.2 Results	39
3.5 Conclusion	46
4. INVESTIGATION OF ITERATIVE METHODS	49
4.1 Resulting Matrix	49
4.2 Storage Schemes	50
4.3 An overview of Iterative Methods.....	51
4.4 Conjugate Gradient Method	52
4.5 Biconjugate Gradient Method	55
4.6 Preconditioned Conjugate Gradient Method	56
4.6.1 Jacobi Preconditioning	57
4.6.2 SSOR Preconditioning.....	58
4.6.3 ILU Factorization Preconditioners	60
4.7 Generalized Minimum Residual Method	62
4.7.1 Preconditioned Generalized Minimum Residual Method	63
4.8 Conclusion	65
5. APPLICATION OF SPECTRAL ELEMENT METHOD IN ELECTROMAGNETIC RADITION PROBLEMS.....	69
5.1 Introduction	69

5.2 Accuracy of SEM, FDM, and FEM	70
5.3 Determination of the Attenuation Factor.....	74
5.4 Scattering Cylinders	81
5.5 Scattering by Large Objects	87
5.6 One-dimensional problem	90
5.7 Conditioning of the System Matrix	91
5.8 Conclusion.....	96
6. PHOTONIC NANOJET ANALYSIS	97
6.1 What is a Photonic Nanojet?	97
6.2 Numerical Analysis of Photonic Nanojets	98
6.3 Nanojet Analysis by Spectral Element Method	101
6.4 Verification of Whispering Gallery Modes.....	109
6.5 Conclusions	113
7. CONCLUSIONS	115
REFERENCES	119
VITA	123

LIST OF TABLES

Table 3. 1 Relative errors vs N for the reference element and the rectangular elemt	41
Table 3. 2 Errors for Quadrilateral element with straight sides and unit area.....	44
Table 3. 3 Errors for Quadrilateral element with curved side and unit area.	45
Table 4. 1 Errors obtained by Jacobi preconditioner.	68
Table 5. 1 Relative errors of SEM and FDM for the problem defined in (5.1).....	71
Table 5. 2 Errors of SEM and FEM for the problem defined in (5.3).....	72
Table 5. 3 Errors of FEM for of the 2D point source problem.	73
Table 5. 4 Maximum relative errors as obtained by SEM for the problem.....	78
Table 5. 5 Maximum relative errors obtained by SEM for the 2D Green's function problem with circular inner boundary.	80
Table 5. 6 SEM errors for the scattering circular cylinder.....	82
Table 5. 7 Maximum relative errors at four positions.....	89
Table 5. 8 The average of relative errors of the 21 positions.....	89
Table 5. 9 The maximum relative error of the one-dimensional problem.	90
Table 5. 10 Condition number of 2D FEM and SEM matrices.....	92
Table 5. 11 Condition number of SEM with and without PML in 2D.....	93
Table 5. 12 Condition number of SEM with and without PML in 1D.....	93
Table 5. 13 Condition number of FDM with and without PML in 1D.	94

LIST OF FIGURES

Figure 2. 1 Scattering by a perfectly conducting cylinder	14
Figure 2. 2 General schematic of the radiation problem.....	17
Figure 2. 3 Schematic of a typical wave-equation problem.....	19
Figure 2. 4 Schematic of a typical wave-equation problem surrounded by PML.	21
Figure 2. 5 The interface between Ω and Ω_{PML}	22
Figure 2. 6 The corner interface between Ω and Ω_{PML}	24
Figure 2. 7 Decaying the field in x-direction using multiple PML layers.	25
Figure 3. 1 A typical electromagnetic scattering problem composed of a dielectric scatterer (Ω_{SC}) embedded in a free-space Ω_{FS} , and domain truncation is performed by the perfectly matched layer Ω_{PML}	33
Figure 3. 2 Mapping an element Ω^e to the standard element Ω^{st}	35
Figure 3. 3 GLL grid nodes on the reference element for a ninth-order polynomial space (nodes are represented by the intersections of horizontal and vertical lines). .	37
Figure 3. 4 Plot of first six Legendre polynomials.	38
Figure 3. 5 Various quadrilateral elements.	39
Figure 3. 6 The reference square element with unit area.	40
Figure 3. 7 Real part of the solution in the reference element at $N=18$	41
Figure 3. 8 Quadrilateral element with straight sides and unit area.....	42
Figure 3. 9 SEM solution for the straight-sided quadrilateral element at $AR = 1.33$..	42
Figure 3. 10 SEM solution for the straight-sided quadrilateral element $AR = 1.88$.	43
Figure 3. 11 SEM solution for the straight-sided quadrilateral element $AR = 2.87$..	43
Figure 3. 12 Quadrilateral element having one curved side and a unit area.	44
Figure 3. 13 SEM solution for the curved-sided quadrilateral element $AR = 1.39$..	46
Figure 3. 14 SEM solution for the curved-sided quadrilateral element $AR = 2.39$...	46
Figure 4. 1 Conjugate Gradient method: Residual versus number of iterations.....	54
Figure 4. 2 Biconjugate Gradient method: Residual versus number of iterations.	56

Figure 4. 3 Preconditioned Conjugate Gradient method: Residual versus number of iterations.....	58
Figure 4. 4 SSOR preconditioner: Residual versus number of iterations.	59
Figure 4. 5 ILU(0) preconditioner: Residual versus number of iterations.	61
Figure 4. 6 GMRES: Residual versus number of iterations.	63
Figure 4. 7 Preconditioned GMRES: Residual versus number of iterations.....	64
Figure 4. 8 GMRES method and the Conjugate Gradient method.....	65
Figure 4. 9 Preconditioned Conjugate Gradient and Biconjugate Gradient methods.....	66
Figure 4. 10 Preconditioned Conjugate Gradient and GMRES methods.....	66
Figure 5. 1 Exact and SEM solutions of the problem (5.3).....	72
Figure 5. 2 FEM solution of the 2D point source problem (Grid: 20×20).	74
Figure 5. 3 The computational domain definition without PML.	76
Figure 5. 4 The computational domain definition with PML.	76
Figure 5. 5 The problem of the 2D Green's function: (a) the problem definition, (b) elements in SEM.	77
Figure 5. 6 Variation of SEM error vs α at $N=11$	79
Figure 5. 7 The problem of the 2D Green's function having a circular inner boundary: (a) the problem definition, (b) elements in SEM.	80
Figure 5. 8 The real part of SEM solution of the problem defined in figure 5.7.	81
Figure 5. 9 Magnitude of the scattered field by the cylinder (i.e., $ u $).	82
Figure 5. 10 Real part of the total electric field near the cylinder at $r_c = 0.8\lambda$	83
Figure 5. 11 A plane wave incident to a square cylinder of radius R	84
Figure 5. 12 Elemental discretization in SEM for the square cylinder problem.....	84
Figure 5. 13 The total field at $R = 0.5\lambda$ due to x-propagating plane wave.....	85
Figure 5. 14 The total field at $R = 1.5\lambda$ due to x-propagating plane wave.....	85
Figure 5. 15 The total field at $R = 0.5\lambda$ due to xy-propagating plane wave.....	86
Figure 5. 16 he total field at $R = 1.5\lambda$ due to xy-propagating plane wave.	86
Figure 5. 17 Scattering by large objects: (on the left) the computational domain, selected positions for the point source (on the right).	87
Figure 5. 18 Plot of $ u $ for position-16 at $N \times N = 11 \times 11$	88
Figure 5. 19 Real part of the exact and SEM solution at $N=18$	91

Figure 5. 20 Imaginary part of the exact and SEM solution at $N=18$.	91
Figure 5. 21 Imaginary part of FDM solution at $N=100$ in each subdomain.	95
Figure 5. 22 Imaginary part of FDM solution at $N=100$ in each subdomain.	95
Figure 6. 1 Experimental observation of a photonic nanojet viewed along the optical axis of a $5 \mu\text{m}$ -diameter dielectric sphere made of glass.	100
Figure 6. 2 Visualization of a photonic nanojet of a plane-wave-illuminated circular dielectric cylinder of $5 \mu\text{m}$ diameter and has a refractive index of 1.7. [15].	100
Figure 6. 3 Definition of the computational domain composed of a dielectric cylinder (Ω_C) embedded in the free space (Ω_{FS}) and truncated by PML.	102
Figure 6. 4 A possible discretization of the computational domain at $R = 1.5\lambda$, and $N \times N = 9 \times 9$ for each element (here, only elements corresponding to Ω_{FS} and Ω_C are shown).	103
Figure 6. 5 Visualization of photonic nanojet at $R = 3.5\lambda$ and $n = 1.6$.	104
Figure 6. 6 3D visualization of photonic nanojet at $R = 3.5\lambda$ and $n = 1.6$.	105
Figure 6. 7 Visualization of photonic nanojet at $R = 5\lambda$ and $n = 1.6$.	105
Figure 6. 8 Visualization of photonic nanojet at $R = 6.5\lambda$ and $n = 1.4$.	106
Figure 6. 9 Visualization of the evolution of a photonic nanojet for $R = 3.50\lambda$ and $n = 1.7$. WGM representation gives $m=28$ and $I = 2$.	107
Figure 6. 10 Visualization of the evolution of a photonic nanojet for $R = 4.50\lambda$ and $n = 2$. WGM parameters are $m=34$ and $I = 4$.	108
Figure 6. 11 FDTD visualization of the evolution of a photonic nanojet for $R = 3.50\lambda$ and $n = 1.7$.	109
Figure 6. 12 Magnitude of magnetic scattered-incident field inside the cylinder for $R = 4\lambda$ and $n = 1.4$. as obtained by Mie theory.	111
Figure 6. 13 The magnitude of the total magnetic field inside the cylinder at $R = 3.5\lambda$ and $n = 1.6905$.	112
Figure 6. 14 The magnitude of the total magnetic field inside the cylinder at $R = 4.5\lambda$ and $n = 1.8911$.	112

LIST OF ABBREVIATIONS

1D	: One Dimension
2D	: Two Dimension
ABC	: Absorbing Boundary Condition
AR	: Aspect Ratio
BC	: Boundary Condition
BiCG	: BiConjugate Gradient
CG	: Conjugate Gradient
CGNE	: Conjugate Gradient on the Normal Equations
CGS	: Conjugate Gradient Squared
CPU	: Central Processing Unit
EM	: Electromagnetics
FEM	: Finite Element Method
FDM	: Finite Difference Method
FDTD	: Finite Difference Time Domain
FWHM	: Full Width at Half Maximum
GLL	: Gauss-Legendre-Lobatto
GMRES	: Generalized Minimum Residual
ILU	: Incomplete LU
LU	: Lower/Upper Triangular
MINRES	: Minimum Residual
PEC	: Perfect Electric Conducting
PDE	: Partial Differential Equation
PML	: Perfectly Matched Layer
QMR	: Quasi Minimal Residual
SEM	: Spectral Element Method
SSOR	: Symmetric Successive Overrelaxation
TE	: Transverse Electric
TM	: Transverse Magnetic
WGM	: Whispering Gallery Mode

CHAPTER 1

INTRODUCTION

1.1 Electromagnetic Modeling

Electromagnetic phenomena are governed by the following fundamental laws in physics:

- Gauss's law for electricity,
- Gauss's law for magnetism,
- Faradays's law of induction, and
- Ampere's circuital law.

Human beings should acknowledge and not forget the Scottish physicist and mathematician James Clerk Maxwell (1831-1879), who combined these laws into a set of partial differential equations, known as Maxwell's equations. Maxwell didn't only simplify and reformulate these laws, but also he added another term to the differential equation corresponding to Ampere's circuital law. This addition was the historical step that brought humanity to the technology that we enjoy nowadays. It was the prediction of existence of electromagnetic waves.

Engineers and scientists use several approaches in analyzing electromagnetic phenomena that are governed by Maxwell's equations. These approaches can be mainly classified as experimental, analytical, or numerical. Being hazardous sometimes, expensive or time consuming, experimental techniques are not preferable. The latter two approaches, on the other hand, are convenient to use in electromagnetic modeling.

Analytical methods are mainly separation of variables, series expansion, conformal mapping, integral solutions (as Laplace and Fourier transforms), and perturbation

methods. The connection between analytical methods and numerical methods is very strong from the sense that numerical methods involve analytic simplification to the point where it is easy to apply a specific numerical method. However, in general, obtaining the analytical solution is very difficult. This difficulty in analytical methods leaves the numerical methods as the only convenient methods for engineers.

Numerical methods are inter-related to each other and they give an approximate solution with a sufficient accuracy for engineering purposes. The most common numerical methods in electromagnetic modeling are [1]:

- a. Finite difference method
- b. Method of weighted residuals
- c. Method of moments
- d. Finite element method
- e. Transmission-line modeling
- f. Monte Carlo method
- g. Method of lines

The necessity for the application of numerical methods is best expressed by Paris and Hurd: “Most problems that can be solved formally (analytically) have been solved” [2]. In fact, until 1940s, most of electromagnetic problems that involve simplicity were solved by analytical methods, mainly by separation of variables and integral equation methods. In addition, a lot of effort was given to extend the application of these methods to a narrow range of practical problems. However, complexity in geometries associated with the most realistic problems was the main reason behind developing numerical methods that can be easily performed by computing machines.

In parallel to the development of high-speed digital computers during 1960s, numerical solutions of electromagnetic problems attracted the attention of electrical engineers [1]. This is due to the fact that the computers can numerically solve very complex and realistic problems, whose analytical solutions are impossible to find.

Moreover, the numerical approach allows the actual work to be performed without requiring the operator to be of high level in mathematics or physics.

Another classification of electromagnetic problems is based on the domain in which the solution is sought; that is, frequency domain and time domain. For each domain, modeling differential equations or integral equations can be utilized. Throughout this thesis, differential equations in frequency domain are used.

Spectral element method (SEM) has been recently applied to electromagnetic problems [7]-[12] and attracted the attention of computational electromagnetic community. The attraction of this method is mainly due to the accuracy achieved for much less degrees of freedom. In the next section, we explore the literature review regarding the application of SEM and PML in modeling the electromagnetic problems.

1.2 Literature Review

Generally speaking, computational methods in the numerical modeling of electromagnetic scattering and radiation problems are either based on the direct discretization of the governing partial differential equations, or on the discretization of the integral equations which reformulate the associated boundary value problems [3]. However, most of the electromagnetic problems occur in unbounded spatial domain. Hence, in order to truncate the computational domain, Absorbing Boundary Conditions (ABCs) had been extensively used in the past (before mid-1990s). Berenger [4] provided a new approach for domain truncation and called it Perfectly Matched Layer (PML).

Mustafa and Mittra [3] studied this new approach extensively. They provided a derivation for the PML, that leads to three different perfectly matched layer realizations; namely, the split-field formulation which is the original work introduced by Berenger [4], the anisotropic PML [5], and the bianisotropic PML [6]. The

derivation introduced by Mustafa and Mittra is utilized in this work with a slight change associated with the attenuation of the field in two-dimensional, frequency-domain electromagnetic scattering problems.

Several numerical methods have been extensively utilized in modeling the electromagnetic scattering and/or radiation phenomena. However, SEM was not used extensively as its counter parts such as finite element method or finite difference method. Several years ago, the computational electromagnetic community turned their attention to this method. Moreover, there was not many studies using SEM together with PML concept.

In 1983, Charles W. Steele [7] tried to apply spectral methods for field computation. In that work, a method for computing magnetic and electric fields is presented by expressing the field as a linear combination of orthogonal basis functions. He showed that this method is superior to the traditional finite element method in terms of the computational cost for certain configurations. However, in practice, electrical machines have complex geometries and this complexity makes it impossible to apply spectral methods that is suitable for basic geometries shapes such as rectangular and circular.

One of the first attempts in numerical modeling of two-dimensional electromagnetic problems by spectral element method was carried out by Mehdizadeh and Parashivoiu [8], in 2003. They proposed a spectral element formulation for solving the two-dimensional Helmholtz's equation, which is the equation governing time-harmonic acoustic waves. The motivation of their work was to reduce the pollution effect that increases the computational cost of Galerkin finite element method as the wave number increases. They also demonstrated a comparison between spectral element method and second-order finite element method and showed that spectral element method leads to fewer grid points per wavelength and less computational cost for the same accuracy. For unbounded problems, they utilized the symmetric perfectly matched layer as an approach for domain truncation.

In 2006, Lee et al. [9] proposed a three-dimensional spectral element method based on Legendre polynomials as the basis functions to solve vector electromagnetic-wave equations. The proposed method led to reducing the computer memory requirement and CPU time in comparison with the conventional high-order finite element method. However, they presented their work in the absence of the perfectly matched layer.

There is also a high potential behind using spectral element method as a better alternative method than the most commonly used methods for solving electromagnetic problems in time domain. For instance, Lee and Liu [10], proposed a spectral element time-domain method to solve three-dimensional transient electromagnetic problems. They showed that the proposed method requires only a trivial sparse matrix-vector product at each time step; hence, reducing CPU time and memory requirement significantly. The perfectly matched layer is used in their work to truncate unbounded domains. In addition, they demonstrated the efficiency and the spectral accuracy by numerical examples. Chen et al. [12] presented a high-precision time integration method for spectral elements to solve time-dependent Maxwell's equations. They demonstrated using some numerical examples on the accuracy and efficiency of the proposed method where the spatial discretization by spectral element method leads to block diagonal mass matrices. Again, they employed the perfectly matched layer for open-region problems in time domain. In 2009, a discontinuous spectral element time-domain method was proposed by Lee et al. [11] to solve transient electromagnetic fields in three-dimensional structures. They employed Riemann solvers in the boundary integral terms in order to guarantee continuity between the boundary fields. They also employed the perfectly matched layer to truncate the computational domain.

The investigations on the performance of iterative methods when spectral element method is used in numerical modeling of electromagnetic problems in frequency domain are not extensive. Botros and Volakis [13] reported an enhanced

convergence speed achieved by using an approximate preconditioner. However, an additional optimization problem is required to be solved, that can be time-consuming. Mehdizadeh and Parashivoiu [8] investigated the performance of spectral element method when used in electromagnetic modeling; however, although they pointed to the importance of investigating the performance of iterative solvers when using SEM, no investigation was carried out in their work.

In a recent study (2012), Shin et al. [14] showed the performance of solvers utilized to solve frequency-domain Maxwell's equations is greatly affected by the type of the perfectly matched layer used. In particular, they used stretched-coordinate perfectly matched layer. By the aid of numerical examples, they showed that this PML formulation results in fast convergence together with a particular diagonal preconditioner that holds for finite-element method discretization.

It is more an art experience than a science to know how to optimally place and size the mesh in the finite element method (FEM). In fact, experience taught us to have more elements in the physical domain where functions change rapidly and less elements where low gradients are expected. Mesh generation may take several trials before achieving a good mesh distribution [30]. On the other hand, the complexity in the physical domain itself may add additional limitations on mesh generation.

In FEM, ranges of the elemental aspect ratio of generated mesh have been investigated extensively and for wide variety of problems. As an example, but not restricted to, M. Picasso [31] proposed an adaptive algorithm for solving the Stokes problem with finite elements and meshes with high aspect ratios. In that paper, the effect of the aspect ratio on the results is discussed in details and some examples are presented for a non-acceptable mesh that can deteriorate the accuracy. V. Prachitham et al. [32] presented a two-dimensional adaptive method with large aspect ratio finite elements for the numerical simulation of mixed electroosmotic microflows. In their work, the refinement/ coarsening criterion is based on a posteriori error estimates. On the other hand, spectral element method (SEM) has the flexibility of using larger elemental aspect ratio without significant deterioration in

accuracy. S. Dong et al. [33] proposed a parallel SEM for dynamic three-dimensional nonlinear elasticity problems that provides a tolerant large elemental aspect ratio employing Jacobi polynomial-based shape functions, as an alternative to the typical Legendre polynomial-based shape functions in solid mechanics. D. Rh. Gwynllwy et al. [34] proposed an iterative method for moving SEM applied to the journal bearing problem where they investigated the results of extremely large physical aspect ratio.

However, the effect of elemental aspect ratio on accuracy has not been investigated in numerical modeling of electromagnetic radiation and/or scattering problems when SEM is utilized. Thus, the goal in this section is to investigate how much deterioration in the solution accuracy is obtained at different values of elemental aspect ratio in two-dimensional electromagnetic scattering problems. This investigation may shed some light on how to accurately mesh the physical domain using SEM. In contrast to FEM, elements in SEM are discretized by Gauss-Legendre-Lobatto grid; i.e., once the computational domain is discretized into elements by SEM, the nodal distribution within those elements can't be changed.

Finally, a phenomenon of electromagnetic scattering by a dielectric object known as photonic nanojets is heavily investigated by finite-difference time-domain method (FDTD). For instance, [15] and [16] provided a complete analysis for photonic nanojets using FDTD. They discussed light focusing and back scattered light by dielectric microspheres and micro-cylinders. Scattering by a dielectric object of cylindrical shape involves an infinite domain, hence; it is worthy to solve such a problem that is truncated by the perfectly matched layer with the optimized associated parameters provided in this work. In another word, this phenomenon is a typical example of an electromagnetic scattering problem where the region of interest composed of not only the free space but also a material whose relative permittivity is different from one.

1.3 Contributions of this Thesis

In this thesis we apply spectral element method for two-dimensional frequency-domain electromagnetic scattering and radiation problems. The main contributions of this work can be summarized in the following points:

1. The formulation of spectral element method for electromagnetic problems involving truncation by perfectly matched layers and dielectric scatterers is provided.
2. The accuracy of spectral element method is demonstrated and compared with finite element and finite difference methods in one and two dimensions. In addition, the elemental deformation and its effect on the accuracy are investigated.
3. Within the formulation of the perfectly matched layer provided in this work, the corresponding optimum values of the attenuating factors per wavelength are provided in the context of spectral element method.
4. Scattering by dielectric micro cylinders (that produces photonic nano jets) is investigated and compared with other work in literature.
5. Capturing whispering gallery modes in scattering dielectric cylinders at specific dimensions and material types is demonstrated in this work. This kind of resonance has not been reported in the literature by other numerical methods to the best of knowledge.
6. An investigation and comparison of the well-known iterative methods and preconditioners are also included in this work.
7. A comparison among the linear systems of equations obtained by using finite element, finite difference and spectral element methods is carried out and reported in this work using the optimum parameters associated with the perfectly matched layer.

Most of the work provided in this thesis is based on the following:

- I. Mahariq, H. I. Tarman, and M. Kuzuoğlu, "On the Accuracy of Spectral Element Method in Electromagnetic Scattering Problems," International

Journal of Computer Theory and Engineering vol. 6, no. 6, pp. 495-499, 2014.

- I. Mahariq, M. Kuzuoğlu, and H. I. Tarman, “On the Attenuation of Perfectly Matched Layer in Electromagnetic Scattering Problems with Spectral Element Method”, Applied Computational Electromagnetic Society Journal, under review.
- I. Mahariq, H. Kurt, H. I. Tarman, and M. Kuzuoğlu, “Photonic Nanojet Analysis by Spectral Element Method”, IEEE Photonics Journal, reviewed, and waiting for decision.

1.4 Arrangement of this Thesis

The flow of the thesis content is arranged as follows:

- Chapter 2 provides the formulation of the perfectly matched layer and discusses the choice of the corresponding parameters. It also presents the partial differential equations that govern free space, electromagnetic radiation and dielectric objects.
- Chapter 3 provides the formulation of spectral element method in 2D frequency-domain electromagnetic problems involving dielectric scatterers, free space, and perfectly matched layers. In addition, the effect of elemental deformation on the accuracy of spectral element method is illustrated.
- Chapter 4 investigates iterative solvers: conjugate gradient method, biconjugate gradient method, generalized minimum residual method and symmetric successive over relaxation, with several preconditioners: Jacobi preconditioner, successive over relaxation preconditioner, and incomplete LU factorization preconditioner.
- Chapter 5 presents and discusses the choice the parameters defining the perfectly matched layer and demonstrates the accuracy of spectral element method based on these choices. In addition, scattering by perfectly conducting circular cylinders and perfectly conducting square cylinders is illustrated. Also, the accuracy of spectral element method when applied in

scattering by electrically large objects whose permittivity and/or permeability are different from that of free space is estimated in this chapter.

- Chapter 6 applies the spectral element method in scattering by dielectric micro cylinders. Results of photonic nanojets are illustrated and discussed. Moreover, this chapter discusses some special cases that are different from the expected photonic nanojets.
- Chapter 7 draws conclusions and future work.

CHAPTER 2

ELECTROMAGNETIC SCATTERING/RADIATION AND DOMAIN TRUNCATION

In this chapter, an overview to electromagnetic scattering and radiation is presented in two dimensions. Subsequently, domain truncation by perfectly matched layer is discussed and the corresponding partial differential equations are derived. At the end of this chapter, perfectly matched layer in electromagnetic modeling is optimized in the context of spectral element method. The optimality is demonstrated by physical reasoning and further discussed numerically in chapter 5.

2.1 Electromagnetic Scattering Problems

In cases when an electromagnetic wave encounters a target which is a metallic object, this wave causes current excitation on the target. The excited currents are oscillatory in nature and that oscillation in turn causes radiation. That is; the process in which radiation from an object takes place due to an incident electromagnetic wave is called electromagnetic scattering. Radar applications and multi-path analysis for radio-wave propagation are typical examples of this process.

Because of linearity in the Maxwell equations, the fields can be decomposed into an incident field E^{inc} and a scattered field E^s . The total field E^{tot} , is then expressed as [17]:

$$E^{tot} = E^{inc} + E^s \quad (2.1)$$

By other words, the total field is simply defined as the sum of the incident wave in the absence of the scatterer, and the scattered field caused by the scatterer in the

absence of any incident fields. This decomposition is mathematically very useful when studying scattering by objects. In this thesis, we considered the objects to be infinitely long cylinders as explained in the following subsection.

In the two-dimensional scattering problems, transverse magnetic mode (TMz) is considered. In TMz mode, the following field components exist: $E_z(x, y)$, $H_x(x, y)$ and $H_y(x, y)$, where E and H represent the electric field and magnetic field, respectively. Based on this mode, we considered two cases; the first case is scattering by an infinitely-long perfect electric conducting cylinder, and the second is scattering by a transparent dielectric cylinder.

In the following two subsections, the partial differential equations governing the field in the space surrounding the cylinder and in the dielectric cylinder itself are formulated. In addition, the derivation of the analytical solution of the field scattered by perfect electric conducting cylinders is provided.

It should be noted that throughout our work, we assume an incident plane wave with suppressed time dependence $exp(j\omega t)$, in which ω stands for the angular frequency.

2.1.1 Perfect Electric Conducting Cylinders

Here is considered a specific case where the cylinder has the following properties:

- It is infinitely long in z-axis, and along this axis, its geometry and boundary conditions don't vary.
- It is perfect electric conducting cylinder (PEC), meaning that it has infinitely large conductivity.
- It has constant radius.

Either in transverse magnetic (TMz) or in transverse electric (TEz) mode the field can be decomposed into scattered field and incident field. For the case where the

scatterer is subjected to a TMz plane wave, the source-free Maxwell's equations must be satisfied:

$$\nabla \times \vec{E} = -j\omega\mu_0\mu_r\vec{H} \quad (2.2)$$

$$\nabla \times \vec{H} = j\omega\varepsilon_0\varepsilon_r\vec{E} \quad (2.3)$$

in which j is the imaginary unit, ω is the angular frequency, \times represents curl operator, μ_0 and ε_0 are the permeability and permittivity of free-space, respectively, and, μ_r and ε_r are the relative permeability and permittivity of the scatterer, respectively. The scalar Helmholtz equation for TMz mode in two-dimensional free-space region can be obtained by combining the above two equations and eliminating the magnetic field (and setting $\mu_r = \varepsilon_r = 1$):

$$\nabla^2 E_z^s + k^2 E_z^s = 0 \quad (2.4)$$

where ∇^2 stands for Laplacian operator, and $k = \omega\sqrt{\mu_0\varepsilon_0}$ is the wave number.

The derivation of the analytical solution of the scattered field is straight forward. If a plane wave of the form:

$$E_z^{inc} = E_0 e^{jkx} \quad (2.5)$$

is incident on an infinitely-long conducting cylinder of radius R and centered in the origin of xy -coordinates as shown in figure 2.1, then for sake of convenience, we need to express the plane wave as:

$$E_0 e^{jkx} = E_0 e^{jk\rho\cos\phi} = E_0 \sum_{n=-\infty}^{\infty} b_n J_n(k\rho) e^{jn\phi} \quad (2.6)$$

where b_n are coefficients of the expansion, J_n are Bessel functions of the first kind of order n , ρ is the radial distance from the z-axis to a point, P , and ϕ is the angle between x-axis and the line from the origin to P .

The orthogonality property of the functions $e^{jn\phi}$ when $0 \leq \phi \leq 2\pi$, is utilized by multiplying equation (2.6) by $e^{jm\phi}$. Integration over $0 \leq \phi \leq 2\pi$ gives (drop the constant k) [1]:

$$\int_0^{2\pi} e^{-j\rho\cos\phi} e^{jm\phi} d\phi = 2\pi b_m J_m(\rho) \quad (2.7)$$

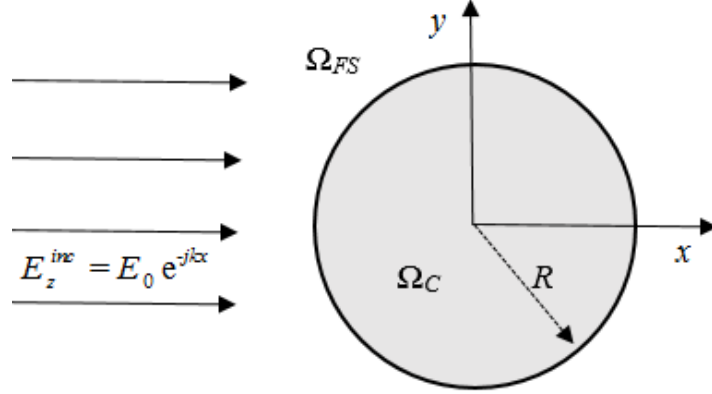


Figure 2. 1 Scattering by a perfectly conducting cylinder

By taking the m^{th} derivative of both sides of equation (2.7) with respect to ρ and evaluating at $\rho=0$, one can then obtain:

$$2\pi \frac{j^{-m}}{2^m} = 2\pi b_m \frac{1}{2^m} \rightarrow b_m = j^{-m} \quad (2.8)$$

By substituting this into equation (2.6), the incident wave can then be expressed as:

$$E_0 e^{jkx} = E_0 e^{jk\rho\cos\phi} = E_0 \sum_{n=-\infty}^{\infty} (-j)^n J_n(k\rho) e^{jn\phi} \quad (2.9)$$

But the scattered field E_z^s , must vanish at infinity. This means that the outgoing waves must have:

$$J_n(k\rho) - jY_n(k\rho) = H_n^{(2)}(k\rho) \quad (2.10)$$

where $H_n^{(2)}$ are Hankel functions of the second kind of the n^{th} order and Y_n is the Bessel function of the second kind. Thus, the scattered field is expressed as:

$$E_z^s = \sum_{n=-\infty}^{\infty} B_n H_n^{(2)}(k\rho) e^{jn\phi} \quad (2.11)$$

The total field in Ω_{FS} is expressed as in equation (2.1). While in Ω_C , the field is simply zero since the cylinder is a perfect conductor. At the boundary, i.e., at $\rho = R$, the tangential components of both fields must be equal. In another word, the total field at $\rho = R$ is equal to zero, i.e.,

$$E_z^{inc}(\rho = R) + E_z^s(\rho = R) = 0. \quad (2.12)$$

If we substitute equations (2.9) and (2.11) into equation (2.12), we obtain:

$$\sum_{n=-\infty}^{\infty} (B_n H_n^{(2)}(kR) + E_0 (-j)^n J_n(kR)) e^{jn\phi} = 0 \quad (2.13)$$

From this, the expansion coefficients B_n , are found to be:

$$B_n = -\frac{(-j)^n E_0 J_n(kR)}{H_n^{(2)}(kR)} \quad (2.14)$$

Substituting this into equation (2.11), the scattered field is finally obtained:

$$E_z^s = -E_0 \sum_{n=-\infty}^{\infty} \frac{(-j)^n J_n(kR)}{H_n^{(2)}(kR)} H_n^{(2)}(k\rho) e^{jn\phi} \quad (2.15)$$

It is important to mention that this solution is expressed in infinite summation of Hankel and Bessel functions. However, truncation of this summation at $n = -120 \rightarrow 120$ is tested and guarantees convergence. It is taken as $n = -180 \rightarrow 180$ in this thesis in order to avoid any error that may affect the results when comparing the numerical solutions with the analytical solutions.

2.1.2 Dielectric cylinders

In the previous subsection, the perfectly conducting cylinder is discussed. There, the induced currents in the scatterer (cylinder) exist only on the surface enclosing it, i.e., in $\partial\Omega_C$ only. However, in dielectric scatterers, the situation is different. The currents are induced everywhere inside the scatterer and their values depends on the spatial position and the characteristics of the incident plane wave (polarization, propagation direction, magnitudes, etc.).

Replacing the PEC cylinder, discussed earlier, by a dielectric cylinder, one can derive the Helmholtz equation for the scattered field in Ω_C as [50]:

$$\nabla \cdot \left(\frac{1}{\mu_r} \nabla E_z^s \right) + k^2 \epsilon_r E_z^s = k^2 (1 - \epsilon_r) E_z^{inc}. \quad (2.16)$$

In fact, the right-hand side of this equation represents induced currents due to the incident wave. ϵ_r in transparent dielectric material is equal to square root of the refractive index of that material. The Helmholtz equation governing free space region Ω_{FS} , is obtained from equation (2.16) since $\epsilon_r = 1$ in Ω_{FS} . Scattering by a dielectric microspheres or micro cylinders has been recently utilized in several applications. More detailed discussion on this topic is presented in chapter 6.

2.2 Electromagnetic radiation

In this work, the problem of radiation from a point source is considered because its analytical solution exists. Here, the source is represented as a point in the xy-plane extending along z-axis. Physically, this is a single-line source inside an infinitely-long cylindrical region of arbitrary shape. As pointed in the previous section, the analysis is based on TMz mode. Figure 2.2 shows a line source placed in the region Ω_D , in the xy-plane, and embedded in the free space region Ω_{FS} which is physically unbounded. The line-source is assumed to be placed in an arbitrary position \vec{r}_0 , inside Ω_D . The electric current density of the line-source is given by:

$$\vec{J}_z = I \delta(\vec{r} - \vec{r}_0) \quad (2.17)$$

with I being a constant (Amp/m).

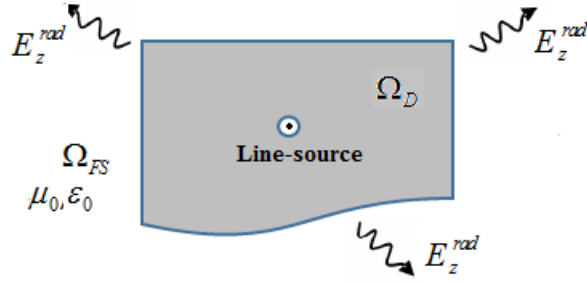


Figure 2. 2 General schematic of the radiation problem.

Maxwell's equations are written as:

$$\nabla \times \vec{E}^{rad} = -j\omega\mu_0\vec{H}^{rad} \quad (2.18)$$

$$\nabla \times \vec{H}^{rad} = j\omega\epsilon_0\vec{E}^{rad} + \vec{J} \quad (2.19)$$

Then the two-dimensional scalar Helmholtz equation governing the radiated electric field can be written as:

$$\nabla^2 E_z^{rad} + k^2 E_z^{rad} = j\omega\mu_0 I \delta(\vec{r} - \vec{r}_0) \quad (2.20)$$

with k being the free-space wave number (of the incident plane wave).

Due to the presence of Dirac delta function, we truncate the free space region around the line-source and simply impose Dirichlet boundary condition on the boundary $\partial\Omega_{FS}$. That is, the problem is redefined as follows:

$$\nabla^2 E_z^{rad} + k^2 E_z^{rad} = 0, \text{ in } \Omega_{FS}, \quad (2.21a)$$

$$\text{with } E_z^{rad} = E_z^{analytical} \text{ on } \partial\Omega_D. \quad (2.21b)$$

The analytical solution $E_z^{analytical}$, which is the solution of equation (2.20), is given by [18]:

$$E_z^{analytical}(\vec{r}) = -\frac{k\eta}{4} IH_0^{(2)}(k|\vec{r} - \vec{r}_0|) \quad (2.22)$$

where, $H_0^{(2)}$ denotes the Hankel function of the second kind of zeroth order, and η is the intrinsic impedance of the medium.

This radiating source is very important in the analysis of electromagnetic problems. That is, when an object is placed in the free space where an incident plane wave exists, the currents are excited everywhere in the object. The object in turn will cause electromagnetic scattering. Numerically speaking, each node in the body of the object acts like a point source radiating the field in the surrounding media. For this reason, the problem defined in equation (2.21) is important. For example, in this thesis, finding the optimum parameters that define a successful domain truncation is based on the radiating point source. In addition, we rely on the same problem to estimate the accuracy achieved by spectral element method when very large objects are encountered.

So far, we have introduced some electromagnetic problems having infinite physical domain. But this situation can't be directly handled by numerical methods. The next section discusses how the physical domain should be modified or truncated so that numerical methods such as finite difference method, finite element method, or spectral element method can be applied.

2.3 Domain truncation

There are quite many problems defined on infinite domains. For instance, electromagnetic radiation and electromagnetic scattering problems most of the time involve infinite domains over which the corresponding set of partial differential equations (PDEs) needs to be solved. In a typical wave-equation problem (See figure 2.3), although the region of interest is finite and the interest is to investigate sources, homogenous and/or inhomogeneous media, nonlinearities, etc, the physical domain is infinite. For this reason, when computation is involved, one needs to truncate the domain so that the problem can be handled without affecting the solution in the region of interest. The important question here is how to perform domain truncation with negligible effect on the region of interest.

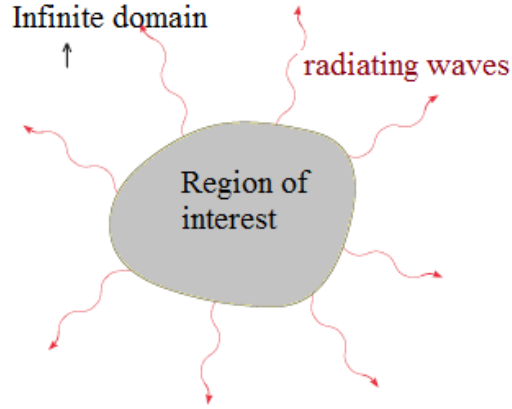


Figure 2. 3 Schematic of a typical wave-equation problem.

The well-known technique by which truncation can be successfully applied is the so called artificial boundary conditions (ABCs) [19]. In this technique the computational domain is effectively coupled to the free space by constructing a boundary operator such that the outgoing waves from the region of interest are absorbed. ABCs are essentially based on a differential operator (boundary operator) such as Trefethen-Halpern General ABC and Higdon Boundary Operator [20]. It was claimed that these two operators perform better than other differential operators.

There are also many other boundary operators, each having some advantages and disadvantages. In general, boundary operators can be classified into two types. The first type has non-local character meaning that the function value at each point on the boundary is related to values at all other points on the boundary. While the second type is local meaning that it is a partial differential operator [3]. Whatever it is, the artificial boundary must be designed in such a way that Sommerfeld radiation condition is satisfied. In two-dimensional scattering problems governed by Helmholtz equation, Sommerfeld radiation condition is defined as:

$$\lim_{|\vec{r}| \rightarrow \infty} \sqrt{|E_z|} \left(\frac{\partial E_z}{\partial r} - jkE_z \right) = 0, \quad (2.23)$$

where \vec{r} is the radiation direction, and E_z stands for either radiated field or scattered field.

Another approach for domain truncation was first introduced by Bettess [21]. In this approach, the finite elements are combined with element of infinite extent. Although, infinite element concept was introduced for problems governed by Laplace's equation in exterior domains, it has also been utilized in electromagnetic scattering problems [22]. However, there are some difficulties arise in the implementation of numerical integration performed over the infinite element when used in wave propagation problems [23].

However, in 1994, Berenger changed the way of thinking: instead of creating an absorbing boundary condition, he introduced an absorbing boundary layer in his well-known paper [4]. In an electromagnetic problem, in which there is a finite region of interest where sources, inhomogeneous media and nonlinearities exist, the domain is truncated by an absorbing boundary layer, as depicted in figure 2.4. That is, the problem is redefined as the original problem bounded by an artificial absorbing boundary layer which is a perfect absorber to all outgoing waves and doesn't reflect them back to the computational region. This absorber is completely independent of the boundary conditions. When a wave enters into this absorber, it is attenuated and decays exponentially; and even if reflections take place within the absorbing layer, the returning waves again are attenuated until they vanish if the absorbing layer is thick enough and the attenuating factor is relatively large.

Berenger showed that a special absorbing medium could be designed so that reflections don't occur at the interface between free-space region and the absorbing layer. This absorber is called; a *perfectly matched layer*, or PML. PML is a very successful approach in which an infinite physical domain is truncated by a perfect absorber that absorbs all waves regardless of their frequency or angle of incidence.

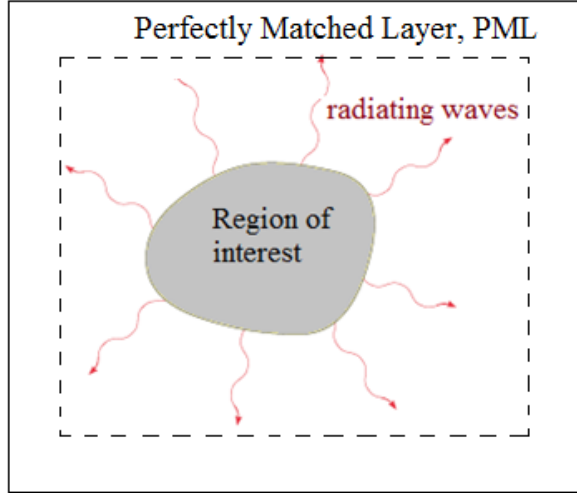


Figure 2. 4 Schematic of a typical wave-equation problem surrounded by PML.

The original formulation of Berenger is called the split-field PML, because the magnetic and electric fields are split into the sum of two new artificial field components. There are two more equivalent PML formulations: anisotropic formulation [5], and bianisotropic formulation [6]. In the next section, derivation of the equations governing the PML in the static case is presented. M. Kuzuoglu and R. Mittra [3] showed that from this derivation it is possible to obtain the three realizations of PML; the split-field PML, anisotropic formulation, and bianisotropic formulation.

2.4 Derivation of the Equations Governing the PML

In the following, y axis (i.e. $x = 0$) is taken as the interface between Ω and Ω_{PML} , which stands for free space and PML regions, respectively, as depicted in figure 2.5. $\Omega = \{(x,y) | x < 0\}$, $\Omega_{PML} = \{(x,y) | x > 0\}$. A plane wave (with suppressed time dependence $\exp(j\omega t)$) incident to the interface can be expressed as:

$$u(x, y) = e^{-jk(\cos\theta x + \sin\theta y)}, \quad (2.24)$$

in which $u(x, y)$ denotes the scalar field at point (x, y) , θ is the incident angle (angle between the direction of propagation of the plane wave and x axis), and k is the wave

number defined by:

$$k = \frac{2\pi}{\lambda}, \quad (2.25)$$

with λ being the wavelength. In the following, $u(x, y)$ will be used to denote the z-component of the field instead of $E_z^{rad}(x, y)$ or $E_z^s(x, y)$ to avoid confusion. As pointed out in [3], in order to provide the attenuation required, one needs to multiply the wave in the PML region by a function $f(x)$ satisfying two properties:

- $f(0) = 1$, so that the field at the interface is not affected, and
- $f(x)$ decreases monotonically for $x > 0$.

For instance, $f(x)$ can be chosen as:

$$f(x) = e^{-\alpha \cos \theta x}. \quad (2.26)$$

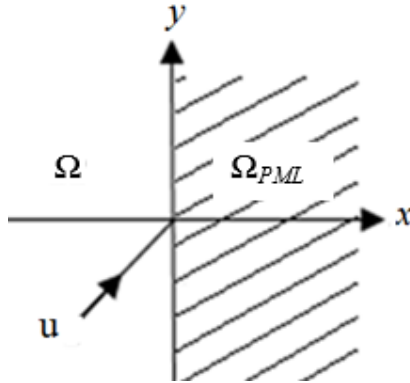


Figure 2. 5 The interface between Ω and Ω_{PML} .

The scalar field in Ω_{PML} then takes the form:

$$u(x, y) = e^{-jk(a \cos \theta x + \sin \theta y)} \quad (2.27)$$

where;

$$a = 1 + \frac{\alpha}{jk}, \quad (2.28)$$

and α is a positive real constant (called attenuation factor). By direct differentiation,

we obtain the following partial differential equation satisfied by the field (2.27):

$$\frac{1}{a^2} \frac{\partial^2 \mathbf{u}}{\partial x^2} + \frac{\partial^2 \mathbf{u}}{\partial y^2} + k^2 \mathbf{u} = 0. \quad (2.29)$$

It is obvious from the derivation above that continuity condition at the interface holds:

$$\mathbf{u}|_{x=0-} = \mathbf{u}|_{x=0+}. \quad (2.30)$$

One more condition is required. At the interface:

$$\left. \frac{\partial \mathbf{u}}{\partial x} \right|_{x=0-} = \frac{1}{a} \left. \frac{\partial \mathbf{u}}{\partial x} \right|_{x=0+}. \quad (2.31)$$

It can be shown by integration by parts that the second condition is automatically satisfied if Helmholtz equation in the PML region is rewritten as:

$$\frac{1}{a} \frac{\partial^2 \mathbf{u}}{\partial x^2} + a \frac{\partial^2 \mathbf{u}}{\partial y^2} + a k^2 \mathbf{u} = 0. \quad (2.32)$$

It can further be shown that for a horizontal interface (i.e., at $y = 0$) the following equation is obtained (while keeping PML thickness the same so that the same attenuation factor α is applied):

$$\frac{\partial^2 \mathbf{u}}{\partial x^2} + \frac{1}{a^2} \frac{\partial^2 \mathbf{u}}{\partial y^2} + k^2 \mathbf{u} = 0. \quad (2.33)$$

And finally for a corner region, which is the intersection of vertical and horizontal PML regions as shown in figure 2.6, the attenuation is applied in both directions [3], and the following partial differential equation is obtained:

$$\frac{1}{a^2} \frac{\partial^2 \mathbf{u}}{\partial x^2} + \frac{1}{a^2} \frac{\partial^2 \mathbf{u}}{\partial y^2} + k^2 \mathbf{u} = 0, \quad (2.34)$$

or:

$$\frac{\partial^2 \mathbf{u}}{\partial x^2} + \frac{\partial^2 \mathbf{u}}{\partial y^2} + a^2 k^2 \mathbf{u} = 0. \quad (2.35)$$

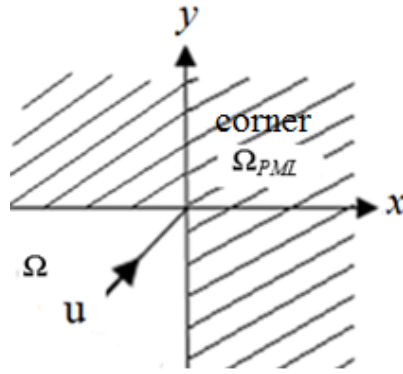


Figure 2. 6 The corner interface between Ω and Ω_{PML} .

Based on this PML formulation, the set of partial differential equations as well as the interface conditions are derived. However, it is not clear how much one should choose the attenuation factor α , and the thickness of the perfectly matched layer. In the next section, choices for the PML parameters are discussed based on the formulation of the PML.

2.5 Choices for the PML parameters

From the physical view of the perfectly matched layer, it can be observed that the only parameter defining the PML is the attenuation factor (α). That is; ideally, the attenuation factor must be chosen infinitely large to make sure that the field magnitude is immediately forced to zero in the PML region. However in numerical applications, the PML must be terminated by an outer boundary and thus arises a second parameter which the thickness of the PML.

From the numerical viewpoint, the thickness should be chosen in such a way that the field is gradually forced to zero, however this requires low attenuation in the PML. Another approach is to choose larger attenuation factor with lower PML thickness, which requires more nodal points (finer mesh/grid) in the PML in order to resolve the fast decay. There are two approaches to overcome this problem. The first one is to design a perfectly matched absorber with different adjacent absorbing layers with

each having different attenuation. For instance, Figure 2.7 shows the magnitude of the field (u) while it is forced to decay in x -direction through multiple absorbing layers until it reaches almost zero. By this way, instead of having sharp decay in the case of single layer, the decay is performed step by step as the wave propagates through PML layers. The second approach is to design the PML with an attenuation factor in such a way that it is a function of position in the longitudinal direction of propagation.

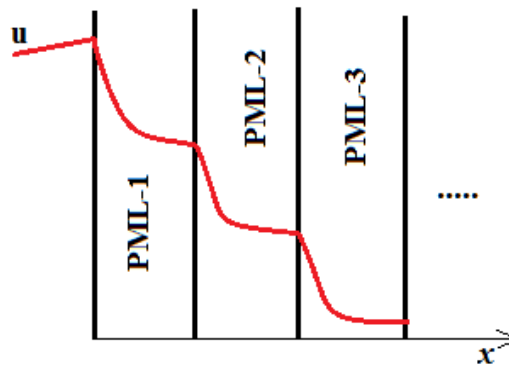


Figure 2. 7 Decaying the field in x -direction using multiple PML layers.

To summarize, one must search for the optimum PML thickness and discretization (i.e. mesh/grid density especially in the longitudinal direction) in the case of single PML layer, in order to represent the field decay as smoothly as possible without causing “numerical” reflections. In other words, there is a trade-off in the choice of the attenuation factor for satisfying the homogenous Dirichlet boundary condition on the outer PML boundary and providing the adequate rate of attenuation within the PML for a specific mesh/grid.

In finite element method, for example, the attenuation of the field in the longitudinal direction in a single-layer PML is about 4 to 6 if the PML thickness is chosen as one wavelength. This choice of attenuation in the literature is gained by experience without being deterministic choice.

It is important to note that in the previous section, the amount of attenuation in the PML is applied equally in both horizontal and vertical layers. This application of attenuation is supported by the following key points:

1. The thickness of the PML in x-decay is chosen the same as that in y-decay. In fact, the thickness is normally chosen to be as much as one wavelength or twice depending on the numerical method used in the computation.
2. The interface between the PML and the free space is placed at a distance far enough from the scatterer so that large fields are avoided to hit the interface. This is based on the fact that either scattered fields or radiated fields decay in general as they propagate out from the region of interest.
3. Since in many problems there is no expectation of magnitudes of the field hitting horizontal interface be different from those hitting the vertical interface, there is no physical reason to choose different attenuations for the same PML thicknesses. Even if there exists such a case (i.e., fields hitting vertical interface are much different in magnitudes from those hitting the horizontal interface), the suitable placement of the interface will overcome this problem as discussed in the second point.

If the thickness of PML is chosen to be one wavelength (i.e., thickness is normalized by the wavelength), then the choice of attenuation will be grid dependent. In another word, the attenuation should guarantee forcing the wave to be negligible at the outer boundary of the PML so that numerical reflections are avoided, and at the same time, there should be enough nodes in the longitudinal direction capable of resolving the attenuated field.

Intuitively, this trade-off implies that at specific number of nodes in the grid, there is a corresponding optimum attenuation factor that gives the best accuracy for that grid. The interest for such an analysis arises from two facts; first, as it will be presented later, the distribution of grid points in Spectral Element Method (SEM) is of Gauss-Legendre-Lobatto type, while in FEM or FDM is not. The regularity in the elements

corresponding to PML region is another important point. That is, the PML can be subdivided into square or rectangular elements when SEM is used.

In this thesis, the PML region is constructed as a single layer of SEM elements with dimensions equal to a wavelength. Under this restriction, the optimal choice of the attenuation factor is carried out via numerical experiments. This is one of the main contributions in this thesis and is discussed further in chapter 5. In addition, as it will be observed from the analysis carried in chapters 5 and 6, single-layer PML is optimal.

The two-dimensional formulation of Helmholtz equation in the context of SEM is presented in the next chapter. This formulation takes into account all the partial differential equations governing the PML region, free space, and magnetic and/or dielectric materials.

CHAPTER 3

SPECTRAL ELEMENT FORMULATION OF ELECTROMAGNETIC SCATTERING/RADIATION PROBLEMS

In this chapter, an introduction to spectral element method is presented which leads to the discrete formulation of electromagnetic scattering and radiation problems. Subsequently, the effect of element shape on the numerical solution obtained by spectral element method is investigated using the point source problem.

3.1 Introduction

Spectral element method was first introduced by Patera [24] in 1984 for computational fluid dynamics. Patera proposed a spectral element method that combines the flexibility of the finite element method with the accuracy of spectral methods (the case where p-type method is applied for a single-element domain). In the spectral element method, he utilized high-order Lagrangian polynomial interpolant over Chebyshev collocation points in order to represent the velocity in each element in the computational domain.

Generally speaking, spectral element methods are considered as a family of approximation schemes based on the Galerkin method. They share common characteristics with finite-element discretizations, and this provides the reason why they can be viewed as h- or p-versions of finite element method. That is, when viewed as h-version, a Lagrangian interpolation formula on the parent element exists in both, as well as the basis functions have local support. On the other hand, spectral element methods use high-degree polynomials on a fixed geometric mesh for sake of

enhanced accuracy, and this is the fact characterizing the p-version of finite element methods [25].

Orthogonality of basis functions either in the h- or p-versions of the finite element is due to non-overlapping local functions. However, in spectral element methods orthogonality is related to both analytical nature and topological nature (local extension) of the basis functions. This fact tells us why spectral element method is different from finite element method of h-version or p-version [26].

There are mainly two implementations that have been proposed, one based on Chebyshev polynomials [24], and the other based on Legendre polynomials. In both cases, Gauss-Lobatto quadrature grid is utilized to perform Lagrangian interpolation. This implementation ensures the continuity of the solution and benefit from the associated numerical quadrature schemes. Patera [24] chose Chebyshev polynomials basically because of the possibility of using fast transform techniques. On the other side, the stiffness and mass matrices were evaluated by the quadratures that were performed analytically without utilizing the weighting factor associated with Chebyshev polynomials [25], (the weighting factor is $(\sqrt{1-x^2})^{-1}$, by which Chebyshev polynomials are orthogonal in contrast to Legendre polynomials whose orthogonality comes with unity weighting factor).

Before we proceed with spectral element formulation, it is important to summarize the set of partial differential equations (PDEs) that governs an electromagnetic scattering or radiation problem. These PDEs are already presented and derived in chapter 2, however, combining them in one equation is important for sake of generality.

3.2 The governing PDEs

In the previous chapter, the derivation of the partial differential equations governing the perfectly matched layer (PML) was presented. However, in a typical

electromagnetic scattering and/or radiation problem, there are a set of partial differential equations to be solved together with the equations governing the PML region. These equations are also derived and presented in chapter 2. Here, we summarize all of these equations in order to provide a complete set to be formulated by spectral element method.

The computational domain is composed of several subdomains that are associated with the following set of partial differential equations:

$$\frac{\partial^2 \mathbf{u}}{\partial x^2} + \frac{\partial^2 \mathbf{u}}{\partial y^2} + k^2 \mathbf{u} = 0, \quad (3.1)$$

is satisfied over the free-space region,

$$\frac{1}{a} \frac{\partial^2 \mathbf{u}}{\partial x^2} + a \frac{\partial^2 \mathbf{u}}{\partial y^2} + a k^2 \mathbf{u} = 0, \quad (3.2)$$

governs the field attenuated in x-direction in PML region,

$$a \frac{\partial^2 \mathbf{u}}{\partial x^2} + \frac{1}{a} \frac{\partial^2 \mathbf{u}}{\partial y^2} + a k^2 \mathbf{u} = 0, \quad (3.3)$$

governs the field attenuated in y-direction in PML region,

$$\frac{1}{a} \frac{\partial^2 \mathbf{u}}{\partial x^2} + \frac{1}{a} \frac{\partial^2 \mathbf{u}}{\partial y^2} + a k^2 \mathbf{u} = 0, \quad (3.4)$$

governs the field attenuated in both x- and y- directions in PML region, and

$$\nabla \cdot \left(\frac{1}{\mu_r} \nabla \mathbf{u} \right) + k^2 \varepsilon_r \mathbf{u} = k^2 (1 - \varepsilon_r) E_z^{inc}, \quad (3.5)$$

is satisfied wherever there is a dielectric object, where; $k = 2\pi / \lambda$ is the wave number, with λ being the wavelength, $a = 1 + \alpha / jk$, α is the attenuation factor, ε_r is the relative permittivity of the scatterer, and μ_r is the relative permeability of the scatterer.

Here, we have changed the notation slightly for convenience. That is; in this set of equations, \mathbf{u} denotes the z-component of the field in the corresponding subdomain: it is the scattered field $E_z^s(x, y)$, or radiated field $E_z^{rad}(x, y)$, if it corresponds to a free-

space subdomain, and it is the absorbed field if it corresponds to the perfectly matched layer.

Figure 3.1 shows a typical electromagnetic scattering domain which is composed of a dielectric scatterer (Ω_{SC}) of an arbitrary shape. The scatterer is embedded in a free-space region represented by Ω_{FS} , and the domain truncation is performed by the perfectly matched layer Ω_{PML} . At this point, a tensor Λ is introduced so that all of the previous equations can be represented in one equation. The tensor is defined as:

$$\Lambda = \begin{bmatrix} \Lambda_{11} & 0 \\ 0 & \Lambda_{22} \end{bmatrix}, \quad (3.6)$$

where;

$$[\Lambda_{11} \quad \Lambda_{22}] = \begin{bmatrix} 1 & \\ a & a \end{bmatrix}$$

for x-decay in the PML region,

$$[\Lambda_{11} \quad \Lambda_{22}] = \begin{bmatrix} a & \\ & 1 \\ & a \end{bmatrix}$$

for y-decay in the PML region,

$$[\Lambda_{11} \quad \Lambda_{22}] = \begin{bmatrix} 1 & \\ & 1 \\ a & a \end{bmatrix}$$

for a corner (xy-decay) in the PML region with $a=1$ in Ω_{FS} , and ε_r being greater than 1 in Ω_{SC} only, and 1 elsewhere.

Thus, the set of all partial differential equations governing an electromagnetic scattering problem can be written as follows:

$$\nabla \cdot \Lambda \nabla \mathbf{u} + a \varepsilon_r k^2 \mathbf{u} = k^2 (1 - \varepsilon_r) E_z^{inc} \quad (3.7)$$

It is worth to mention that for transparent dielectric material and for free-space is $\mu_r = 1$. In addition, $\varepsilon_r > 1$ in the dielectric material only, and $\varepsilon_r = 1$ elsewhere. In

fact, when $\varepsilon_r = 1$, the right-hand side of equation (3.7) vanishes to zero. In the next section, we provide the spectral element formulation for the Helmholtz equation as expressed in equation (3.7) which must be satisfied in a typical electromagnetic scattering and/or radiation problem.

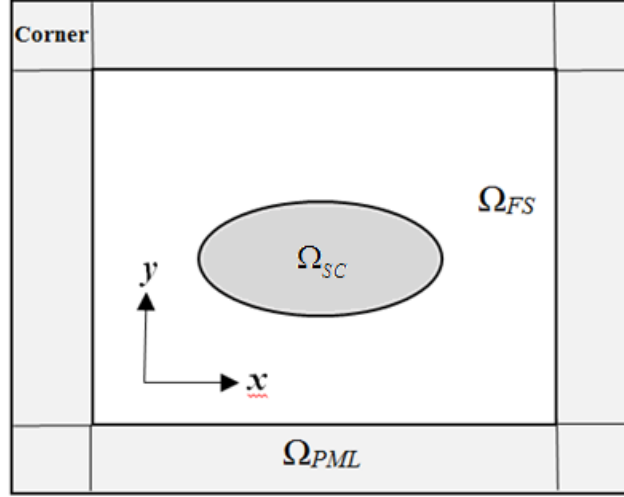


Figure 3. 1 A typical electromagnetic scattering problem composed of a dielectric scatterer (Ω_{SC}) embedded in a free-space Ω_{FS} , and domain truncation is performed by the perfectly matched layer Ω_{PML} .

3.3 SEM formulation

As discussed in the previous section, a typical electromagnetic scattering and/or radiation problem in the frequency-domain can be defined as:

$$\nabla \cdot \nabla \mathbf{u} + \varepsilon_r k^2 \mathbf{u} = k^2 (1 - \varepsilon_r) \mathbf{E}_z^{inc} \quad (3.8a)$$

for $\mathbf{x} = (x, y) \in \Omega \subset \mathfrak{R}^2$ subject to the boundary conditions:

$$\mathbf{u}|_{\partial\Omega_D} = \mathbf{f}, \quad \frac{\partial}{\partial n} \mathbf{u}|_{\partial\Omega_N} = \mathbf{g}, \quad (3.8b)$$

on the boundary $\partial\Omega = \partial\Omega_D \cup \partial\Omega_N$.

SEM formulation involves two function spaces, namely, test and trial spaces. An approximate solution to equation (3.8) is sought in the trial space

$$U = \left\{ \mathbf{u} \in \mathbf{H} \mid \mathbf{u}|_{\partial\Omega_D} = \mathbf{f}, \quad \frac{\partial}{\partial n} \mathbf{u}|_{\partial\Omega_N} = \mathbf{g} \right\}. \quad (3.9)$$

The residual resulting from the substitution of the approximate solution from the trial space into equation (3.8) vanishes in the process of projection onto the test space

$$V = \{ \mathbf{v} \in \mathbf{H} \mid \mathbf{v}|_{\partial\Omega_D} = 0 \}. \quad (3.10)$$

The projection is performed by using the weighted inner product operation:

$$(\mathbf{v}, \mathbf{u})_\omega \equiv \int_{\Omega} \omega \bar{\mathbf{v}} \mathbf{u} \, d\mathbf{x} \quad (3.11)$$

in the Hilbert space \mathbf{H} where overbar denotes complex conjugation. The projection procedure

$$(\mathbf{v}, \nabla \cdot \Lambda \nabla \mathbf{u} + a \varepsilon_r k^2 \mathbf{u} - k^2 (1 - \varepsilon_r) E_z^{inc})_\omega = 0 \quad (3.12)$$

leads to the variational (weak) form

$$\int_{\Omega} \nabla(\omega \bar{\mathbf{v}}) \cdot \Lambda \nabla \mathbf{u} \, d\mathbf{x} - a k^2 \int_{\Omega} \omega \bar{\mathbf{v}} \mathbf{u} \, d\mathbf{x} = \int_{\partial\Omega_N} \omega \bar{\mathbf{v}} \mathbf{g} \, d\mathbf{x} - k^2 (1 - \varepsilon_r) \int_{\Omega} \omega \bar{\mathbf{v}} E_z^{inc} \, d\mathbf{x} \quad (3.13)$$

after integration by parts that introduces the boundary integrals. The trial function is then decomposed as follows

$$\mathbf{u} = \mathbf{u}_h + \mathbf{u}_b, \text{ where } \mathbf{u}_h|_{\partial\Omega_D} = 0 \quad \text{and} \quad \mathbf{u}_b|_{\partial\Omega_D} = \mathbf{f}, \quad (3.14)$$

resulting in

$$\begin{aligned} \int_{\Omega} \nabla(\omega \bar{\mathbf{v}}) \cdot \Lambda \nabla \mathbf{u}_h \, d\mathbf{x} - a k^2 \int_{\Omega} \omega \bar{\mathbf{v}} \mathbf{u}_h \, d\mathbf{x} &= - \int_{\Omega} \nabla(\omega \bar{\mathbf{v}}) \cdot \Lambda \nabla \mathbf{u}_b \, d\mathbf{x} \\ &+ a k^2 \int_{\Omega} \omega \bar{\mathbf{v}} \mathbf{u}_b \, d\mathbf{x} \int_{\partial\Omega_N} \omega \bar{\mathbf{v}} \mathbf{g} \, d\mathbf{x} - k^2 (1 - \varepsilon_r) \int_{\Omega} \omega \bar{\mathbf{v}} E_z^{inc} \, d\mathbf{x} \end{aligned} \quad (3.15)$$

after substitution into equation (3.13). The boundary conditions are now in place in the variational form with the introduction of the particular solution \mathbf{u}_b satisfying the nonhomogeneous Dirichlet boundary condition.

Adapting the formulation to an arbitrary domain geometry is achieved in two steps.

The first step involves partitioning of the domain into mutually disjoint elements:

$$\Omega = \Omega^1 \cup \dots \cup \Omega^e \dots \cup \Omega^M = \bigcup_{e=1}^M \Omega^e. \quad (3.16)$$

A typical integral in the variational form then becomes

$$\int_{\Omega} \omega \bar{v} u_h \, d\mathbf{x} = \sum_{e=1}^M \int_{\Omega^e} \omega \bar{v} u_h \, d\mathbf{x}, \quad (3.17)$$

due to the linearity of integration operation. The second step is the introduction of the standard square element

$$\Omega^{\text{st}} = \{(\xi, \eta) \in \mathbb{R}^2 \mid -1 \leq \xi \leq 1, -1 \leq \eta \leq 1\} \quad (3.18)$$

that will standardize and facilitate the integral operations over a general quadrilateral element Ω^e with curved sides through mapping:

$$\mathbf{x} = \chi_1^e(\xi, \eta), \quad y = \chi_2^e(\xi, \eta). \quad (3.19)$$

In another word, in order to perform the operations of integration and differentiation in an element Ω^e that may have an arbitrary shape and orientation as shown in figure 3.2, the introduction of the one-to-one elemental mapping defined in equation (3.19) is necessary. In fact, this mapping is also onto, which in turn becomes isomorphic transformation. The isomorphism here tells us that inverse transformation exists.

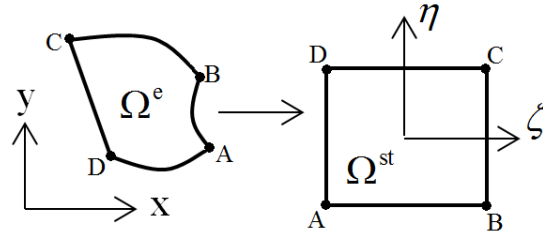


Figure 3. 2 Mapping an element Ω^e to the standard element Ω^{st} .

The differential operations can then be converted using the rules:

$$\begin{bmatrix} dx \\ dy \end{bmatrix} = \underbrace{\begin{bmatrix} \frac{\partial \chi_1^e}{\partial \xi} & \frac{\partial \chi_1^e}{\partial \eta} \\ \frac{\partial \chi_2^e}{\partial \xi} & \frac{\partial \chi_2^e}{\partial \eta} \end{bmatrix}}_{\mathbf{J}} \begin{bmatrix} d\xi \\ d\eta \end{bmatrix}, \quad \nabla = \begin{bmatrix} \frac{\partial}{\partial x} \\ \frac{\partial}{\partial y} \end{bmatrix} = \frac{1}{|\mathbf{J}|} \begin{bmatrix} \frac{\partial \chi_2^e}{\partial \eta} & -\frac{\partial \chi_1^e}{\partial \eta} \\ -\frac{\partial \chi_2^e}{\partial \xi} & \frac{\partial \chi_1^e}{\partial \xi} \end{bmatrix} \begin{bmatrix} \frac{\partial}{\partial \xi} \\ \frac{\partial}{\partial \eta} \end{bmatrix}, \quad (3.20)$$

where $|\mathbf{J}|$ is the determinant of the Jacobian \mathbf{J} .

Numerical implementation of the procedure requires introduction of a spatial discretization that will facilitate the numerical evaluation of the derivatives and the integrals. This is equivalent to taking the trial and test spaces as finite dimensional spaces for which space of polynomials is the convenient choice. Jacobi polynomials as eigenfunctions of singular Sturm-Liouville differential operator provide a good basis for this space [27]. Numerically stable interpolation and highly accurate quadrature integration approximation techniques are provided by nodes and weights associated with Jacobi polynomials. In particular, Legendre polynomials are the convenient choice in that they are orthogonal under the weighted inner product with unity weight $\omega=1$. The associated roots ζ_m as nodes provide the stable form of interpolation

$$\mathbf{u}(\zeta) = \sum_{m=0}^N \mathbf{u}(\zeta_m) L_m(\zeta) \quad (3.21)$$

where L denotes respective Lagrange interpolants with the typical form

$$L_k(\zeta) = \prod_{\substack{\ell=0 \\ \ell \neq k}}^N \frac{(\zeta - \zeta_\ell)}{(\zeta_k - \zeta_\ell)} \quad (3.22)$$

satisfying the cardinality property $L_k(\zeta_\ell) = \delta_{k\ell}$. This in turn provides the means for evaluating the derivatives, say,

$$\left. \frac{d}{d\zeta} \mathbf{u}(\zeta) \right|_{\zeta_k} = \sum_{m=0}^N \mathbf{u}(\zeta_m) L'_m(\zeta_k) = \sum_{m=0}^N \mathbf{u}(\zeta_m) \underbrace{L'_m(\zeta_k)}_{D_{km}} \quad (3.23)$$

where D_{km} is referred to as the differentiation matrix. It also provides Gauss-Legendre-Lobatto (GLL) quadrature

$$\int_{-1}^1 \mathbf{u}(\zeta) d\zeta = \sum_{k=0}^N \bar{\omega}_k \mathbf{u}(\zeta_k) \quad (3.24)$$

which is exact for the integrand of a polynomial of degree $\leq 2N-1$. These can easily be extended to two dimensions over the tensor grid (ξ_k, η_ℓ) with the mapping functions $\chi_i(\xi, \eta)$ constructed using the linear blending function approach [28], [29].

As mentioned above, the nodal basis for the reference element is usually built by Lagrangian basis polynomials associated with a tensor product grid of GLL nodes. Figure 3.3 shows such a grid for a ninth-order polynomial space. In one direction, the GLL grid nodes $\zeta_\ell \in [-1,1]$, $0 \leq \ell \leq N$ are the roots of the polynomial:

$$(1-x^2) \frac{dP_N(x)}{dx} \quad (3.25)$$

where $P_N(x)$ is the Legendre polynomial of degree N in $[-1,1]$:

$$\begin{aligned} P_0(x) &= 1, \\ P_1(x) &= x, \\ P_{n+1}(x) &= \frac{2n+1}{n+1} x P_n(x) - \frac{n}{n+1} P_{n-1}(x), \quad n \geq 1. \end{aligned} \quad (3.26)$$

The first six Legendre polynomials are plotted in figure 3.4.

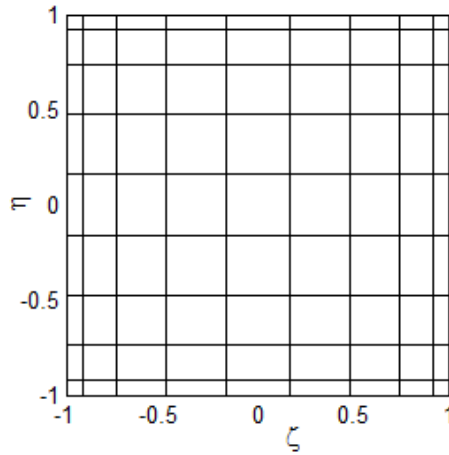


Figure 3. 3 GLL grid nodes on the reference element for a ninth-order polynomial space (nodes are represented by the intersections of horizontal and vertical lines).

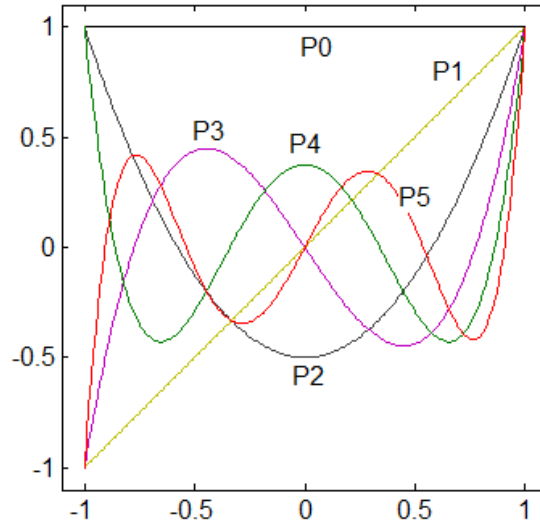


Figure 3. 4 Plot of first six Legendre polynomials.

It is important here to demonstrate the accuracy of the spectral element in one element of square shape and deformed shape. In the following section, the effect of element deformation on the accuracy of spectral element method is investigated.

3.4 SEM accuracy in a single-element domain

3.4.1 Elemental Deformation

Most of practical engineering problems encounter complex geometries, hence; the computational domain requires to be discretized into irregular elements. Meshing a problem in the case of finite element method has been intensively investigated in the literature. For instance, if triangular elements are used to mesh a problem, it is recommended that the smallest angle in the element should not be lower than 15 degrees in order to not deteriorate the accuracy. Similarly, it is important to study the effect of elemental deformation on the accuracy in the case of SEM. In this section, we demonstrate the accuracy of spectral element method for a single-element domain of various quadrilateral deformed elements.

3.4.2 Results

Our investigation is restricted to quadrilateral elements with straight or curved sides. Some examples of these quadrilateral elements are shown in figure 3.5. This flexibility in the shapes of SEM elements can be utilized in meshing complex geometries where different scattering objects of arbitrary shapes are involved.

In this work, the following definition for the elemental aspect ratio (AR) is considered:

$$AR = \frac{\max(d_i)}{\min(d_i)} \quad (3.27)$$

where d_i ($1 \leq i \leq 4$) stands for side length of a quadrilateral element. To make use of this definition, one needs to study the accuracy of SEM for a single-element domain having a reference area with equal dimensions. We call such an element as a reference element. Then, by changing the dimensions and the shape of the element while having the same area as that of the reference element, a comparison can be performed. With this approach, the effect of AR on the accuracy can be investigated. It is also worth to note that all sides of the elements are assumed to have equal nodes.

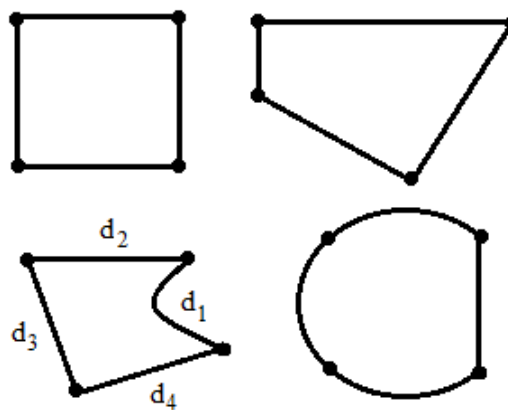


Figure 3. 5 Various quadrilateral elements.

We consider the two-dimensional point source problem that has Helmholtz equation as the governing partial differential equation:

$$\nabla^2 u + k^2 u = -\delta(\vec{r}). \quad (3.28)$$

To avoid the singularity at the origin, the homogenous Helmholtz equation is solved inside a square element (Ω) as shown in figure 3.6 with dimensions $\lambda \times \lambda$, with $\lambda=1$; hence the element has a unit area. This square element will be referred as the reference element. On the boundary $\partial\Omega$, the exact solution to equation 3.28 in terms of Hankel function of the second kind (zero order), $(u(\vec{r}) = (j/4)H_0^{(2)}(k|\vec{r}|))$, is applied as boundary conditions, where $|\vec{r}|$ is the Euclidean distance from the origin to a point \vec{r} on the boundary $\partial\Omega$.

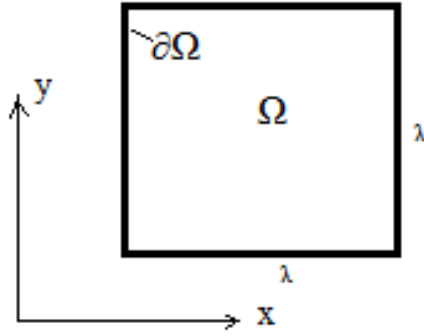


Figure 3. 6 The reference square element with unit area.

The real part of the solution is shown in figure 3.7 for $N=18$ points per wavelength λ . Throughout this work, the maximum relative error is defined as:

$$Err = \max_i \frac{|u_{i,exact} - u_{i,SEM}|}{|u_{i,exact}|} \quad (3.29)$$

where $u_{i,exact}$ and $u_{i,SEM}$ are the exact solution and the SEM solution, respectively, at the i th node corresponding to the free space region, Ω . The error is presented in

Table 3.1 as N increases for the reference square element and for a rectangular element of unit area for aspect ratios: 1.33, 1.88, and 2.87. The effect of the aspect ratio on the accuracy can be clearly observed.

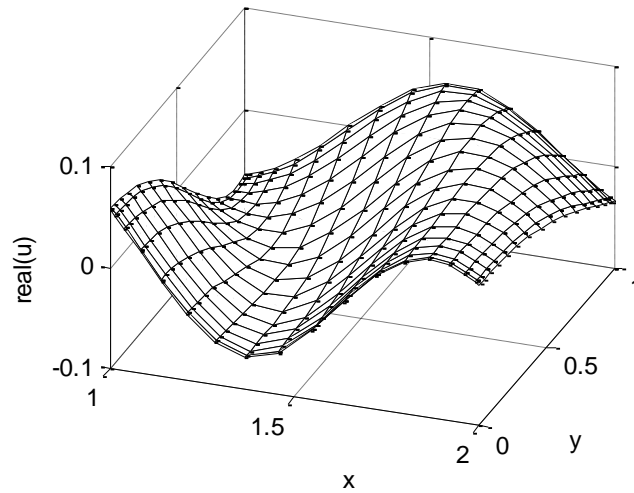


Figure 3. 7 Real part of the solution in the reference element at $N=18$.

Table 3. 1 Relative errors vs N for the reference element and the rectangular element.

N	Square Element	Rectangular Element		
		AR =1.33	AR =1.88	AR =2.87
	<i>Err</i>	<i>Err</i>	<i>Err</i>	<i>Err</i>
7	0.00091	0.0026	0.0903	0.2572
8	1.30E-04	3.4737e-04	0.0163	0.1202
9	1.25E-05	6.4093e-05	0.0027	0.0583
10	1.14E-06	1.0906e-05	5.9235e-04	0.0231
11	1.13E-07	1.7698e-06	1.1915e-04	0.0090
12	1.26E-08	2.9412e-07	2.5201e-05	0.0031
13	1.51E-09	4.4364e-08	5.0504e-06	0.0010
14	2.23E-10	5.9119e-09	9.9654e-07	3.1313e-04
15	2.57E-11	8.9382e-10	1.7686e-07	8.9887e-05
16	3.23E-12	9.1668e-11	3.0693e-08	2.4335e-05
17	2.86E-13	1.2123e-11	4.8938e-09	6.1549e-06

Next, we consider a quadrilateral element with straight sides and having a unit area as shown in figure 3.8. The error is presented in Table 3.2 for the aspect ratios of $AR = 1.33, 1.88$ and 2.87 (while the elemental area is kept the same). It is clearly observed that as the aspect ratio (AR) increases, the accuracy is deteriorated. Figure 3.9, 3.10 and 3.11 show the real part of the numerical solutions at $AR = 1.33, 1.88$ and 2.87 , respectively.

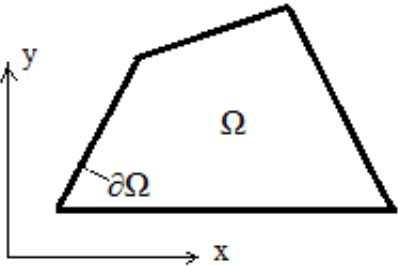


Figure 3. 8 Quadrilateral element with straight sides and unit area.

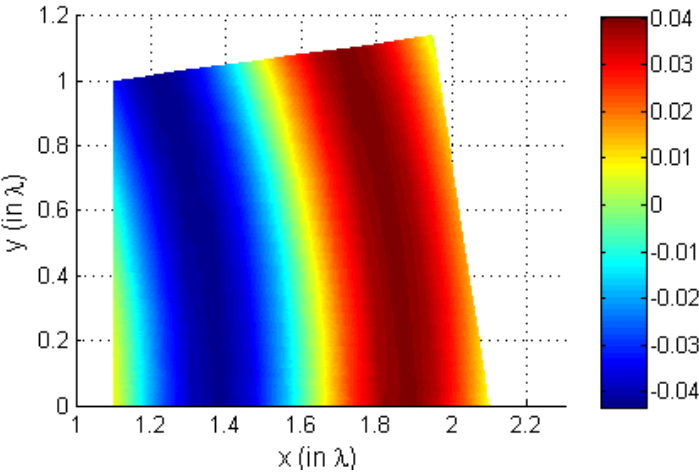


Figure 3. 9 SEM solution for the straight-sided quadrilateral element at $AR = 1.33$.

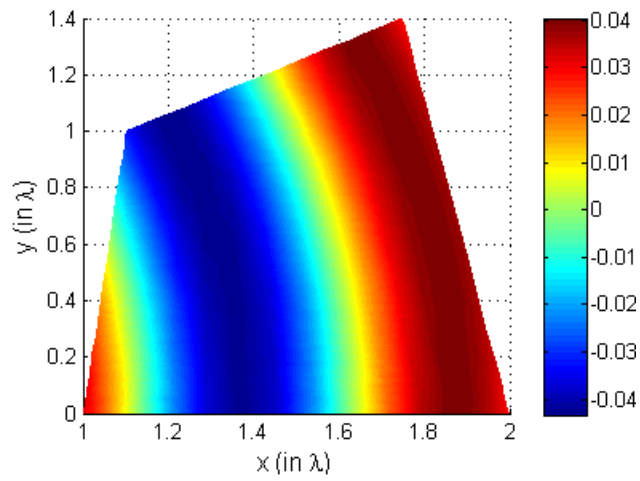


Figure 3. 10 SEM solution for the straight-sided quadrilateral element at $AR = 1.88$.

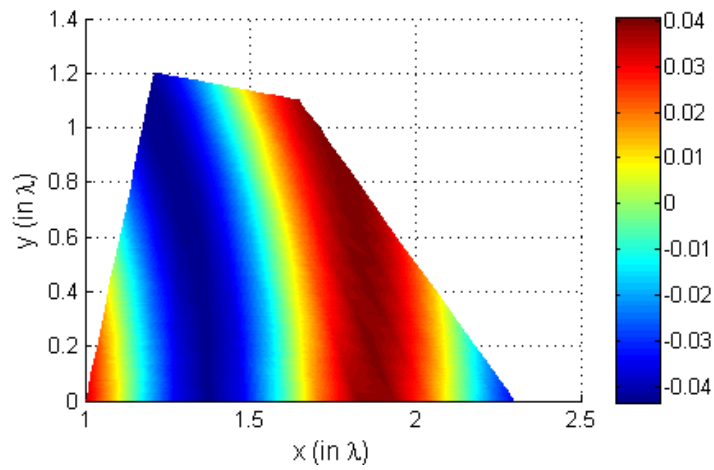


Figure 3. 11 SEM solution for the straight-sided quadrilateral element at $AR = 2.87$.

Table 3. 2 Errors for Quadrilateral element with straight sides and unit area.

N	Err (AR = 1.33)	Err (AR = 1.88)	Err (AR = 2.87)
7	0.001	0.003	0.062
8	1.5e-04	6.0e-04	0.012
9	1.5e-05	1.2e-04	0.004
10	1.6e-06	2.4e-05	0.001
11	1.7e-07	4.6e-06	2.6e-04
12	1.8e-08	8.2e-07	6.3e-05
13	2.0e-09	1.4e-07	1.5e-05
14	2.6e-10	2.3e-08	3.4e-06
15	3.1e-11	3.6e-09	7.3e-07
16	3.8e-12	5.5e-10	1.5e-07
17	4.3e-13	8.0e-11	2.9e-08

Next, a quadrilateral element having one curved side and a unit area is investigated (See figure 3.12). This kind of elements is encountered in meshing of many computational electromagnetic problems. The solution of the point source problem is applied on the boundary of the element where the homogeneous Helmholtz equation is satisfied. The maximum relative errors are presented in Table 3.3 for different values of aspect ratio while keeping the elemental area unchanged.

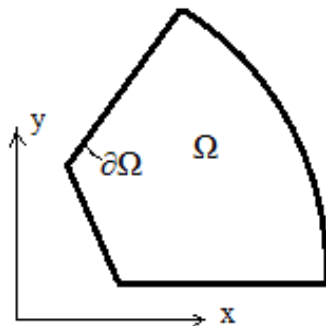


Figure 3. 12 Quadrilateral element having one curved side and a unit area.

Table 3. 3 Errors for Quadrilateral element with curved side and unit area.

N	Err ($AR=1.39$)	Err ($AR=1.91$)	Err ($AR=2.39$)
7	0.0014	0.0016	0.0189
8	0.0005	0.0008	0.0029
9	1.8e-05	3.3e-05	2.7e-04
10	2.1e-05	2.8e-05	3.8e-05
11	2.7e-07	6.5e-07	5.3e-06
12	1.0e-07	1.7e-07	7.2e-07
13	4.4e-08	4.7e-08	9.2e-08
14	5.0e-09	1.3e-08	3.1e-08
15	5.3e-10	1.5e-09	3.2e-09
16	5.3e-11	2.5e-10	8.8e-10
17	5.2e-12	1.6e-10	9.1e-10

Again, we show the real part of the numerical solution for this type of elements in figure 3.13 and 3.14 at $AR=1.39$ and $AR=2.39$, respectively. For convenience, color mapping is utilized so that the dimensions are shown on the corresponding figures.

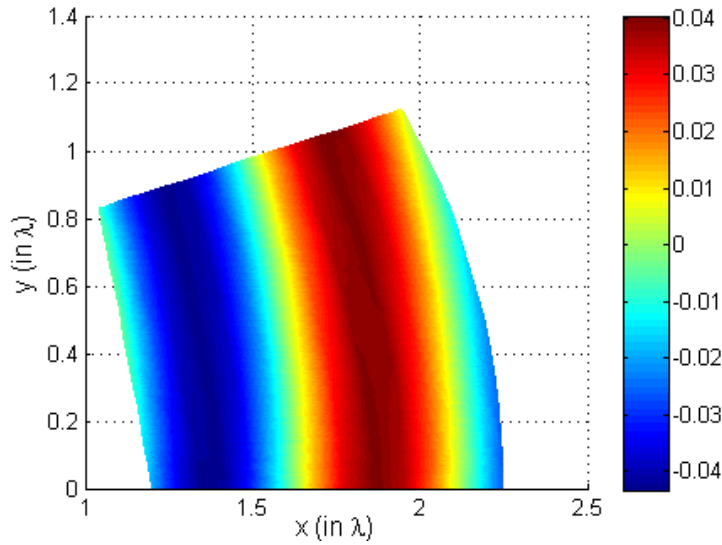


Figure 3. 13 SEM solution for the curved-sided quadrilateral element at $AR = 1.39$.

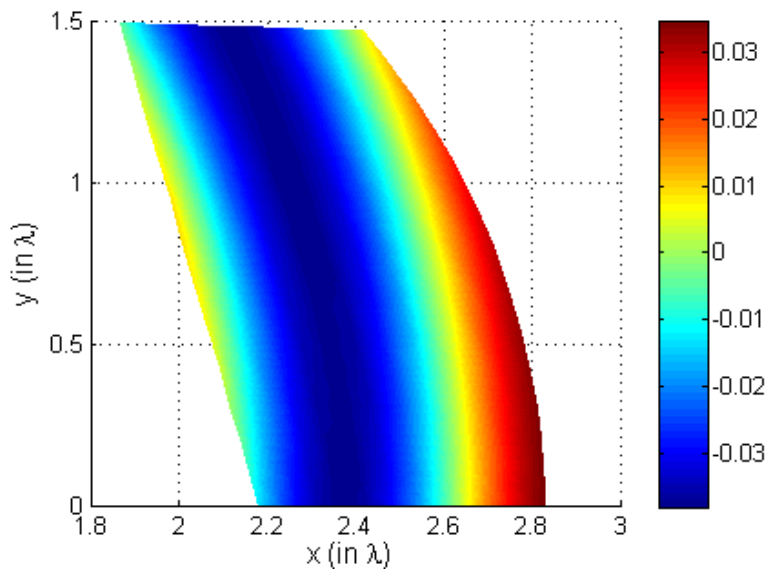


Figure 3. 14 SEM solution for the curved-sided quadrilateral element at $AR = 2.39$.

3.5 Conclusion

In this chapter, the formulation of electromagnetic scattering and radiation problems based on the spectral element method is provided. This formulation considers also domain truncation by the perfectly matched layer. For this purpose, all the partial

differential equations that govern over the perfectly matched layer, free-space regions, magnetic and/or dielectric objects, are put in a single representative form that defines a typical electromagnetic scattering in frequency domain. Numerical implementation by spectral element method is then applied.

Next, the effect of element deformation on the accuracy of spectral element method is investigated. As observed from the results, in quadrilateral elements having straight or curved sides the error was less than that of rectangular elements. Thus, in general, the accuracy can deteriorate if the aspect ratio of some elements is chosen to be large. One can notice from the presented errors that there is no safe range of the aspect ratio in which high accuracy is guaranteed. In conclusion, the discretization of the physical domain should be performed so that the aspect ratio of each element is close to unity as much as possible.

CHAPTER 4

INVESTIGATION OF ITERATIVE METHODS

In this chapter, we investigate some of the well-known iterative methods in solving the resulting system of equations from the perspective of spectral element method. This chapter is arranged in the following manner: we first outline the resulting system of equations to be solved. Then, an introduction to iterative methods is presented. After introducing each iterative method, we present the required number of iterations for the corresponding method to converge. At the end of the chapter, a comparison is made among the investigated iterative methods.

4.1 Resulting Matrix

Based on the formulation presented in chapter 3, the resulting system after discretized by spectral element method in an electromagnetic problem is complex valued. In other words, both the real part and the imaginary part of the unknowns must be solved. The discretization performed by spectral element method results in a system of linear algebraic equations of the form:

$$Hx = b, \quad (4.1)$$

in which H stands for the Helmholtz operator (square matrix) as derived by SEM, x is a vector representing the scattered electric (or magnetic field) to be solved, and b denotes a vector containing the information about the boundary conditions and the right-hand side of the Helmholtz equation.

To apply iterative techniques, one needs to decompose H , x , and b as follows:

$$(H_R + jH_I) \times (x_R + jx_I) = (b_R + jb_I), \quad (4.2)$$

where R and I denote the real component and the imaginary component, respectively. Therefore, the system given in equation (4.2) can be expressed as a block system of equations:

$$\begin{aligned} H_R x_R - H_I x_I &= b_R, \\ H_I x_R + H_R x_I &= b_I, \end{aligned} \quad (4.3)$$

which can be rewritten as a symmetric system of equations [8]:

$$\begin{bmatrix} H_R & H_I \\ H_I & -H_R \end{bmatrix} \begin{bmatrix} x_R \\ -x_I \end{bmatrix} = \begin{bmatrix} b_R \\ b_I \end{bmatrix} \quad (4.4)$$

or equivalently:

$$Ay = f. \quad (4.5)$$

This system is linear, sparse, symmetric, indefinite and relatively ill-conditioned. Hence, solving this system requires an iterative method, and to efficiently solve it, a suitable preconditioner must be applied. Before we proceed, we will present an overview of the storage scheme in order to utilize the sparsity in the system.

4.2 Storage Schemes

The resulting system matrix formed by spectral element method is sparse. Therefore, in order to utilize this property for purpose of storage savings, special storing schemes are required to be used. The aim of these schemes is to store only the nonzero elements of the system matrix, and at the same time, to be able to perform matrix operations required by the iterative method.

Before we proceed, it is worthy to pay attention to two points. First, although it is apparent that the final system presented in equation (4.5) has twice the dimensions of the original system defined by equation (4.1) because the original system is decomposed into real and imaginary parts, this increase in the dimensions doesn't cost extra storage requirement. In another word, the original system is already in complex form which requires the memory to allocate the same number of bytes for real numbers and for imaginary numbers. In addition, from the view of CPU, the

time required to solve the system in (4.1) is the same as that required to solve the decomposed system since the same number of algebraic operations (addition and multiplication operations) will be carried in both systems.

The second point is that, based on the formulation of electromagnetic scattering problems by spectral element method, it is important to illustrate an example which gives an outlook to the percentage of the nonzero elements in the system matrix. For this purpose, a problem with ten elements is chosen, and in each element has 11×11 GLL nodes. The resulting total number of the unknowns in equation (4.1) is 959. Among 919681 elements, there are 804162 zero elements. From this example, we can see that only a percentage of 12.56% from all matrix entries needs to be stored.

When storing such sparse matrices, the simplest scheme is the coordinate format. In this scheme, the data structure consists of three arrays:

- An array containing all the nonzero elements of the system matrix in any order,
- An integer array containing the row indices of the nonzero elements, and
- An integer array containing the column indices of the nonzero elements.

4.3 An overview of Iterative Methods

Iterative methods are mainly classified as stationary and nonstationary. Stationary methods are older and easier to implement, however, they are not that much effective. Stationary methods include [35]:

- a. Jacobi method: In this method, the solution is performed locally for each variable in terms of other variables. Although it is easy to implement, Jacobi has slow convergence.
- b. Gauss-Seidel method: It is similar to Jacobi method except that it updates values immediately after they are available. Compared with Jacobi method, Gauss-Seidel method has faster convergence but still relatively slow.

- c. Successive Over Relaxation (SOR): This method is an extension of Gauss-Seidel method after introducing an extrapolation parameter ω . If ω is chosen optimally, SOR can converge faster than Gauss-Seidel.
- d. Symmetric SOR (SSOR) is useful if considered as a preconditioner.

Stationary methods can be expressed as in the following form:

$$x^{(k)} = Ax^{(k-1)} + c, \quad (4.6)$$

and they are called stationary iterative methods since none of A or c are dependent upon the iteration counter, k .

Nonstationary methods, on the other hand, can be highly effective. They mainly include:

1. Conjugate Gradient (CG).
2. Minimum Residual (MINRES).
3. Conjugate Gradient on the Normal Equations (CGNE).
4. Generalized Minimal Residual (GMRES).
5. BiConjugate Gradient (BiCG).
6. Quasi-Minimal Residual (QMR).
7. Conjugate Gradient Squared (CGS).
8. BiConjugate Gradient Stabilized.
9. Chebyshev Iteration.

4.4 Conjugate Gradient Method

The conjugate gradient method is one of the oldest among nonstationary methods. It is known of its efficiency for symmetric positive definite systems [35], [36]. It proceeds by generating successive approximations to the solution, residuals corresponds to the iteration, and search directions which is used in updating the residuals and iterates. In each iteration, in order to compute update the scalars so that certain orthogonality conditions are satisfied, two inner products must be performed.

If the system is symmetric positive definite, the orthogonality conditions ensure that the distance to the correct solution is minimized [35].

However, since the resulting system in our work is not positive definite, equation (4.5) must be modified by multiplying it with the transpose of the matrix A , i.e.,

$$A^T A y = A^T f \quad (4.7)$$

or,

$$B y = g \quad (4.8)$$

It is important to pay attention to the conditional number of the new system. This operation of multiplication results in having higher conditional number (in fact, it is square of the conditional number of A). However, this point is not much important as long as preconditioners will take care of this increase in ill-conditioning.

The algorithm of the conjugate gradient method is given below:

Compute $r^{(0)} = g - B y^{(0)}$, where $y^{(0)}$ is the initial guess

for $k = 1, 2, \dots$

solve $M z^{(k-1)} = r^{(k-1)}$

$\rho^{(k-1)} = r^{(k-1)T} z^{(k-1)}$

if $k = 1$

$p^{(1)} = z^{(0)}$

else

$\beta^{(k-1)} = \rho^{(k-1)} / \rho^{(k-2)}$

$p^{(k)} = z^{(k-1)} + \beta^{(k-1)} p^{(k-1)}$, *end if*

$q^{(k)} = B p^{(k-1)}$

$\alpha^{(k)} = \rho^{(k-1)} / p^{(k)T} q^{(k)}$

$y^{(k)} = y^{(k-1)} + \alpha^{(k)} p^{(k)}$

$r^{(k)} = r^{(k-1)} - \alpha^{(k)} q^{(k)}$

check convergence, if no, iterate

end,

where $r^{(k)}$ is the residual, $p^{(k)}$ is the search direction corresponding the k^{th} iteration, and M is the identity matrix for the unpreconditioned conjugate gradient, and it is the

preconditioner for the preconditioned conjugate gradient method. The choice $\beta^{(k-1)} = \rho^{(k-1)} / \rho^{(k-2)}$ is made to ensure that $p^{(k)}$ and $r^{(k)}$ are orthogonal to all previous $Bp^{(k)}$ and $r^{(k)}$, respectively. As can be observed from the algorithm, the conjugate gradient method involves three vector updates, only one matrix vector multiplication, and two inner products in each iteration.

Next, we will solve the resulting linear system of equations by conjugate gradient method without any preconditioner. Here, it is worth to point that although the method may converge for indefinite systems, convergence is not guaranteed all the time.

We considered a matrix size of 3274×3274 , i.e., the number of unknowns is 3274. Conjugate gradient method is used to solve such a linear system of equations. The relation between the residual and the number of iterations required for the algorithm to converge is shown in figure 4.1.

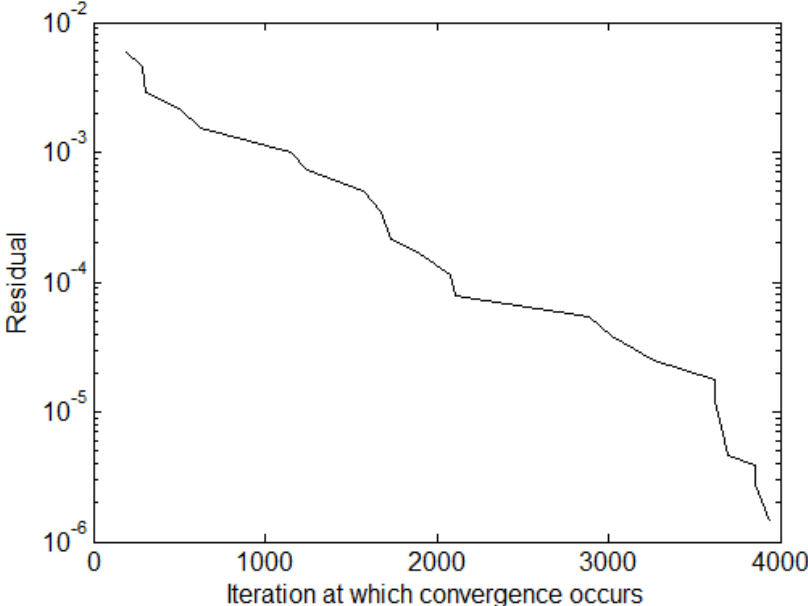


Figure 4. 1 Conjugate Gradient method: Residual versus number of iterations.

4.5 Biconjugate Gradient Method

The Biconjugate Gradient method was first proposed in 1952 by Lanczos [37]. After that, in 1974 Fletcher [38] provided a different version of it known as Conjugate Gradient-like version. The algorithm of the Biconjugate Gradient method is given as follows:

Compute $r^{(0)} = g - By^{(0)}$, choose $r^{(0)*}$ such that $r^{(0)*} \cdot r^{(0)} \neq 0$

Set $p^{(0)} = r^{(0)}$, $p^{(0)*} = r^{(0)*}$

for $j = 0, 1, 2, \dots$

$$\alpha^{(j)} = (r^{(j)}, r^{(j)*}) / (Bp^{(j)}, p^{(j)*})$$

$$y^{(j+1)} = y^{(j)} + \alpha^{(j)} p^{(j)}$$

$$r^{(j+1)} = r^{(j)} - \alpha^{(j)} Bp^{(j)}$$

$$r^{(j+1)*} = r^{(j)*} - \alpha^{(j)} B^T p^{(j)*}$$

$$\beta^{(j)} = (r^{(j+1)}, r^{(j+1)*}) / (r^{(j)}, r^{(j)*})$$

$$p^{(j+1)} = r^{(j+1)} + \beta^{(j)} p^{(j)}$$

$$p^{(j+1)*} = r^{(j+1)*} + \beta^{(j)} p^{(j)*}$$

end if satisfied

The Biconjugate Gradient is implemented for the same system mentioned previously. Jacobi preconditioner which will be introduced later in this chapter is applied. The relation between the residual and the number of iterations required for the algorithm to converge is shown in figure 4.2.

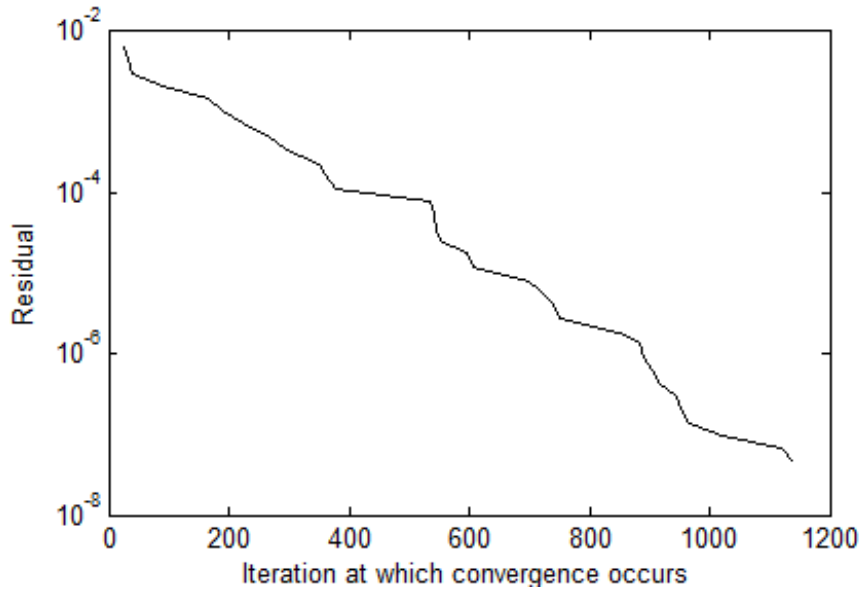


Figure 4. 2 Biconjugate Gradient method: Residual versus number of iterations.

4.6 Preconditioned Conjugate Gradient Method

The rate of convergence of an iterative method mainly depends on the properties of the coefficient matrix. Since the resulting system to be solved in this work is relatively ill-conditioned, one wonders whether it is possible to transform the system into another system which is equivalent in the sense that the same solution can be obtained, and this new system has more favorable properties. Fortunately this is possible by introducing a matrix that performs such a transformation. This matrix is called a preconditioner and it is denoted by M in this thesis.

The preconditioner M , should approximate the original matrix B , and results into an easier system to solve. Or equivalently, preconditioning means finding M that approximates inverse of B while only multiplication by M is required, i.e. it provides some numerical savings. In another word, the preconditioned system has the form:

$$M^{-1}By = M^{-1}g \quad (4.9)$$

Apparently, there is a trade-off between the operational cost involving the preconditioner and the gain obtained from increasing the speed of convergence. There are some preconditioners, such as SSOR preconditioner, that requires very little construction phase; on the other hand, incomplete factorizations, for instance, demands substantial work. In general, most of preconditioners require work that is proportional to the number of unknowns [35].

Since the conjugate gradient method is a very powerful iterative method, in this work, we use this method wherever a preconditioner is discussed. Some of the well-known preconditioners are discussed and implemented in the following subsections.

4.6.1 Jacobi Preconditioning

Jacobi preconditioner is the simplest one and its elements are defined by:

$$m_{ij} = \begin{cases} b_{ij}, & \text{if } i = j \\ 0, & \text{otherwise} \end{cases}, \quad (4.10)$$

where b_{ij} are the elements of the matrix B defined in equation (4.8). In other words, Jacobi preconditioner contains just the diagonal elements of B . The numerical benefits utilized by implementing Jacobi preconditioner are the storage savings (i.e., no need to store the elements of Jacobi since its elements are the diagonal of B), and the ease in inverting it. However, since division operations are costly, storing Jacobi preconditioner is carried by storing the reciprocals of the matrix diagonal.

The Conjugate Gradient is utilized with Jacobi preconditioning for the same system defined previously. The relation between the residual and the number of iterations required for the algorithm to converge is shown in figure 4.3.

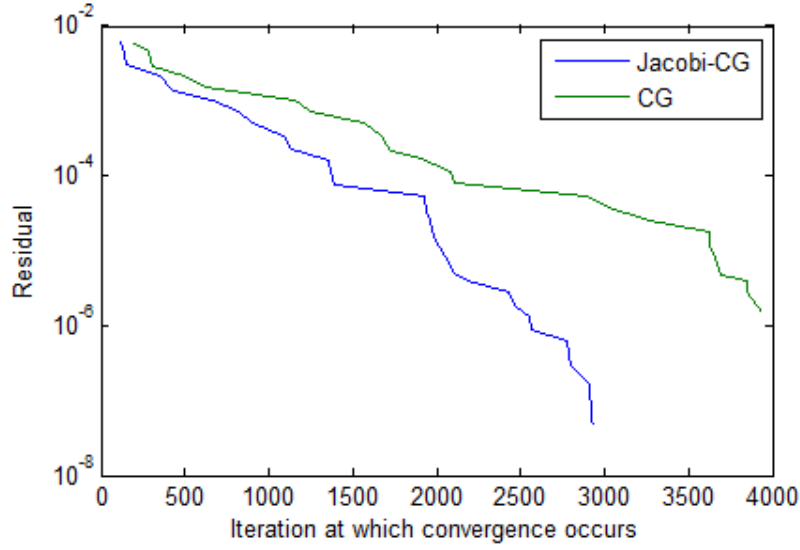


Figure 4. 3 Preconditioned Conjugate Gradient method: Residual versus number of iterations.

4.6.2 SSOR Preconditioning

Jacobi and symmetric successive over relaxation (SSOR) preconditioners are easy to derive from the system matrix B . SSOR derivation proceeds by decomposing B as follows:

$$B = D + L + L^T \quad (4.11)$$

where D is the diagonal of B , and L , L^T are the lower and upper triangular matrices. Here it is worth to point that since B is symmetric, the upper triangular matrix is simply the transpose of the lower triangular matrix. With the aid of this decomposition, the SSOR preconditioning matrix is defined as:

$$M = (D + L)D^{-1}(D + L)^T \quad (4.12)$$

which can be parameterized by factor ω as:

$$M = \frac{1}{2 - \omega} \left(\frac{1}{\omega} D + L \right) \left(\frac{1}{\omega} D \right)^{-1} \left(\frac{1}{\omega} D + L \right)^T. \quad (4.13)$$

A theorem presented by Kahan [39], shows that SOR fails to converge as an iterative method if ω lies outside the open interval $(0, 2)$. And if $\omega = 1$, SOR reduces to

Gauss-Seidel method. When SSOR preconditioning is utilized, there will be an optimum value for ω at which the convergence rate is increased. Although the convergence is not guaranteed when ω is outside the mentioned interval, we have searched for the optimal value inside and outside the interval $(0, 2)$.

We applied the SSOR preconditioner to solve our system. The relation between the residual and the number of iterations required for the algorithm to converge is shown in figure 4.4 for $\omega = 1$, $\omega = 7$ and $\omega = 10$. In fact, different values were also investigated, however, the minimum number of iterations that can be achieved occurs between $\omega = 7$ and $\omega = 10$.

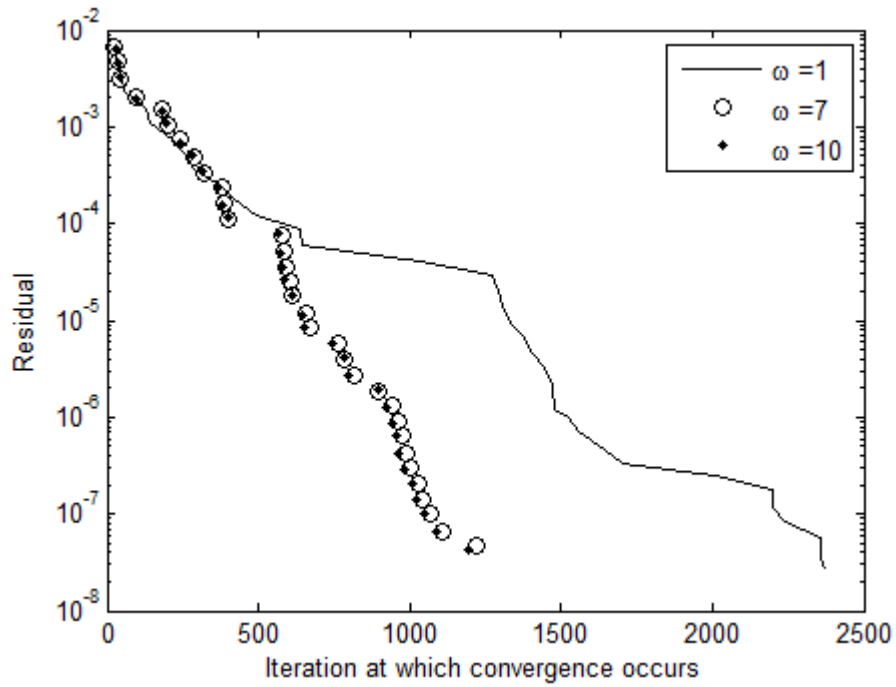


Figure 4. 4 SSOR preconditioner: Residual versus number of iterations.

4.6.3 ILU Factorization Preconditioners

Incomplete LU (ILU) factorization of the system matrix B computes a sparse upper triangular matrix U and a sparse lower triangular matrix L so that the multiplication of L and U approximates B , or equivalently the residual matrix $R = LU - B$ satisfies some constraints such as having zero elements in some locations. In this work we use the Zero Fill-in factorization (ILU(0)).

When ILU factorization technique is used with no fill-in, it has the same zero pattern as that of the system matrix B . That is, ILU(0) is to find any pair of matrices L and U such that the elements of $R = LU - B$ are zero in locations of $NZ(B)$, where $NZ(B)$ is the set of pairs (i, j) , $1 \leq (i, j) \leq n$ such that $b_{ij} \neq 0$, and n is the number of unknowns. However, these constraints don't define ILU(0) uniquely as infinitely many pairs of L and U can satisfy the above requirements [36]. So, the standard ILU(0) can be built as shown in the following algorithm:

```

Algorithm of ILU(0) :
for i = 2, ..., n
  for k = 1, ..., i - 1 and for (i, k) ∈ NZ(B)
    compute  $b_{ik} = b_{ik} / b_{kk}$ 
  for j = k + 1, ..., n and for (i, j) ∈ NZ(B)
    compute  $b_{ij} = b_{ij} - b_{ik} b_{kj}$ 
  end
end
end

```

The zero fill-in ILU preconditioning matrix can then be written as:

$$M = (D - E)D^{-1}(D - F) \quad (4.14)$$

where $-E$ and $-F$ are the strict lower triangular and strict upper triangular matrices of B , respectively, and D is a certain diagonal matrix which is different from the diagonal of B . If the preconditioning in equation (4.14) is considered, then the elements of the matrix D are determined by a recursive formula.

It is obvious that an extra storage is required for the diagonal without large storage costs. This kind of preconditioning is very similar to SSOR case when $\omega=1$, however, they are different in the way in which the diagonal matrices are constructed. That is, in SSOR, the diagonal matrix is the diagonal of the system matrix B , however, in ILU(0), the diagonal is determined in such a way that the diagonal of the preconditioner M equals to the diagonal of B . It is important to note that the number of nonzero elements in both L and U is identical to the number of nonzero elements in the system matrix B .

The relation between the residual and the number of iterations required for the algorithm to converge is shown in figure 4.5. The linearity in the figure (although they are shown in logarithmic scales, but when compared with other preconditioners) can be observed clearly, which means that ILU(0) has less convergence rate.

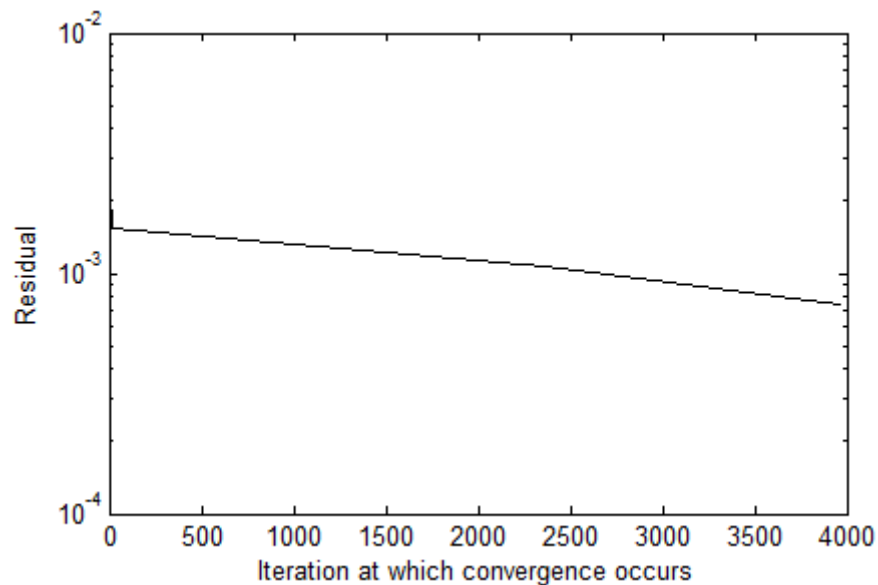


Figure 4. 5 ILU(0) preconditioner: Residual versus number of iterations.

4.7 Generalized Minimum Residual Method

The Generalized Minimum Residual method (GMRES) is an extension of the MINRES. It can be utilized for linear symmetric or unsymmetric systems, and proposed by Saad and Schultz [40]. It is an iterative method proposed for solving linear systems and minimizes the norm of the residual vector over a Krylov subspace in every step, i.e., without the iteration having been formed. Therefore, the iteration is postponed until the residual norm becomes small enough [35]. One of its most popular forms utilizes Gram-Schmidt procedure and uses restarts to control storage requirements. That is why it is sometimes called Restarted GMRES.

One of drawbacks of GMRES is that storage requirement increases as the iteration counts increase. Fortunately, the solution to this problem is achieved by restarting the iteration. That is, the accumulated data are cleared from the memory after a chosen number of iterations (m) and the obtained results are immediately utilized to initialize the next number of iterations. The procedure is repeated until convergence is achieved.

When GMRES is used to solve our system, the relation between the residual and the number of iterations required for the algorithm to converge is shown in figure 4.6 for two different Restarts: 10 and 30.

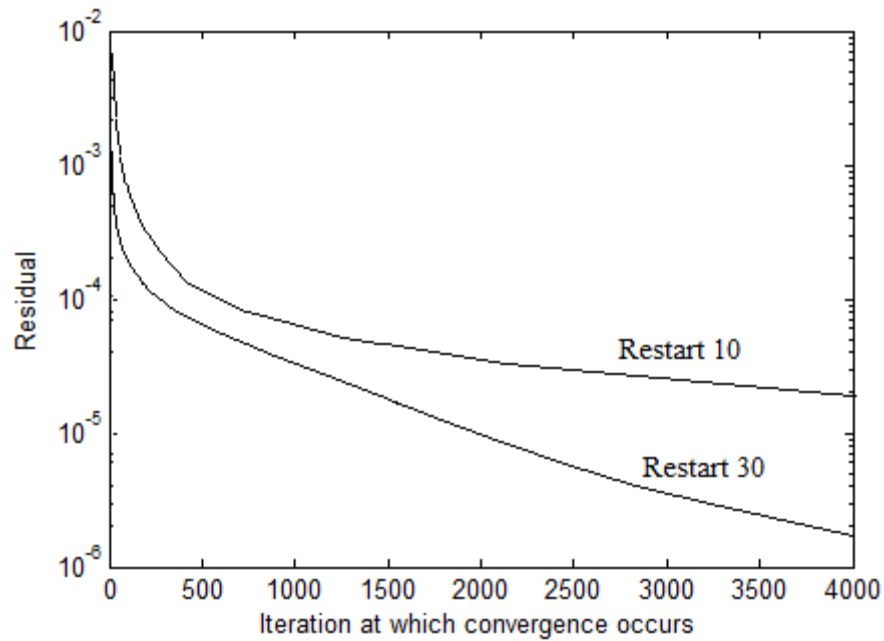


Figure 4. 6 GMRES: Residual versus number of iterations.

4.7.1 Preconditioned Generalized Minimum Residual Method

When used as a preconditioned iterative method, Restarted GMRES accepts the application of preconditioning operation as in the case of conjugate gradient method. However, there is a fundamental difference in the case of the right preconditioning which gives a rise to what is called the flexible variant (the variant in which the preconditioner may change in each step). In this work, we considered left preconditioners. Mainly, we apply Jacobi preconditioner in order to perform a comparison between the Restarted GMRES method and the Conjugate Gradient method. The relation between the residual and the number of iterations required for the algorithm to converge is shown in figure 4.7 when the Restart is 10.

The algorithm that performs the left preconditioned GMRES is presented below for Jacobi preconditioner M :

Algorithm of left preconditioned GMRES :

compute $r_0 = M^{-1}(g - By_0)$, $\beta = \|r_0\|_2$ and $v_1 = r_0 / \beta$

for $j = 1, \dots, n$

 compute $\omega = M^{-1}Bv_j$

 for $i = 1, \dots, j$

$h_{ij} = (\omega, v_i)$

$\omega = \omega - h_{ij}v_i$

 end

 compute $h_{j+1,j} = \|\omega\|_2$ and $v_{j+1} = \omega / h_{j+1,j}$

end

$V_m = [v_1, \dots, v_m]$

$H_m = \{h_{ij}, 1 \leq i \leq j+1\}$

$z_m = \arg \min_z \|\beta e_1 - H_m z\|_2$

$y_m = y_0 + V_m z_m$

if satisfied Stop, else set $y_0 = y_m$

Repeat.

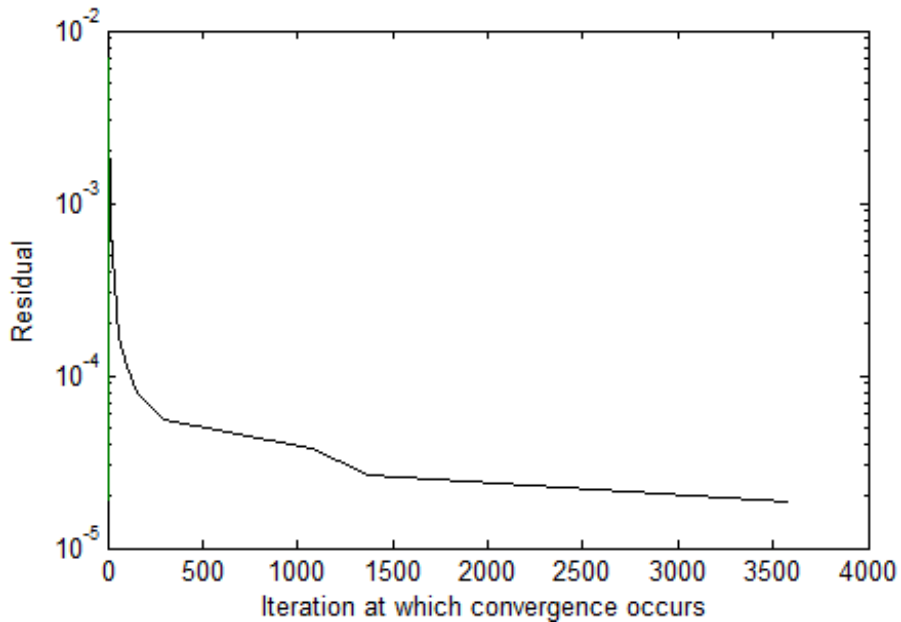


Figure 4. 7 Preconditioned GMRES: Residual versus number of iterations.

4.8 Conclusion

When comparing the number of iterations for both conjugate gradient method and GMRES method with a restart of 30 without any preconditioning, one can see that the GMRES has less number of iterations at a specific tolerance. Such a comparison is shown on figure 4.8. However, in terms of time spent the computer, the conjugate gradient method was much faster.

Figure 4.9 compares the conjugate gradient with and without Jacobi preconditioning and the preconditioned Biconjugate gradient method. First of all, it is clear that when preconditioning is utilized in iterative methods, the number of iteration is much reduced. However, the cost is paid in terms of number of operations. It can also be observed that the preconditioned Biconjugate gradient requires the least number of iterations but the solution time is much higher. For this reason, we used the conjugate gradient method to carry a comparison among the preconditioners presented.

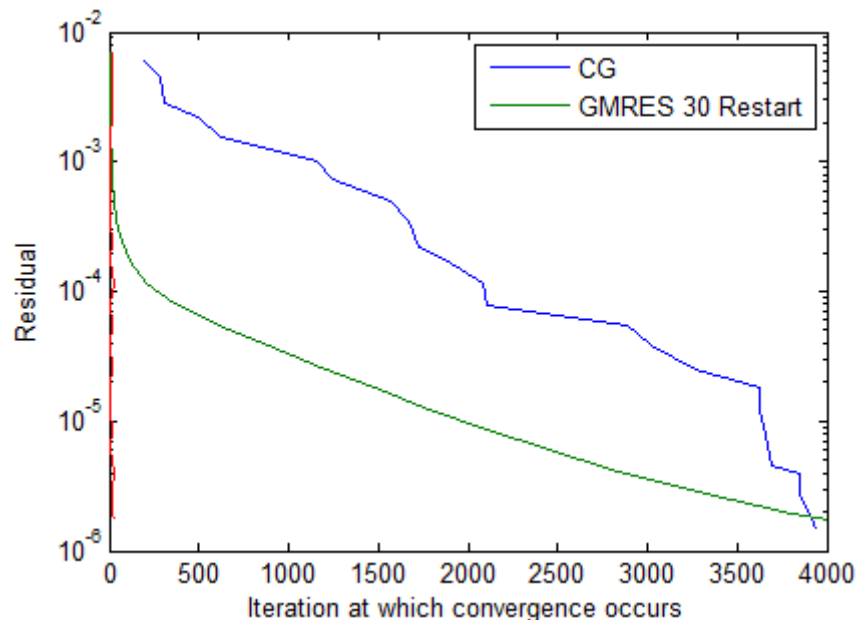


Figure 4. 8 GMRES method and the Conjugate Gradient method.

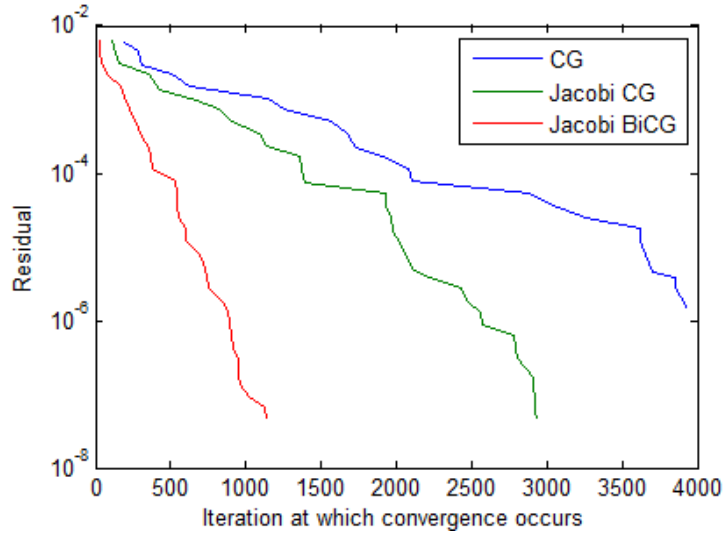


Figure 4. 9 Preconditioned Conjugate Gradient and Biconjugate Gradient methods.

In figure 4.10, we show a comparison between the conjugate gradient method preconditioned with: Jacobi, incomplete LU decomposition, and the SSOR preconditioners and the GMRES method with Jacobi preconditioner. Obviously, SSOR with $\omega=7$ requires the minimum number of iterations amongst other preconditioners, the cost is paid in terms of solution time.

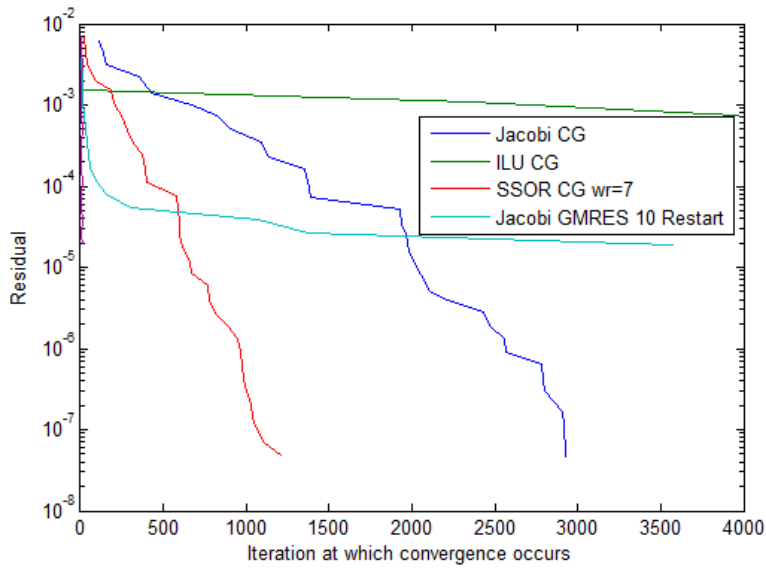


Figure 4. 10 Preconditioned Conjugate Gradient and GMRES methods.

It can be clearly seen from the previous results that the preconditioned Biconjugate Gradient method converges at less number of iterations than the preconditioned Conjugate Gradient method; however, the time spent by the computing machine was less in the case of preconditioned Conjugate gradient than that of preconditioned Biconjugate Gradient. In fact, Conjugate gradient with Jacobi preconditioner took the minimum time among all other preconditioners. In addition, without any preconditioner, the Conjugate Gradient method was the fastest iterative method in terms of time. However, the number of iterations required by an iterative method is also important. The GRMES, on the other hand, depends on its restart. For instance, results with a restart of 30 were better than that of 10, at the same time, when the restart increases, additional memory is required. The SSOR preconditioning is also utilized in our work. It can be observed that when relaxation factor is in between 7 and 10, better results can be achieved.

Several iterative methods are utilized in this thesis with different preconditioners. In summary, there is a trade-off between the operational cost for the preconditioner, in terms of storage requirement, and the gain obtained from increasing the speed of convergence.

However, we should note that the problems discussed in this work are solved by direct methods; namely by the backslash operator (`mldivide`) in MATLAB. When iterative solvers are considered, most of them are saturated at a relatively small stopping criterion (tolerance) in terms of the accuracy obtained by spectral element method. For instance, we checked the maximum relative error between the iteratively-solved solution and the analytical solution for the same linear system of equations discussed in this chapter by using conjugate gradient method with Jacobi preconditioner. The expected maximum relative error between SEM solution when direct solvers are utilized and the analytical solution is $1e-09$. As observed from Table 4.1, when iterative solvers are used, we need at least a tolerance of $1e-09$ in order to get the same SEM accuracy. In fact such a tolerance is relatively small for

iterative methods. However, this means that when we seek an accuracy of $1e-012$, for example, the corresponding tolerance in this case will be extremely small.

The need for iterative solvers arises in the cases where very large problems with complex geometries are involved. This is because of the fact that as the system of equations gets larger and larger with being sparse, the condition number will get large as well. This ill-conditioning is investigated for spectral element method, finite difference method and finite element method in the next chapter.

Table 4. 1 Errors obtained by Jacobi preconditioner.

Tolerance	<i>Err</i>
1e-02	1.01
1e-05	0.0029
1e-07	8.3617e-06
1e-08	6.5719e-08
1e-09	4.0115e-09, time=59.4sec

CHAPTER 5

APPLICATION OF SPECTRAL ELEMENT METHOD IN ELECTROMAGNETIC RADIATION PROBLEMS

5.1 Introduction

In the second chapter of this thesis, the formulation of the perfectly matched layer (PML) is presented. The corresponding set of partial differential equations of the PML (as an approach for domain truncation) and the regions where the electromagnetic field is to be solved by spectral element method are defined. However, important questions arise here; for instance, how the electromagnetic field should be attenuated within the PML region so that domain truncation is successfully performed without affecting the solution of interest. By other words; what is the attenuating factor (α) that well defines the PML in order to make it perfect absorbing layer when spectral element method is utilized as a numerical method in electromagnetic scattering and/or radiation problems?

Another important issue here is that, how the factor α should be chosen for different grids associated with the elements representing the PML region. And one wonders whether there is an optimum value for this factor at a specific grid and specific PML thickness or not. In addition, what is the burden caused by the PML thickness if it is chosen much larger than a wavelength?

In this chapter, we optimize the value of the attenuating factor in the PML region based on an electromagnetic radiation problem. Justification of these choices is discussed. Then we check the optimized values by inspecting the solutions of

scattered fields from perfectly conducting cylinders of both circular type and square type. The estimation of relative errors of electrically large objects is then provided.

However, to get an insight about the accuracy gained from spectral element method, when compared to other numerical methods, demonstrations are performed using numerical examples. For this purpose, we first start by comparing the accuracy of finite element method and finite difference method with that of spectral element method in the following section.

5.2 Accuracy of SEM, FDM, and FEM

A comparison is first carried out between spectral element method (SEM) and finite difference method (FDM). We considered the following one-dimensional boundary-value problem:

$$\begin{aligned} \frac{d^2 u}{dx^2} + k^2 u &= 0, \text{ in the interval } [0, 1.1] \\ \text{with } u(0) &= 1, \quad u(1.1) = e^{-jk \cdot 1.1} \end{aligned} \quad (5.1)$$

where $k = 2\pi$. We define an error measure as follows:

$$Err = \max_i \frac{|u_{i,exact} - u_{i,numerical}|}{|u_{i,exact}|} \quad (5.2)$$

where; $u_{i,exact}$ is the exact solution e^{-jkx} , and $u_{i,numerical}$ is the numerical solution obtained by the specified numerical method at the i th node in the computational domain. This definition is used throughout this thesis.

In Table-5.1, the relative errors for both FDM and SEM are shown as the number of nodes increases in both methods. Obviously, it can be observed that the errors of FDM are slowly decaying although the number of nodes is chosen in the order of 10. On the other hand, SEM shows high accuracy with much fewer number of nodes. That is, the accuracy obtained by FDM at 100 nodes can be achieved by 8 nodes with SEM.

Table 5. 1 Relative errors of SEM and FDM for the problem defined in (5.1).

FDM		SEM	
Nodes	<i>Err</i>	Nodes	<i>Err</i>
10	0.1840	7	0.0103
20	0.0524	8	0.0012
30	0.0238	9	1.4550e-04
40	0.0135	10	1.6087e-05
50	0.0087	11	2.0749e-06
60	0.0060	12	2.3081e-07
70	0.0044	13	2.5700e-08
80	0.0034	14	2.6247e-09
90	0.0027	15	2.6137e-10
100	0.0022	16	2.4206e-11
110	0.0020	17	2.3182e-12

To compare SEM with the first-order FEM, we consider the following 1D problem:

$$\begin{aligned} \frac{d^2u}{dx^2} + u = 0, \text{ in } [-1, 0], \frac{d^2u}{dx^2} + 4^2u = 0, \text{ in } [0, 1] \\ \text{with } u(-1) = \sin(-1), u(1) = \sin(4). \end{aligned} \quad (5.3)$$

In fact the solution of (5.3) is $u(x) = \sin(cx)$, with $c = 1$ in $[-1, 0]$, and $c = 4$ in $[0, 1]$. However, for error calculations, to avoid division by zero, we compute the error (only for this problem) as the maximum difference between the exact solution and the numerical solution. The comparison is shown in Table 5.2 in which nodes represent the number nodes in each sub-domain. Again, it can be seen that SEM accuracy is much higher than that of FEM. Figure 5.1 shows the plot of the solution obtained by SEM for 15 nodes in each subdomain.

Table 5. 2 Errors of SEM and FEM for the problem defined in (5.3).

FEM		SEM	
Nodes	<i>Err</i>	Nodes	<i>Err</i>
10	0.0546	7	7.0333e-05
20	0.0252	8	3.3405e-06
30	0.0164	9	4.6975e-07
40	0.0121	10	1.8764e-08
50	0.0096	11	2.5935e-09
60	0.0080	12	9.0923e-11
70	0.0068	13	1.1323e-11
80	0.0059	14	3.4817e-13
90	0.0053	15	3.9413e-14
100	0.0047	16	1.5876e-14

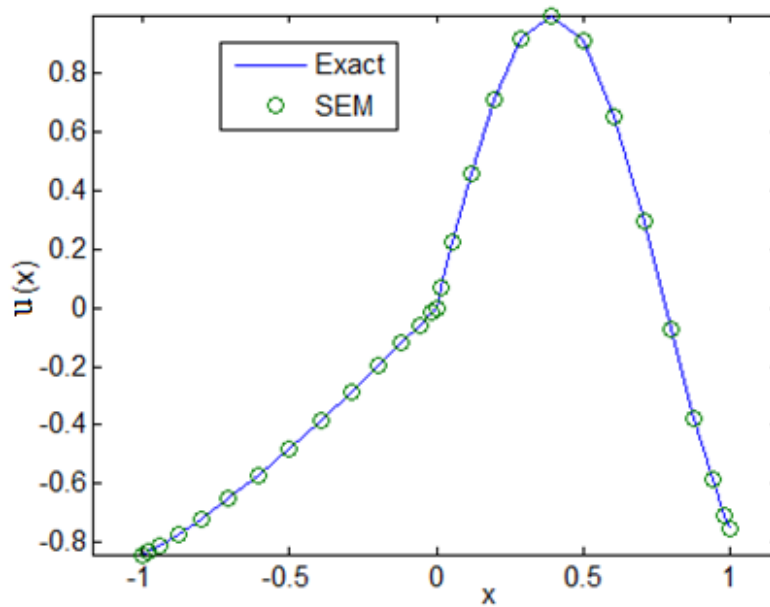


Figure 5. 1 Exact and SEM solutions of the problem (5.3).

It is worth also to compare FEM and SEM in a two dimensional boundary value problem. The point source problem (2D Green's function) is considered for this purpose. Right-triangle elements are utilized in meshing the problem over a domain of dimensions $\lambda \times \lambda$ and $\lambda = 1$. Figure 5.2 shows the solution obtained by FEM at a

grid of 20×20 . As observed from Table 5.3, the error profile in 2D doesn't differ from that of 1D case.

Next, we apply spectral element method in electromagnetic scattering problems. Although the problem defined in (5.3) and whose solution is plotted in figure 5.1 is in one dimension, it resembles domain truncation by PML from the sense that there are two differential equations governing the problem. However, the major difference in the case of problems involving PML and problem (5.3) is that there is an extra parameter that forces the field to decay inside the PML, and that parameter has to be determined as explained in the next section.

Table 5. 3 Errors of FEM for of the 2D point source problem.

FEM		SEM	
Nodes	<i>Err</i>	Nodes	<i>Err</i>
10	0.5554	7	0.00091
15	0.3229	8	1.30E-04
20	0.2018	9	1.25E-05
25	0.1356	10	1.14E-06
30	0.0967	11	1.13E-07
35	0.0724	12	1.26E-08
40	0.0562	13	1.51E-09
45	0.0447	14	2.23E-10
50	0.0364	15	2.57E-11
55	0.0302	16	3.23E-12
60	0.0255	17	2.86E-13
80	0.0145		
100	0.0103		

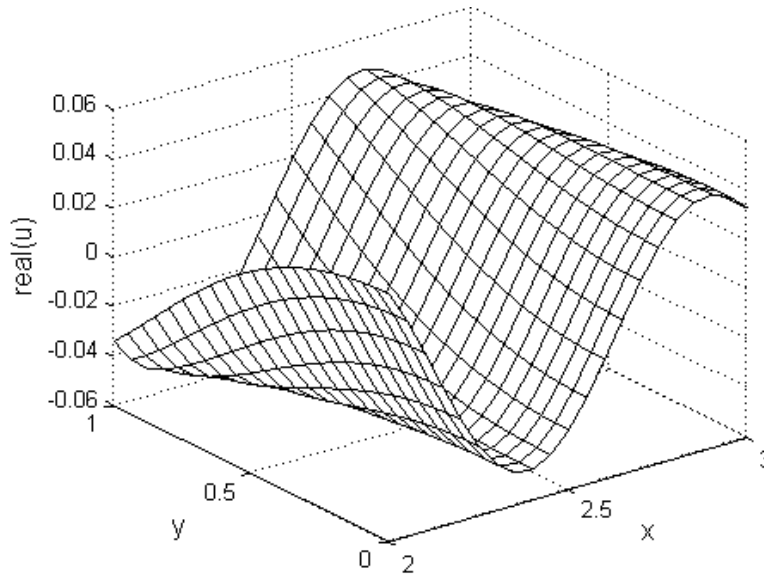


Figure 5. 2 FEM solution of the 2D point source problem (Grid: 20×20).

5.3 Determination of the Attenuation Factor

Ideally, the attenuation factor (α) must be infinitely large to make sure that the field magnitude is immediately forced to zero in the PML region. However in the numerical application, the PML must be terminated by an outer boundary and one must search for the optimum PML thickness, discretization (i.e. mesh/grid density especially in the longitudinal direction), and α , in order to represent the field decay as smoothly as possible without causing “numerical” reflections. In other words, there is a tradeoff in the choice of the attenuation factor in having almost zero Dirichlet boundary condition on the outer PML boundary and providing the adequate rate of attenuation within the PML for a specific mesh/grid.

The attenuation factor and the thickness of the perfectly matched layer are strongly connected to each other. If very small values of attenuation are chosen, then to have a successful domain truncation, one must consider a very thick perfectly matched layer. That is, the thickness and the attenuation factor are inversely proportional to each other. From theoretical viewpoint, this is correct, however, the computational aspect must be considered as well. For instance, one can choose the PML to be thick

as much as three or four times the wavelength. But to be able to resolve three wavelengths inside the perfectly matched layer, one must assign three or four times the nodes required to resolve one wavelength. This turns to cause a huge computational cost as the perfectly match layer surrounds the region of interest where the solution is to be found. In another word, the size of the perfectly matched layer is directly proportional to the size of the region of interest.

In conclusion, from computational viewpoint, there are three parameters determining the characteristics of the perfectly matched layer in order to successfully truncate unbounded domains without numerical reflections. These parameters are:

- Attenuation factor,
- PML thickness, and
- Number of nodes in the longitudinal direction.

Choosing the thickness of the PML region as much as one wavelength is very reasonable from viewpoint of the computational cost. And then, one should search for the best attenuating rate within the PML. Here, it is worth to point that one can choose the thickness even much less than one wavelength, however, since the field is decaying exponentially inside the PML, more nodes are required to resolve this decay. In addition, numerical reflection will significantly contribute to deterioration of solution corresponding to the region of interest.

For the numerical experiments, it is assumed that u is known (analytical expression is available). In figure 5.3, on $\partial\Omega_1$ and $\partial\Omega_2$, u is specified as a Dirichlet boundary condition. Throughout this work, this is referred to as “case-a”. In Ω , u satisfies the homogenous Helmholtz equation. The numerical solution is then obtained by SEM. The computational domain Ω which is shown in figure 5.4, is composed of the free-space region truncated by the perfectly matched layer (i.e., $\Omega = \Omega_{FS} \cup \Omega_{PML}$), where u is imposed on $\partial\Omega_1$ only, and on $\partial\Omega_2$ zero Dirichlet boundary condition is simply imposed. This case is referred as “case-b” in which both the homogenous Helmholtz

equation (governing the free space region, Ω_{FS}), and the PML partial differential equations (governing the PML region, Ω_{PML}) are satisfied. In this way, the SEM error without PML (case-a) and the SEM error with the utilization of PML can be compared.

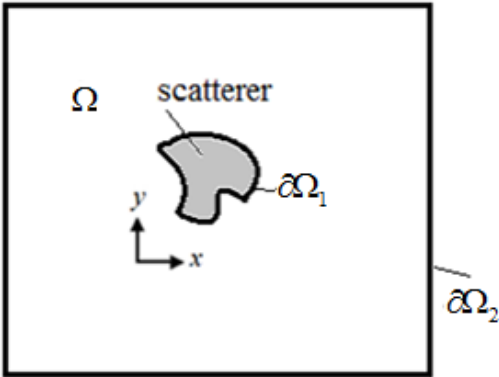


Figure 5. 3 The computational domain definition without PML.

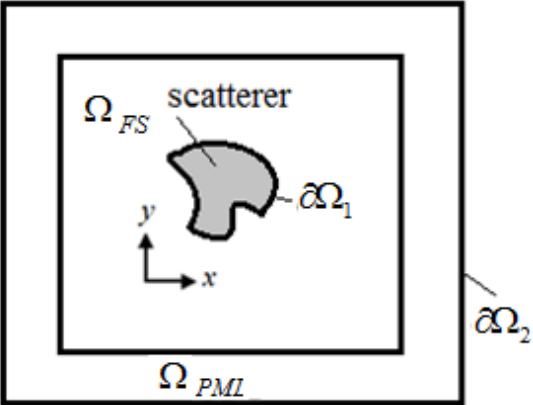


Figure 5. 4 The computational domain definition with PML.

For the sake of determining the optimum value of the attenuation factor (α) in SEM at fixed number of points per wavelength in the PML region, several problems have

been carefully studied. First, we considered the two-dimensional Green's function that has Helmholtz equation as the governing PDE:

$$\nabla^2 u + k^2 u = -\delta(\vec{r}) \quad (5.4)$$

where the solution is given in terms of Hankel function of the second kind of order zero as $u(\vec{r}) = (j/4)H_0^{(2)}(k|\vec{r}|)$. To avoid singularity arising from the radiating point source being at the origin, we truncate the domain around the origin, and impose the Dirichlet boundary condition in terms of the field $u(\vec{r})$ over the boundary $\partial\Omega_1$ as shown in figure 5.5(a). Then, to have a bounded domain, truncation by PML is applied. By utilizing symmetry, only one-fourth of the computational domain is studied. Zero Dirichlet boundary is imposed on the outer boundary of the PML region (i.e., $\partial\Omega_2$) and zero Neumann symmetry condition is imposed on the boundary $\partial\Omega_N$.

The computational domain is subdivided into eight square elements as shown in figure 5.5(b), with dimensions of $\lambda \times \lambda$ and a resolution of $N \times N$ for each element. It is worth to point that the maximum incident angle (the angle between the ray and the normal to the free space-PML interface) in this problem is 45° in terms of a ray approximation.

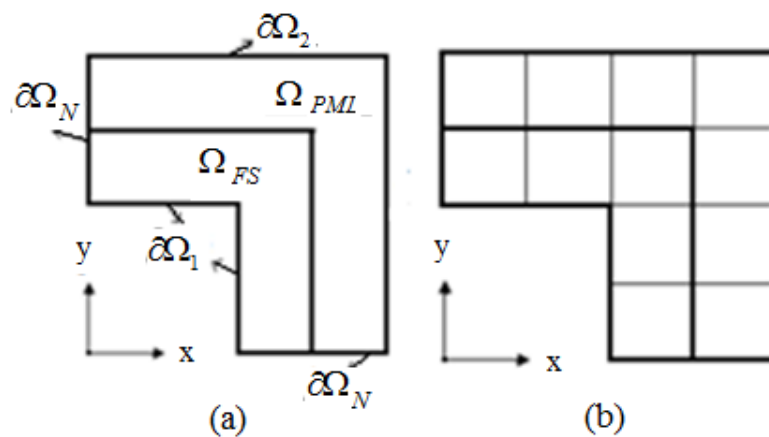


Figure 5. 5 The problem of the 2D Green's function: (a) the problem definition, (b) elements in SEM.

Table 5.4 shows the value of the attenuation factor α , and the corresponding maximum relative error for each resolution (N). The values of α were calibrated for each number of points per wavelength N, such that the minimum possible error is obtained in each case. For instance, at N=11, the variation of error vs α is demonstrated in figure 5.6.

Table 5. 4 Maximum relative errors as obtained by SEM for the problem in Fig. 5.5.

N	α	<i>Err</i>
7	4.40	4.5e-3
8	5.25	4.1746e-4
9	6.40	4.6100e-5
10	7.18	4.6486e-06
11	8.41	5.8466e-07
12	9.10	8.0365e-08
13	10.40	7.9952e-09
14	11.16	1.4402e-09
15	12.33	1.3769e-10
16	13.18	2.6012e-11
17	14.22	3.2078e-12
18	15.20	4.4765e-13

It is important to check the accuracy of SEM when it is used to solve the 2D Green's function problem again, but this time, on a different computational domain in which the inner boundary is defined to be circular. Because of symmetry (i.e., when the point source is placed at the origin), only two adjacent quadrants are studied as shown in figure 5.7(a). Here, the field $u(\vec{r})$ is imposed over the inner boundary $\partial\Omega_1$, zero Dirichlet boundary condition and Neumann boundary condition are imposed on $\partial\Omega_2$ and $\partial\Omega_N$, respectively. The elements chosen in SEM to discretize the

computational domain are shown in figure 5.7 (b) for convenience. The solutions obtained by this definition are referred as “case-b” as previously defined.

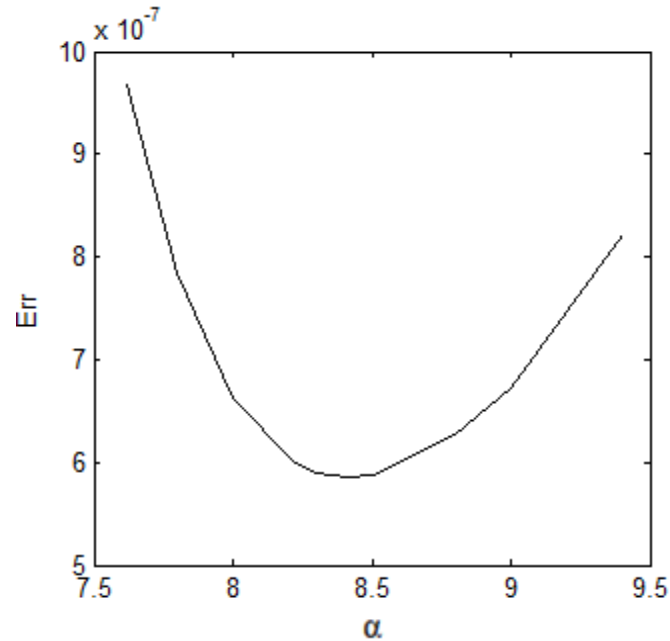


Figure 5. 6 Variation of SEM error vs α at $N=11$.

In “case-a”, simply the domain corresponding to the PML region is considered as free space satisfying the homogenous Helmholtz equation, and the field $u(\vec{r})$ is imposed over both the inner boundary $\partial\Omega_1$, and the outer boundary $\partial\Omega_2$. The errors are calculated for the following dimensions: $\lambda = 1$, $R = b = 0.5$, $d = c = 1$, and presented in Table 5.5 for both case-a and case-b. It is worth to point that the errors are larger than the ones presented in Table 5.4, this is due to the fact that we have deformed elements in this problem as discussed in chapter 3. The real part of the numerical solution is plotted in figure 5.8 both in the PML region and in the free-space region.

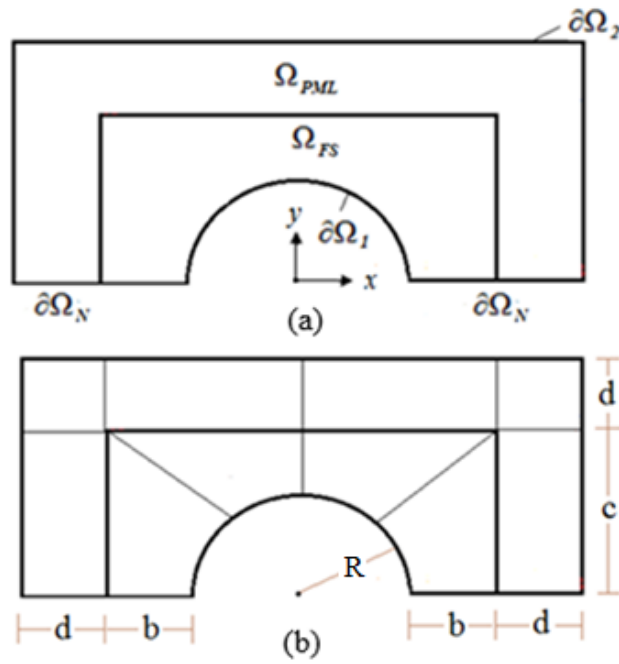


Figure 5. 7 The problem of the 2D Green's function having a circular inner boundary: (a) the problem definition, (b) elements in SEM.

Table 5. 5 Maximum relative errors obtained by SEM for the 2D Green's function problem with circular inner boundary.

N	α	<i>Err</i> (case-a)	<i>Err</i> (case-b)
7	4.40	0.003559	0.001994
8	5.25	0.000382	0.000342
9	6.40	5.24E-05	6.03E-05
10	7.18	6.92E-06	7.77E-06
11	8.41	8.50E-07	9.72E-07
12	9.10	1.06E-07	1.30E-07
13	10.40	1.29E-08	1.50E-08
14	11.16	1.32E-09	1.60E-09
15	12.33	2.44E-10	7.89E-10
16	13.18	6.37E-11	4.65E-10
17	14.22	1.71E-11	3.63E-10
18	15.20	4.62E-12	2.75E-10

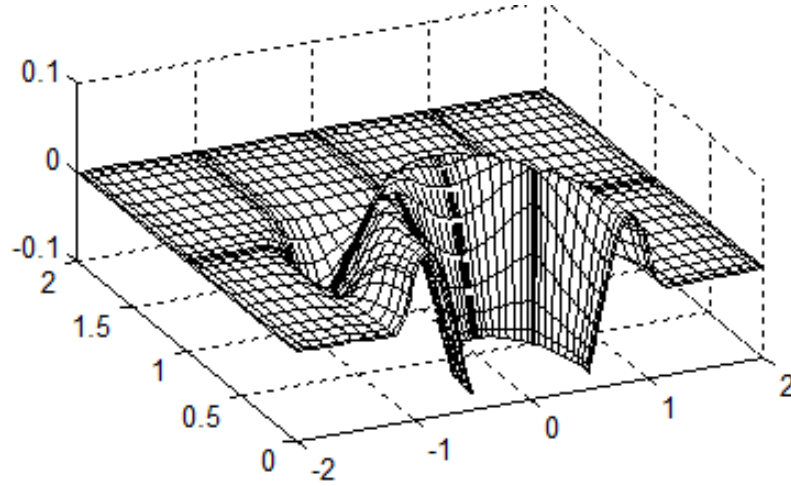


Figure 5. 8 The real part of SEM solution of the problem defined in figure 5.7.

5.4 Scattering Cylinders

Next, we have studied scattering by a circular cylinder and considered the following incident plane wave of the form $u^i = u_0 e^{-jkx}$ on an infinitely long, circular conducting cylinder of radius r_c . Because of symmetry in z-direction, the problem is a two-dimensional one, and because of symmetry along x-axis, only one half of the plane is considered. The scattered field is given analytically in terms of Bessel and Hankel functions as:

$$u^s = -u_0 \sum_{n=-\infty}^{\infty} (-j)^n \frac{J_n(kr_c) H_n^{(2)}(k\rho) e^{jn\phi}}{H_n^{(2)}(kr_c)} \quad (5.5)$$

This problem is solved as shown in figure 5.7 for the same dimensions mentioned previously. Here, for case-a, the scattered field given in (5.5) is imposed on $\partial\Omega_1$ and $\partial\Omega_2$. For case-b, the scattered field given in (5.5) is imposed on $\partial\Omega_1$ only, and zero Dirichlet boundary condition is imposed on $\partial\Omega_2$. Error results are presented in Table 5.6. As seen from the table, although we have deformed elements, the values of α still give the best accuracy when compared with the accuracy obtained in case-a. The magnitude of the solution is shown in figure 5.9 at $N \times N = 16 \times 16$ in each

element. The real part of the total electric field (scattered field and incident field) is shown in figure 5.10 at $r_c = 0.8\lambda$ using color mapping.

Table 5. 6 SEM errors for the scattering circular cylinder.

N	α	<i>Err</i> (case-a)	<i>Err</i> (case-b)
7	4.40	0.010563	0.00305
8	5.25	0.000817	0.00044
9	6.40	7.74E-05	8.02E-05
10	7.18	1.48E-05	1.63E-05
11	8.41	4.46E-06	4.51E-06
12	9.10	1.18E-06	1.18E-06
13	10.40	3.74E-07	3.80E-07
14	11.16	1.24E-07	1.27E-07
15	12.33	3.92E-08	4.78E-08
16	13.18	1.22E-08	3.22E-08
17	14.22	3.78E-09	2.64E-08
18	15.20	1.17E-09	2.21E-08

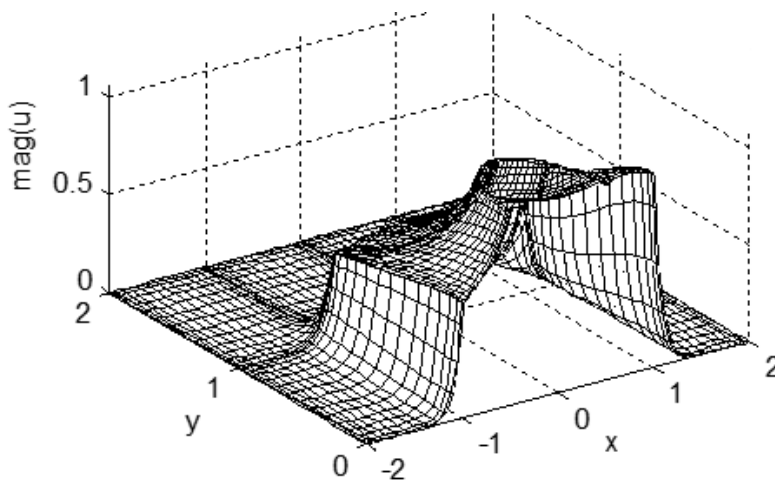


Figure 5. 9 Magnitude of the scattered field by the cylinder (i.e., $|u|$).

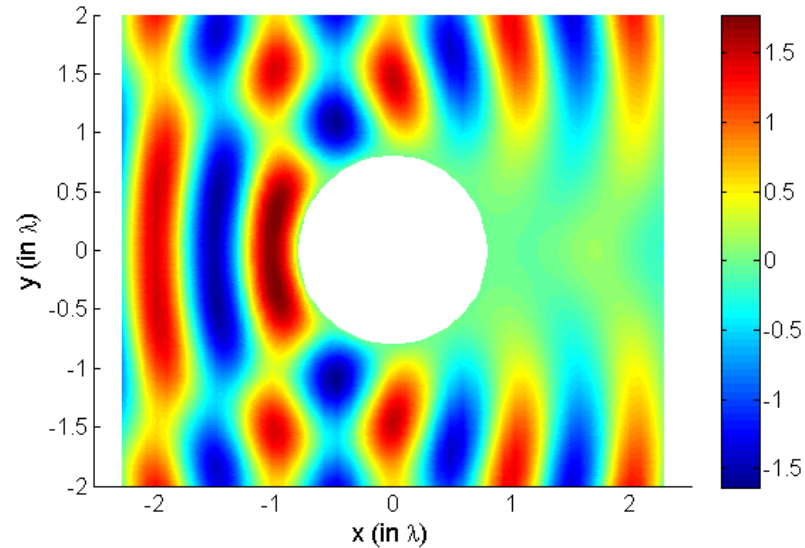


Figure 5.10 Real part of the total electric field near the cylinder at $r_c = 0.8\lambda$.

The high accuracy of spectral element method can be observed very clearly from the previous results. Although the problem discussed here is completely different from the point-source radiation problem, the optimized values of the attenuation factor still give the minimum errors in the case of scattering from a perfectly conducting cylinder. We investigated this problem in detail and tried to check whether there is a different set of values that minimizes the errors, and found no other values of attenuation that give better solutions. This is also clear from the comparison made between ‘case-a’ and ‘case-b’ presented earlier.

In practice, perfectly-conducting square cylinders are involved in many applications. For this reason, we also solve the scattered field by a perfectly-conducting cylinder (infinitely long in z-direction) of square shape although the analytical solution of such a problem is not available. Figure 5.11 shows a plane wave incident to a square cylinder of radius R , and the corresponding elemental discretization in SEM is shown in figure 5.12.

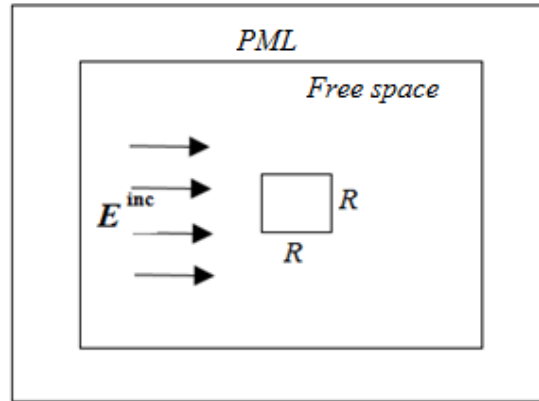


Figure 5. 11 A plane wave incident to a square cylinder of radius R .

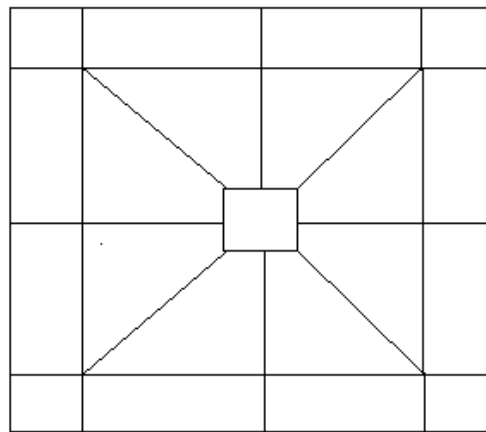


Figure 5. 12 Elemental discretization in SEM for the square cylinder problem.

In figure 5.13, the real part of the total incident-scattered field is shown in the free space region that surrounds a square cylinder of radius $R = 0.5\lambda$. It can be observed that the magnitude exceeds 1.5 although the incident plane wave has a magnitude of 1. Besides, the scattered field pattern can be better observed when a larger cylinder is of interest, for instance, the real part of the total incident-scattered field is shown in figure 5.14 at $R = 1.5\lambda$.

Next, we consider an incident plane wave propagating in xy -direction, i.e., of the form $E^{inc} = e^{-jk(x+y)}$. Again, the total incident-scattered field is plotted in figure 5.15

and figure 5.16 for $R = 0.5\lambda$ and $R = 1.5\lambda$, respectively. It can be observed that the scattered field strongly depends on the plane wave propagation direction.

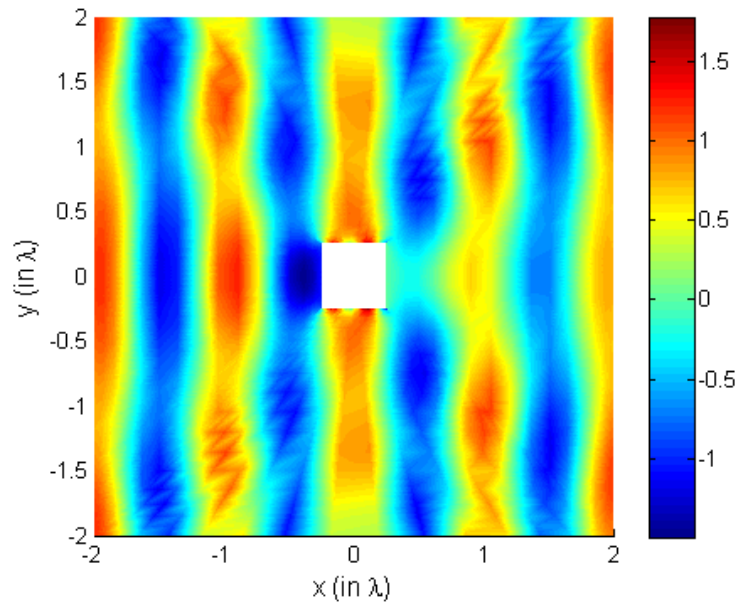


Figure 5. 13 The total field at $R = 0.5\lambda$ due to x-propagating plane wave.

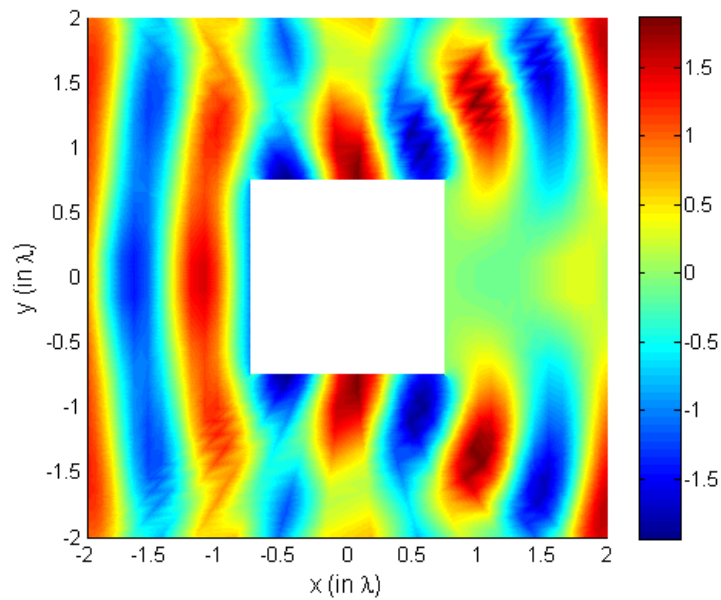


Figure 5. 14 The total field at $R = 1.5\lambda$ due to x-propagating plane wave.

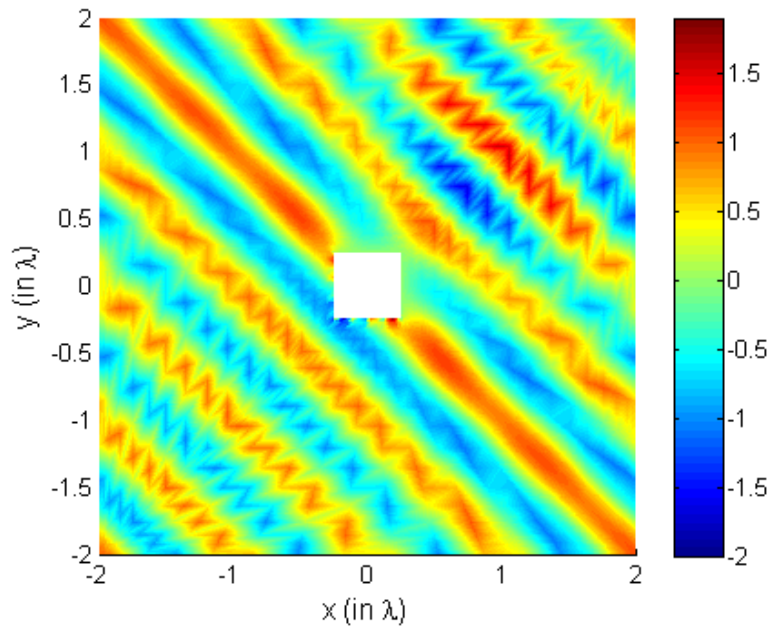


Figure 5. 15 The total field at $R = 0.5\lambda$ due to xy-propagating plane wave.

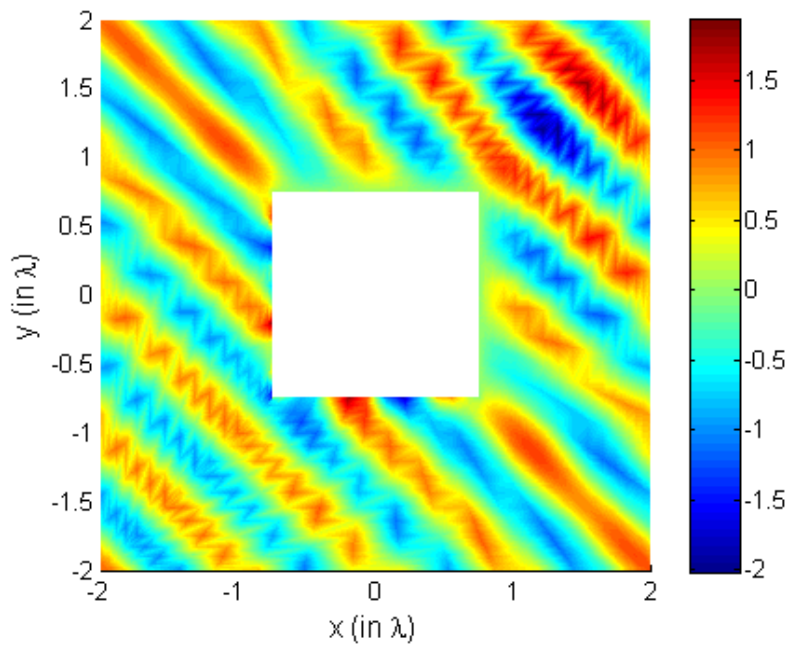


Figure 5. 16 he total field at $R = 1.5\lambda$ due to xy-propagating plane wave.

5.5 Scattering by Large Objects

To investigate SEM accuracy using the optimal values of α when scattering by large objects is encountered, we considered a square region with dimension $6\lambda \times 6\lambda$ (standing for the object dimensions) whose boundary is $\partial\Omega_1$ (where the field $u(\bar{r})$ is imposed) as shown in the left side of figure 5.10. Each of the free-space region Ω_{FS} , and the PML region Ω_{PML} , has a width of λ . The computational domain is subdivided into 64 elements so that each element is of $\lambda \times \lambda$ ($\lambda = 1$) and has a resolution of $N \times N$. The point source is chosen to be placed in 21 positions as seen from the right side of figure 5.17.

Here, we note that because of symmetry, the average relative error of these selected positions is the same as if 121 positions were chosen and distributed uniformly over the object. In each position, the problem is solved and the SEM relative error is calculated (case-b). The magnitude of the field when the point source is at position-16 is shown in figure 5.18 at $N \times N = 11 \times 11$ in each element.

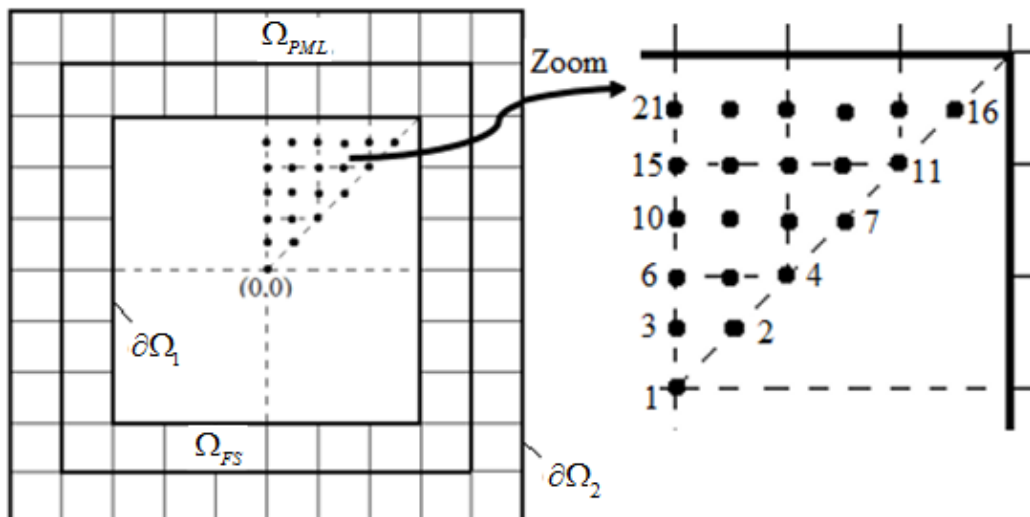


Figure 5. 17 Scattering by large objects: (on the left) the computational domain, selected positions for the point source (on the right).

From the viewpoint of ray approximation, it should be noted the maximum incident angle ranges from 45° (for position-1) to 77° (for position-16). As the incident angle gets larger, the error increases as well. The maximum relative errors for positions: 1, 11, 15, 16, are presented in Table 5.7. It can be observed from the table that the SEM accuracy is similar to the accuracy obtained in a typical boundary value problem where the PML is not utilized.

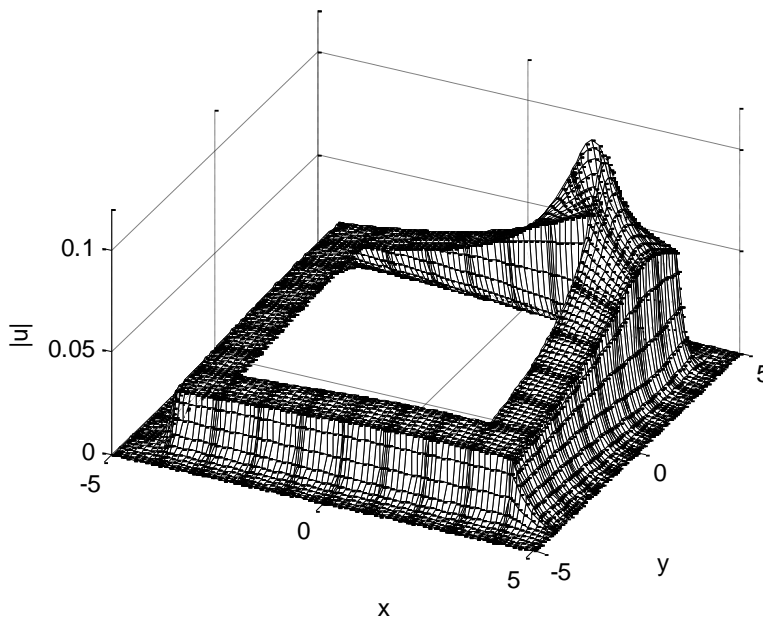


Figure 5. 18 Plot of $|u|$ for position-16 at $N \times N = 11 \times 11$.

Although the solutions are obtained by changing the position of the radiating point source whose field is governed by equation (5.4), taking the average of the maximum relative errors of all positions will give an estimate of the accuracy when a dielectric object is involved. This is due to the fact that the error in our work is normalized with the field, and the solution when a dielectric object exists can be expressed as a linear combination of Hankel functions of the second kind of order zero. In Table 5.8, the average of the errors obtained for the 21 positions are presented.

Table 5. 7 Maximum relative errors at four positions.

Max inc. angle		45°		63.4°	71.6°	77°
N	α	<i>Err</i> Posit.1 (case-a)	<i>Err</i> Posit.1 (case-b)	<i>Err</i> Posit.15 (case-b)	<i>Err</i> Posit.11 (case-b)	<i>Err</i> Posit.16 (case-b)
7	4.40	0.07012	0.005803	0.006064	0.008012	0.01413
8	5.25	0.00476	0.000463	0.000565	0.00264	0.00565
9	6.40	0.00018	5.58E-05	9.75E-05	0.000662	0.00180
10	7.18	9.41E-06	8.49E-06	2.95E-05	0.000254	0.00080
11	8.41	6.44E-07	1.00E-06	4.67E-06	5.43E-05	0.00022
12	9.10	6.64E-08	2.98E-07	1.63E-06	2.23E-05	0.00010
13	10.40	6.48E-09	2.95E-08	2.17E-07	3.92E-06	2.23E-05
14	11.16	6.04E-10	7.51E-09	6.55E-08	1.37E-06	8.90E-06
15	12.33	5.42E-11	8.86E-10	9.96E-09	2.54E-07	2.02E-06

Table 5. 8 The average of relative errors of the 21 positions.

N	α	Average <i>Err</i>
7	4.40	0.006971
8	5.25	0.001451
9	6.40	3.44E-04
10	7.18	1.32E-04
11	8.41	2.91E-05
12	9.10	1.23E-05
13	10.40	2.36E-06
14	11.16	8.71E-07
15	12.33	1.78E-07
16	13.18	7.91E-08
17	14.22	2.68E-08

5.6 One-dimensional problem

Finally, we considered the Helmholtz equation in one dimension over $x \in [-1-\varepsilon, 1+\varepsilon]$, where ε is a real number chosen as 0.001 to avoid singularity (i.e., to have the solution: $u = \exp(-jkx)$). The domain is divided into two elements each has N points and a length of $1+\varepsilon$. In the first element (i.e., $x \in [-1-\varepsilon, 0]$), the homogeneous Helmholtz equation is satisfied and in the second element (PML subdomain), the nonhomogeneous Helmholtz equation is satisfied:

$$\frac{1}{a^2} \frac{\partial^2 u}{\partial x^2} + k^2 u = 0, \text{ for } x \in [0, 1+\varepsilon] \quad (5.6)$$

with the boundary conditions $u(-1-\varepsilon) = \exp(-jk(-1-\varepsilon))$ and $u(1+\varepsilon) = 0$.

To solve this problem, we applied the same attenuation factor in order to check the accuracy. The maximum relative errors corresponding to the first element are presented in Table 5.9 for unity wavelength. The real parts and imaginary parts of the exact and SEM solutions are shown in figure 5.19 and figure 5.20, respectively, at $N = 18$ in each subdomain. It be seen from the table that SEM accuracy is high and similar to the expected accuracy in the case where the PML is not applied.

Table 5. 9 The maximum relative error of the one-dimensional problem.

N	α	<i>Err</i>
7	4.40	0.0065
8	5.25	5.1111e-04
9	6.40	6.0577e-05
10	7.18	6.0067e-06
11	8.41	7.4124e-07
12	9.10	7.1254e-08
13	10.40	8.7009e-09
14	11.16	6.5970e-10
15	12.33	1.0664e-10
16	13.18	8.8274e-12
17	14.22	1.6588e-12
18	15.20	2.3845e-13

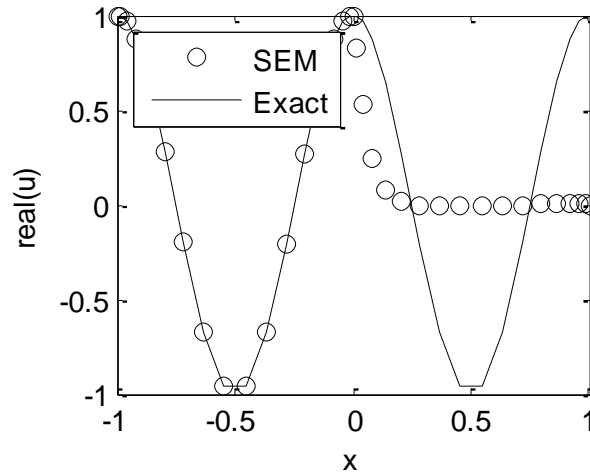


Figure 5.19 Real part of the exact and SEM solution at $N=18$.

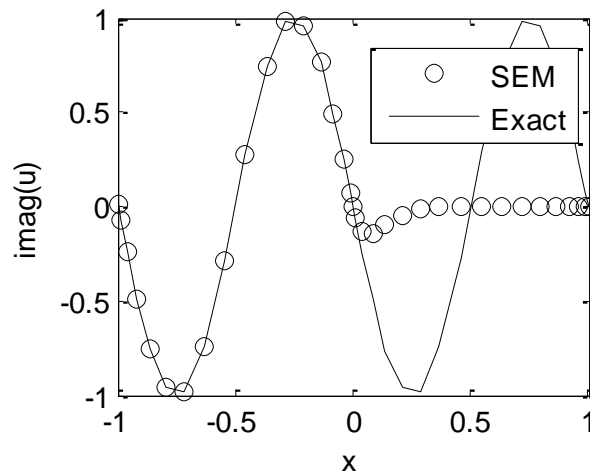


Figure 5.20 Imaginary part of the exact and SEM solution at $N=18$.

5.7 Conditioning of the System Matrix

In chapter 3, we have investigated the performance of iterative methods and some of the well-known preconditioners. However, the condition number of the resulting linear system of equations was not investigated. It is important to check the condition number of the system matrix formed by spectral element method with and without the introduction of the perfectly matched layer. In addition, it is worth to carry out a

comparison between finite element method (FEM), finite difference method (FDM) and spectral element method.

We start by comparing the condition number of FEM and SEM matrices for the two-dimensional point source problem which was solved earlier in this chapter and whose solution is presented in figure 5.2 (without PML). The comparison is presented in Table 5.10 against the number of nodes considered in each method. It can be seen from this table that in the case of FEM, the conditional number increases as the number of nodes increases. However in the case of SEM, the conditional number is less than that of FEM, and the rate of increase is less as well. This is the case where the perfectly matched layer is absent.

Table 5. 10 Condition number of 2D FEM and SEM matrices.

FEM		SEM	
Nodes	Cond(A)	Nodes	Cond(A)
10	235.1	7	196.0
15	622.4	8	285.8
20	1.2e+03	9	390.1
25	1.9e+03	10	513.8
30	2.8e+03	11	661.9
35	4.0e+03	12	840.1
40	5.1e+03	13	1.1e+03
45	6.5e+03	14	1.3e+03
50	8.1e+03	15	1.6e+03
55	9.8e+03	16	1.9e+03
60	1.7e+04	17	2.3e+03
80	2.1e+04		
100	3.3e+04		

Second, we check the condition number of the matrix formed by SEM under the application of PML. For this purpose, the point source problem for which the attenuation factor was optimized, is considered. And to check the effect of the PML (case-b), we compare the condition numbers with that of case-a where the PML is absent. This comparison is shown in Table 5.11. As seen from this table, the

condition number of the matrix when the PML is utilized is much less than that of the case where the PML is absent. This advantage of the PML is also available in the 1D problem defined in equation (5.6) as can be observed from Table 5.12.

Table 5. 11 Condition number of SEM with and without PML in 2D

N (points)	α	Cond(A) (No PML)	Cond(A) (PML)
7	4.40	7.22e+04	142.21
8	5.25	2.74e+04	220.81
9	6.40	3.54e+04	351.85
10	7.18	4.47e+04	515.15
11	8.41	5.66e+04	767.36
12	9.10	7.12e+04	1.05e+03
13	10.40	8.87e+04	1.48e+03
14	11.16	1.09e+05	1.95e+03
15	12.33	1.33e+05	2.61e+03
16	13.18	1.60e+05	3.34e+03
17	14.22	1.91e+05	4.28e+03
18	15.20	2.26e+05	5.37e+03

Table 5. 12 Condition number of SEM with and without PML in 1D.

N (points)	α	Cond(A) (No PML)	Cond(A) (PML)
7	4.40	4.34e+03	600.19
8	5.25	4.73e+03	578.58
9	6.40	7.12e+03	555.83
10	7.18	9.99e+03	543.74
11	8.41	1.35e+04	528.85
12	9.10	1.78e+04	522.23
13	10.40	2.26e+04	512.23
14	11.16	2.88e+04	507.55
15	12.33	3.57e+04	501.58
16	13.18	4.30e+04	497.98
17	14.22	5.27e+04	494.22
18	15.20	6.29e+04	491.22

Next, we investigated the condition number of the matrix formed by FDM in the 1D problem defined in equation (5.6) where the perfectly matched layer is utilized. The imaginary and the real parts of the FDM solution are shown in figure 5.21 and figure 5.22, respectively, at $N=100$ in each subdomain for $\alpha =6$ (where the minimum error is obtained). This investigation is shown in Table 5.13. The advantage of the perfectly matched layer also appears in FDM. However, when we compare the results with that presented in the fourth column of Table 5.12 (the SEM case), we clearly see that not only the introduction of the PML is computationally advantageous, but also the application of SEM as well.

Table 5. 13 Condition number of FDM with and without PML in 1D.

N (points)	Cond(A) (No PML)	Cond(A) (PML)
20	1.31e+03	206.09
30	3.869e+03	589.73
40	8.58e+03	1.28e+03
50	1.59e+04	2.38e+03
60	2.62e+04	3.97e+03
70	3.97e+04	6.16e+03
80	5.63e+04	9.03e+03
90	7.60e+04	1.26e+04
100	9.89e+04	1.71e+04
110	1.24e+05	2.26e+04
120	1.53e+05	2.91e+04
130	1.85e+05	3.67e+04

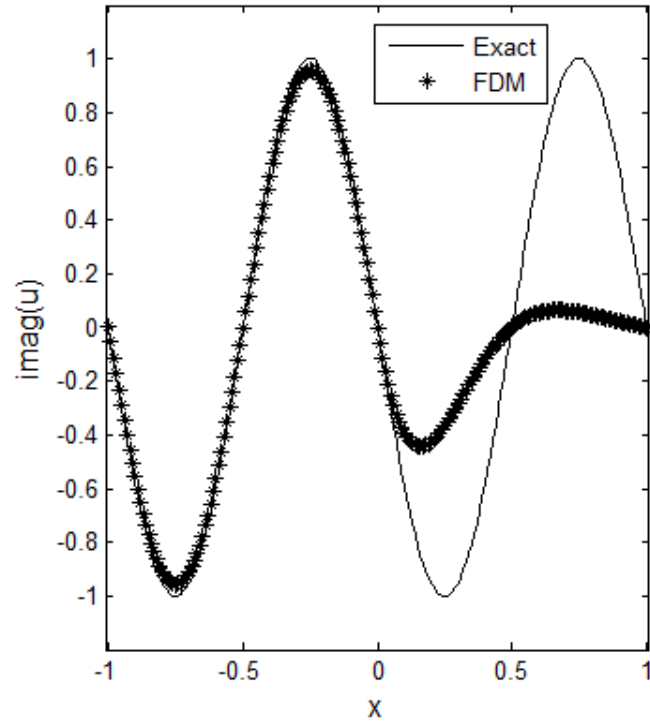


Figure 5. 21 Imaginary part of FDM solution at N=100 in each subdomain.

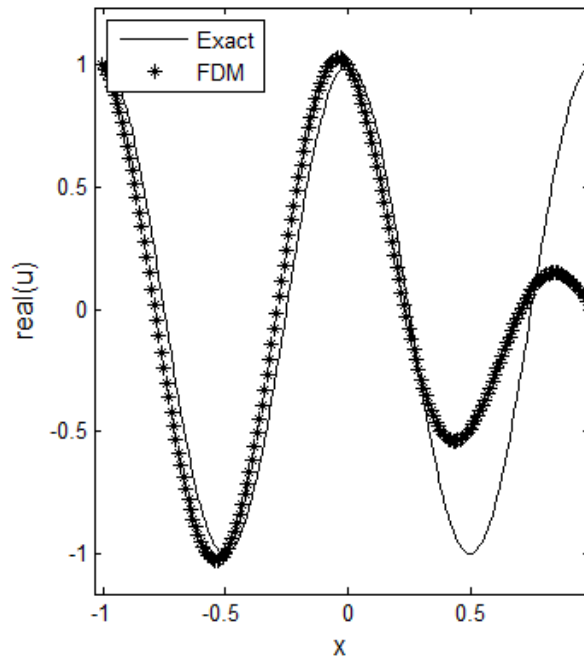


Figure 5. 22 Imaginary part of FDM solution at N=100 in each subdomain.

5.8 Conclusion

In this chapter, we carried out a comparison among spectral element method, finite difference method and finite element method in both one and two dimensional problems. As observed from the presented numerical results, the accuracy of SEM is high and can never be achieved by other low-order numerical methods.

Based on the numerical results discussed in this thesis for different geometries, it is obvious that only one PML layer is required to truncate the computational domain when spectral element method is used. Here, it is important to note that in the case of finite difference or finite element methods, more than one PML layer is usually introduced in order to reduce the numerical reflections. This in turn causes a huge burden in terms of the computational cost.

In addition, we have provided the attenuation factor versus number of nodes per one wavelength so that the best accuracy is achieved. Then, the accuracy is verified by comparing the relative errors with that calculated in the absence of the perfectly matched layer for various problems. It is also observed that the provided attenuation factor has almost a linear relationship with the number of points per wavelength (slope ≈ 0.95). Then, the accuracy of scattering by large objects is studied.

Finally, the condition number of the matrices formed by FDM, FEM, and SEM is investigated with and without the introduction of the perfectly matched layer. It is clearly observed that SEM is superior to its counterparts from computational viewpoint. In conclusion, the applicability of PML in electromagnetic scattering problems by using SEM is very successful in terms of the attenuation factors provided in this work.

CHAPTER 6

PHOTONIC NANOJET ANALYSIS

In this chapter, we numerically investigate scattering of light by a dielectric, non-magnetic cylinder by SEM. By the aid of spectral element method and the perfectly matched layer formulations presented in this work, we accurately solve scattering by dielectric microcylinders. Interesting cases, which finite difference time-domain method couldn't capture, are presented and discussed in this thesis. This chapter is arranged as follows: first an introduction to photonic nanojets (light focusing due to dielectric cylinders) is presented, we then discuss the application of spectral element method and the corresponding results of photonic nanojets. Verification of the obtained results is then presented using the analytical solution of Mie theory.

6.1 What is a Photonic Nanojet?

When an electromagnetic plane wave is perpendicularly incident to a dielectric cylinder or to a dielectric sphere, instead of having a shadow region behind the dielectric material, a photonic nanojet is obtained at some specific choices of material dimensions and a corresponding refractive index. Photonic nanojets can be defined as a narrow electromagnetic beam having high intensity. This beam propagates into the background medium, in which the dielectric material is embedded [41]. In order to obtain a photonic nanojet, the dielectric microspheres or micro cylinders must be lossless dielectric materials and of diameters greater than the illuminating wavelength. Due to the unique nature of the light distribution at the focal area, the phenomenon is named as photonic nanojet [41]-[45].

The key properties defining the photonic nanojet are [41]:

1. It is non-evanescent beam that propagate while maintaining a subwavelength full-width at half-maximum (FWHM) transverse beamwidth along a specific path that can extend more than twice of the wavelength behind the dielectric micro cylinder or microsphere.
2. Its minimum FWHM beamwidth can be as small as around one-third of the wavelength for microspheres, in another word; FWHM can be smaller than the classical diffraction limit.
3. It is a phenomenon that has a nanoresonant property. That is, it can appear for a wide range of the diameter of the microsphere or micro cylinder extending from 2 to 40 times the wavelength for a very applicable, relative refractive index (i.e., less than 2).
4. Photonic nanojets have a very high intensity which exceeds the intensity of the illuminating wave.

Photonic nanojets have several applications. They are mainly utilized in the following applications [41], [46], [47]:

- Nanospectroscopy (detection and manipulation of nanoscale objects),
- Subdiffraction resolution,
- Enhanced Raman scattering,
- Waveguiding, and,
- High intensity optical storage.

Low-loss optical wave guiding, high density data storage, lithography, high resolution microscopy, and nonlinear optical effects are the other applications of photonic nanojets [15], [48], [49].

6.2 Numerical Analysis of Photonic Nanojets

Light as an electromagnetic field interacts with different metallic or dielectric objects of any size and shape and provides novel features via scattering, reflection, refraction, and diffraction mechanisms [41], [42]. To be more specific about light interaction with an object we can assume lossless (absorption free) dielectric micro-

cylinders and excitation with a normally incident plane wave. The result of the interaction produces scattered light and strongly focused beam intensity at the back side of the medium (shadow side).

Optical engineering of micron sized dielectric cylinders and spheres produce nano-scale light manipulation. Divergence behavior of the beam whether low or high, location of the focus (inside, at the boundary or outside of the cylinder), field enhancement, and transverse dimension of the spot size compared to the illuminating wavelength (how small with respect to the wavelength) are important parameters for the photonic jet. A substantial literature has been devoted to the verification of light focusing of photonic jet into sub-diffraction-limited sizes. Squeezing light at the shadow side as well as altering the location of focal point by means of different material and structural parameters (refractive index, radius, deformation, wavelength etc.) are unique properties to create interaction between enhanced intensity and matter interaction.

Experimental observation of photonic nanojets generated by latex microspheres of varying diameters was reported in Ref. 46 (See figure 6.1). Low loss optical guiding of light can be accomplished by touching microspheres [49]. Propagation losses as low as 0.08 dB per microsphere was measured in the same study.

Photonic nanojets have been mainly explored by numerical methods based on FDTD analysis [15], [16]. For instance, figure 6.2 shows a visualization of a photonic nanojet as obtained by FDTD for a plane-wave-illuminated circular dielectric cylinder of $5 \mu\text{m}$ diameter at a wavelength of 5 nm . The cylinder is embedded in vacuum and has a refractive index of 1.7. Very fine meshes are required in order to get accurate and reliable results with FDTD method. Besides, the excitation mechanism such as plane wave in free space may restrict the observation of special resonance modes. Later, analytical and semi-analytical attempts were introduced in the literature [42]. The majority of analytical studies are based on Mie theory. Rigorous Mie theory was used to analyze the fundamental properties of the photonic

nanojet in [42]. Recasting eigenfunction solution of the Helmholtz equation into a Debye series. [16] provided detailed optics of photonic nanojets on dielectric cylinders.

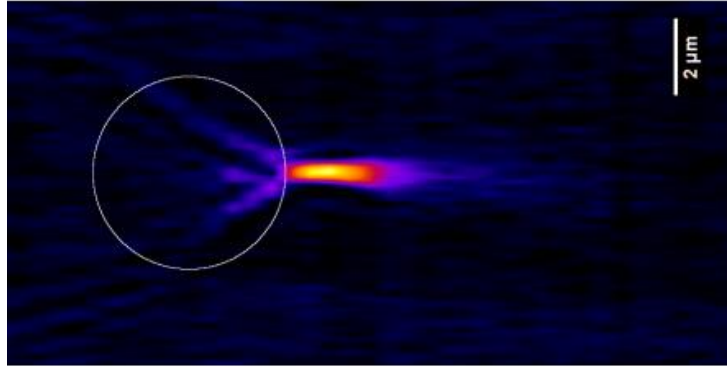


Figure 6. 1 Experimental observation of a photonic nanojet viewed along the optical axis of a $5 \mu\text{m}$ -diameter dielectric sphere made of glass, [46].

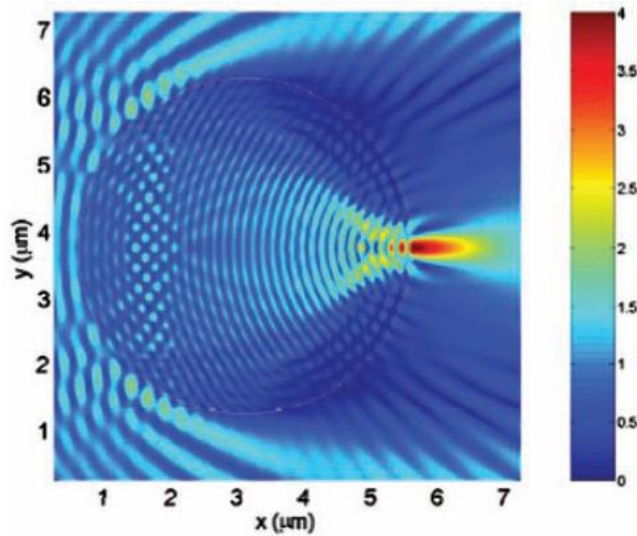


Figure 6. 2 Visualization of a photonic nanojet of a plane-wave-illuminated circular dielectric cylinder of $5 \mu\text{m}$ diameter and has a refractive index of 1.7. [15].

As mentioned previously to have accurate results with FDTD method it is necessary to use finely discretized mesh which is a huge burden on the computational

resources. Therefore, it is important to check/verify results with an alternative numerical method. In the present work, we implement the spectral element method to solve for the scattered electric field inside and outside the dielectric cylinder.

6.3 Nanojet Analysis by Spectral Element Method

In the case of photonic nanojet where the scatterer is assumed to be an infinitely-long dielectric cylinder, the problem can be considered as a two-dimensional one when an incident plane wave propagating in a direction perpendicular to the cylinder axis is assumed. We consider an incident plane wave propagating in x-direction and the electric field is polarized in z-direction (i.e., in a transverse magnetic mode (TMz)):

$$E_z^{inc} = \hat{a}_z \exp(-jkx) \quad (6.1)$$

To solve the problem numerically, we should truncate the unbounded domain. Again, the formulation of the perfectly matched layer presented in chapter 2 is utilized for the domain truncation. Figure 6.3 shows, in the xy-plane, a dielectric cylinder represented by Ω_C , free space region represented by Ω_{FS} , and the PML region denoted by Ω_{PML} , which represents the region surrounding Ω_{FS} . On the outer boundary of Ω_{PML} , zero-dirichlet boundary condition is simply imposed. In Ω_{FS} , the homogenous Helmholtz equation is satisfied:

$$\nabla^2 E_z^s + k^2 E_z^s = 0, \quad (6.2)$$

in which E_z^s stands for the scattered electric field and polarized in the z-direction (TMz polarization is considered), and k is the wave number. While in Ω_C , the following Helmholtz equation can be derived:

$$\nabla^2 E_z^s + k^2 \epsilon_r E_z^s = k^2 (1 - \epsilon_r) E_z^{inc}, \quad (6.3)$$

where; ϵ_r is the relative permittivity, and E_z^{inc} represents the incident plane wave. Throughout this work, we assume that the medium is non-magnetic ($\mu_r = 1$). In Ω_{PML} , the set of partial differential equations derived in chapter 2 must be satisfied.

Under these assumptions, the refractive index is related to the relative permittivity as follows:

$$n = \sqrt{\varepsilon_r}. \quad (6.4)$$

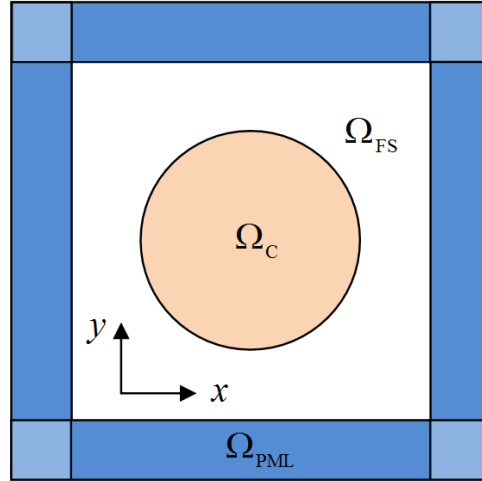


Figure 6. 3 Definition of the computational domain composed of a dielectric cylinder (Ω_C) embedded in the free space (Ω_{FS}) and truncated by PML.

Before we proceed further, it is worth to mention that the scattering dielectric cylinder is embedded in the free space that has a unity refractive index. From practical viewpoint, the cylinder can be embedded in another dielectric material that has a refractive index different than one, but it should be less than that of the scattering cylinder in order to obtain a photonic nanojet. What is important here is that the effective refractive index (n_{eff}) which is expressed by:

$$n_{eff} = \frac{n_C}{n_m}, \quad (6.5)$$

where; n_C and n_m are the refractive indices of the cylinder and the surrounding material, respectively. In this work, we assume that the surrounding material is free space and we denote the effective index by n which, in turn, is the refractive index

of the scattering cylinder. The radius of the cylinder, denoted by R , is normalized with the wavelength λ .

A possible discretization of the computational domain by spectral element method when the dielectric cylinder radius is $R = 3.5\lambda$, is shown in figure 6.4. In this figure, the GLL nodes are chosen as $N \times N = 9 \times 9$ in each element for demonstration purpose. However in this work, finer resolutions are considered depending on R , for instance, when $R = 3.5\lambda$, the grid size of 30×30 in each element is considered when the domain elements are chosen as shown in figure 6.4 in order to achieve approximately 14 points per wavelength). It is important to mention that the number of elements should be increased as the radius of the cylinder increases due to the grid distribution of GLL nodes and since the radius is normalized with the wavelength.

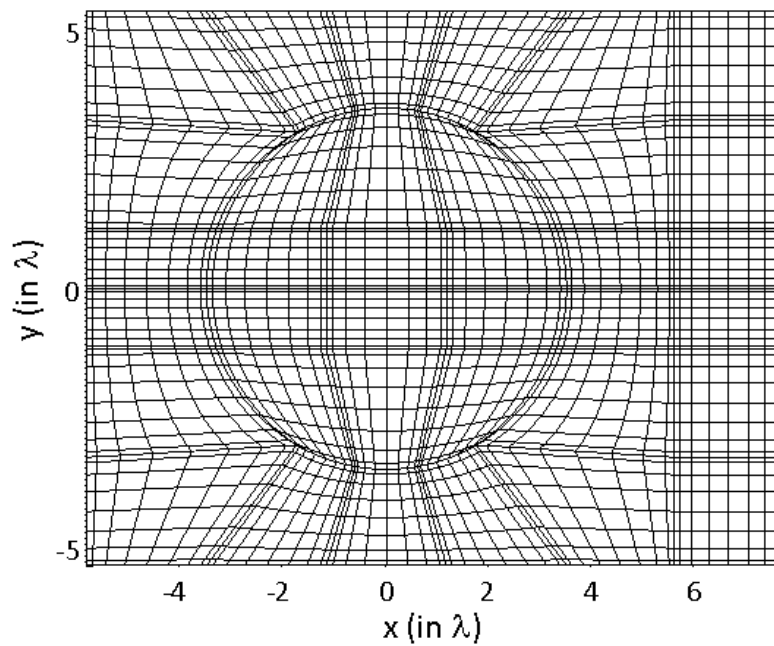


Figure 6. 4 A possible discretization of the computational domain at $R = 1.5\lambda$, and $N \times N = 9 \times 9$ for each element (here, only elements corresponding to Ω_{FS} and Ω_C are shown).

Typical field solutions of photonic nanojets obtained by spectral element method are shown in figure 6.5 for the cylinder radius $R = 3.5\lambda$, and for a refractive index $n = 1.6$. The plots in this chapter are illustrated using color map. In figure 6.6, the photonic nanojet in figure 6.5 is shown 3D. Figures 6.7 and 6.8 illustrate different photonic nanojets at $(R = 5\lambda, n = 1.6)$ and at $(R = 6.5\lambda, n = 1.4)$, respectively.

It is worth to mention that, after obtaining the solution by spectral element method, which represents the scattered field, the incident plane wave is added to the scattered field in the subdomains Ω_C and Ω_{FS} only. One can produce the same spatial light distribution for the case where FDTD method is used. We have performed FDTD study and verified the exact photonic nanojet creations. With the application of SEM in frequency domain, it is easy to decompose the total field into incident and scattered field components.

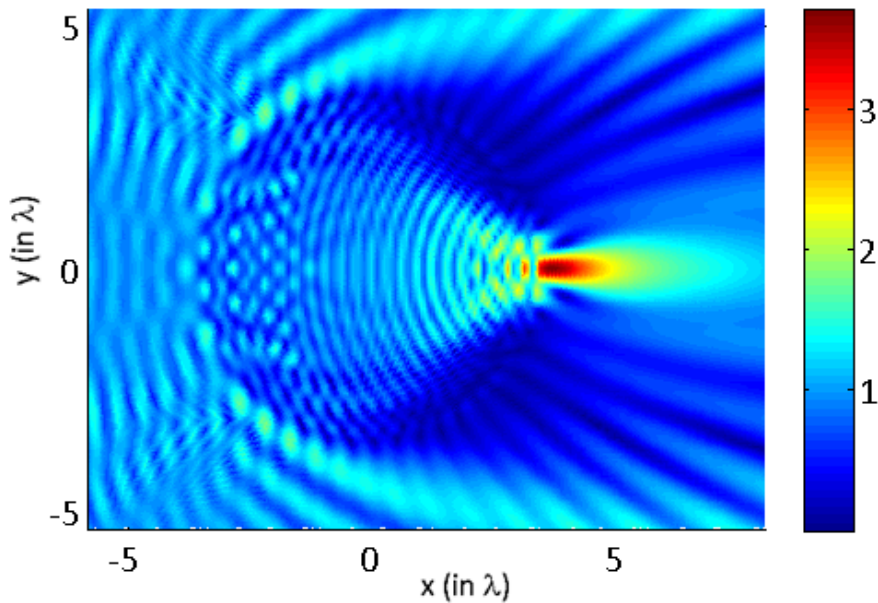


Figure 6. 5 Visualization of photonic nanojet at $R = 3.5\lambda$ and $n = 1.6$.

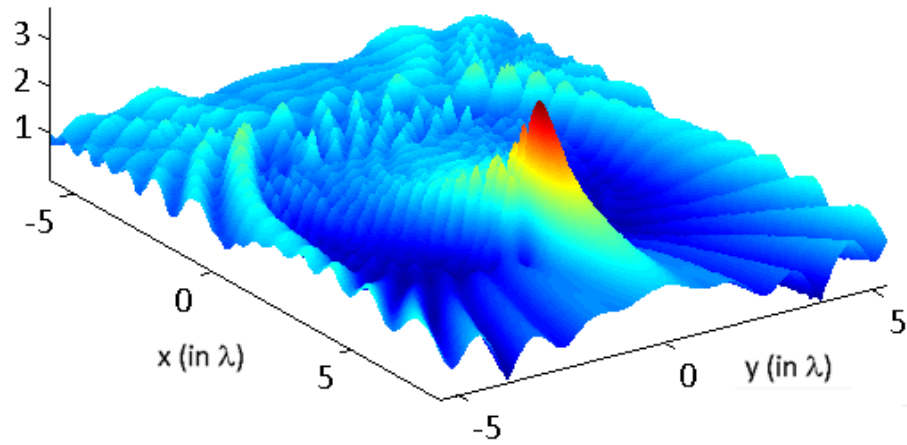


Figure 6. 6 3D visualization of photonic nanojet at $R=3.5\lambda$ and $n=1.6$.

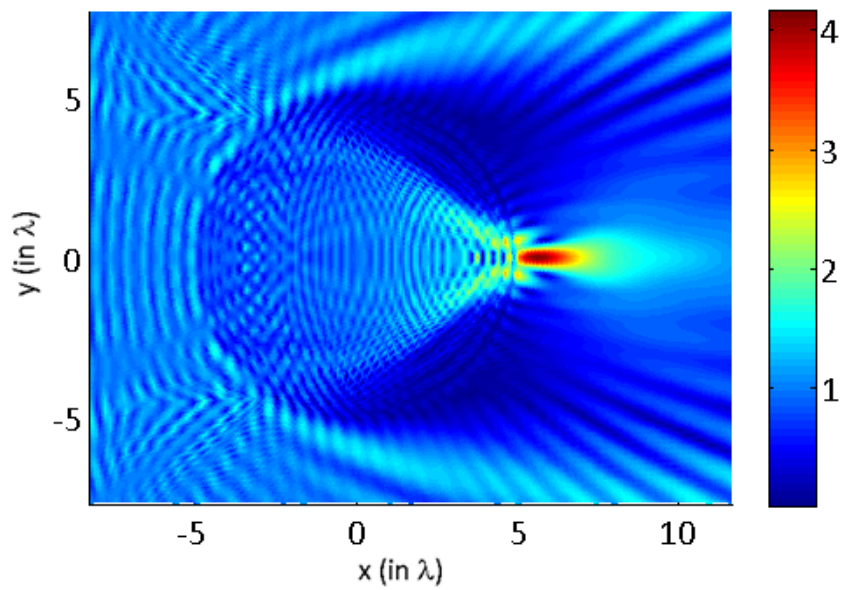


Figure 6. 7 Visualization of photonic nanojet at $R=5\lambda$ and $n=1.6$.

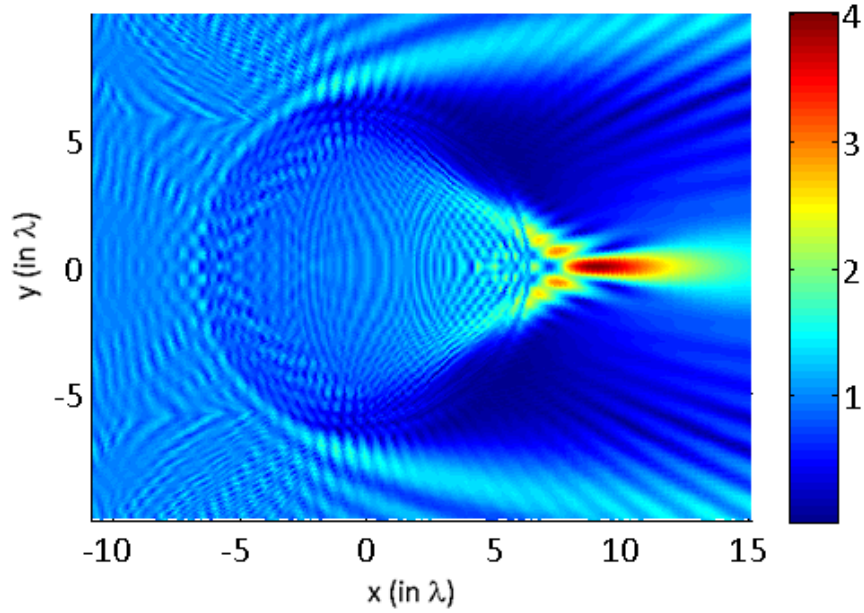


Figure 6. 8 Visualization of photonic nanojet at $R = 6.5\lambda$ and $n = 1.4$.

The results presented in the previous figures demonstrate the capability of spectral element in the analysis of photonic nanojet generation. The input source interacts with the cylindrical object and gets focused at different locations as we change the radius and refractive index of the dielectric material. The focal point appears close to the surface in figure 6.5 and it moves away from the back side along the optical axis ($y=0$ line) in figures 6.7 and 6.8.

Plane wave illumination of dielectric micro cylinders with FDTD method always produces an expected lensing/focusing effect so that the planar wave front of light gets tilted and focused at the optical axis. In the next example, we try to emphasize the advantage of SEM analysis over FDTD method. For example, when we change the refractive index of the cylinder and keeping the radius constant at 3.50λ a resonance mode appears.

Figure 6.9 shows one of the captured resonance mode supported by a dielectric micro cylinder with $R = 3.50\lambda$ and $n = 1.7$. The light focusing action with weak amplitude can be seen at the interior part of the cylinder. On the other hand, strong field

localization at around the small cylinder appears with a highly symmetric light distribution in the form of two rings. Light is trapped by total internal reflection. Similarly, when we change the radius of the cylinder to $R=4.50\lambda$, the resonance mode again occurs if the refractive index value becomes 2.0. The result is presented in figure 6.10. Light distribution with five rings is highly symmetric and strong field localization takes place at the exterior part of the micro cylinder. The evanescent field that leaks out of the dielectric cylinder radially is apparent in the plot.

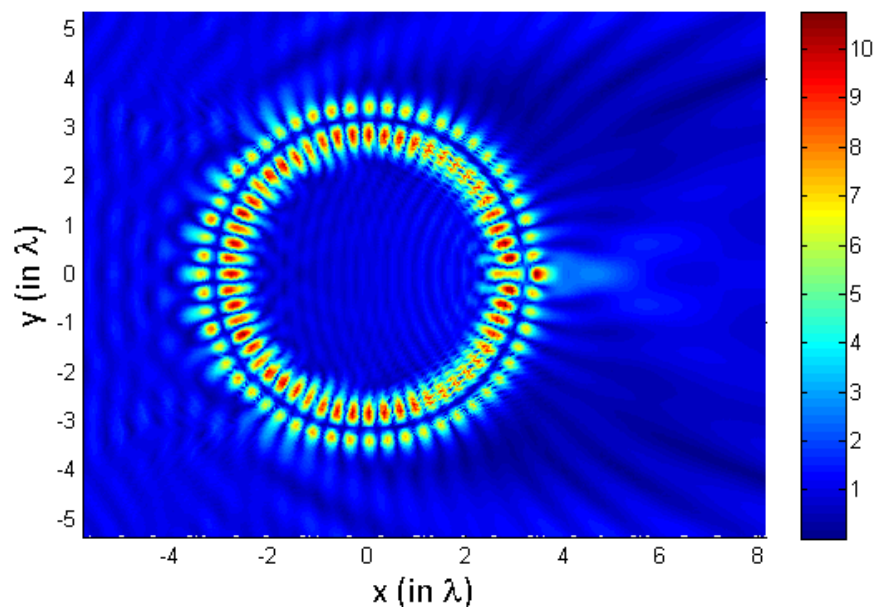


Figure 6. 9 Visualization of the evolution of a photonic nanojet for $R = 3.50\lambda$ and $n = 1.7$. WGM representation gives $m=28$ and $I = 2$.

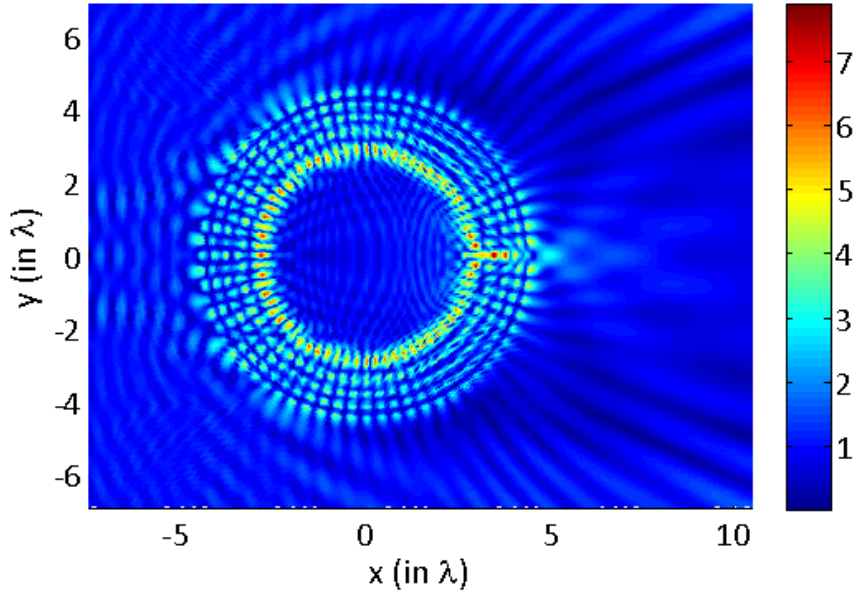


Figure 6.10 Visualization of the evolution of a photonic nanojet for $R = 4.50\lambda$ and $n = 2$. WGM parameters are $m=34$ and $I = 4$.

Special cases corresponding to specific radius and refractive index values in the figures 6.9 and 6.10 can be attributed to whispering gallery mode (WGM). In the representation of WGM, m indicates the azimuthal mode number I and radial mode number. The resonance mode with different mode number is confined to the circumference of the cylinder by means of the total internal reflection mechanism. Using that notation we can express figures 6.9 and 6.10 in terms of WGM resonances. By means of spectral element method we captured resonance modes as well as photonic nano jets cases. Commonly used FDTD method requires a different excitation scheme in order to gather the resonance modes of the micro-cylinder apart from the plane wave illumination.

We should point out that FDTD method gives us regular light focusing behavior but it does not indicate the creation of resonance mode. For instance, we have solved the problem at $R = 3.50\lambda$ and $n = 1.7$ by FDTD method using MEEP (a FDTD-based software developed by Massachusetts Institute of Technology-MIT). The corresponding real part of solution is shown on figure 6.11. The plot is obtained by meshing the domain uniformly such that 40 nodes are used per one wavelength.

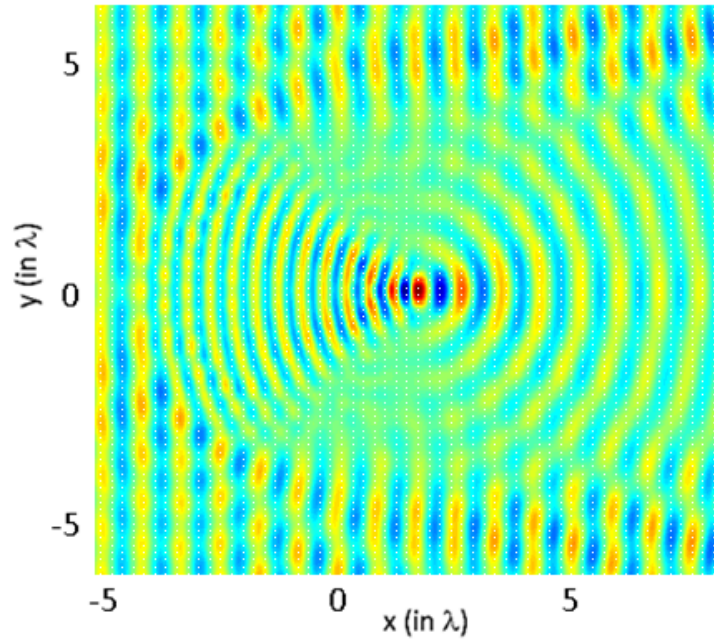


Figure 6. 11 FDTD visualization of the evolution of a photonic nanojet for $R = 3.50\lambda$ and $n = 1.7$.

Phase matching condition has to be satisfied for FDTD method in order to excite the resonance mode. That condition requires special coupling techniques such as waveguide coupling or tapered optical fiber to excite the mode. The downside of the coupling approach is that the micro-resonator gets disturbed and the true resonance mode is modified due to the presence of the external waveguides.

6.4 Verification of Whispering Gallery Modes

Photonic nanojet analysis can be performed analytically. Mie theory was intensively utilized in electromagnetic scattering problems. However, when the characteristic dimensions of the scattering object becomes much larger than the wavelength, improper algorithms may lead to considerable numerical errors [16]. In the examples presented in the previous section, where resonance takes places, the diameter of the micro-cylinder is larger than the wavelength but not too much. It is very important to

check whether the analysis that Mie theory provides produces such resonance cases or not.

Itagi and Challener [16] provided the solution of the scattered light by a dielectric cylinder using Mie theory. Although their derivation is based on transverse magnetic mode (TE), we will use this analytical solution to verify our results. By Mie theory, the total-incident scattered magnetic field inside the cylinder can be expressed as:

$$h(\rho, \phi) = \sum_{m=0}^{\infty} a_m \cos(m\phi) J_m(nk\rho) \quad (6.6)$$

where; ρ is the Euclidean distance from the z-axis to a point lying inside the cylinder, ϕ is the azimuth angle, J_m denote Bessel function of the first kind of m th order, and k is the wavenumber. The coefficients a_m are defined as:

$$a_m = c_m n \left[\frac{H_m^{(1)'}(kR) J_m(kR) - H_m^{(1)}(kR) J_m'(kR)}{n H_m^{(1)'}(kR) J_m(nkR) - H_m^{(1)}(kR) J_m'(nkR)} \right], \quad (6.7)$$

in which R denotes the radius of the cylinder, $H_m^{(1)}$ is Hankel function of the first kind of m th order, ' denotes the derivative with respect to the argument of the function, and the coefficients c_m are given as:

$$c_m = \begin{cases} 1, & m = 0 \\ 2j^m, & m > 0. \end{cases} \quad (6.8)$$

This analytical solution is derived under the assumption that the cylinder is centered at the origin of the xy-plane. With the aid of this analytical solution, the magnitude of the magnetic scattered-incident field inside the cylinder is plotted for $R = 4\lambda$ and $n = 1.4$ in figure 6.12. Here, we note that the truncation of the series at $m = 150$ has negligible effect on the solution.

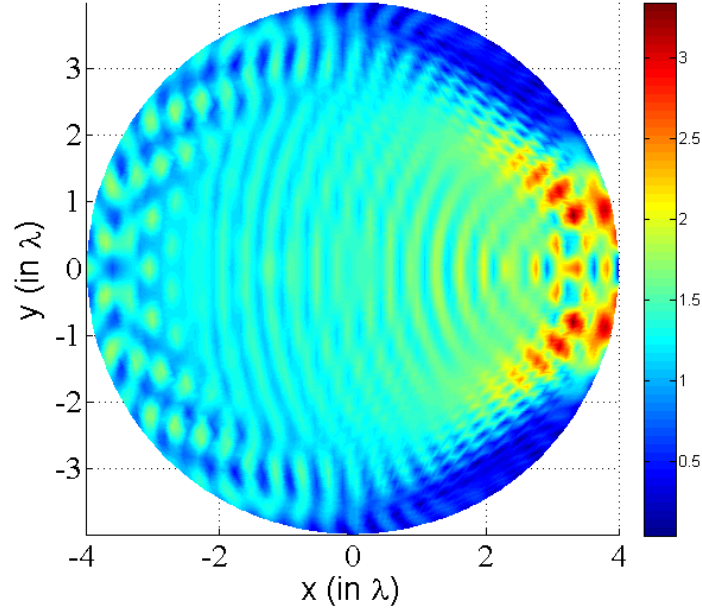


Figure 6. 12 Magnitude of magnetic scattered-incident field inside the cylinder for $R = 4\lambda$ and $n = 1.4$.as obtained by Mie theory.

Considering that the accuracy of spectral element method is very high, and one of the resonance cases is captured at a refractive index of $n = 1.7$, we have solved the problem at the neighborhood of $n = 1.7$, for instance at $n = 1.701$ and at $n = 1.699$, and the expected photonic nanojets were captured. So the index $n = 1.7$ is very critical. It should be noted that since the cylinder radius is larger than the wavelength, Mie theory provides an approximate solution instead of the exact solution.

In other words, the solution obtained by Mie theory shows that there is no resonance at 1.7. We have performed a search loop in the neighborhood of 1.7 and captured the same resonance cases obtained by spectral element method. Figures 6.13 and 6.14 show the magnitude of the total magnetic field inside the cylinder at ($R = 3.5\lambda$ and $n = 1.6905$), and at ($R = 4.5\lambda$ and $n = 1.8911$), respectively.

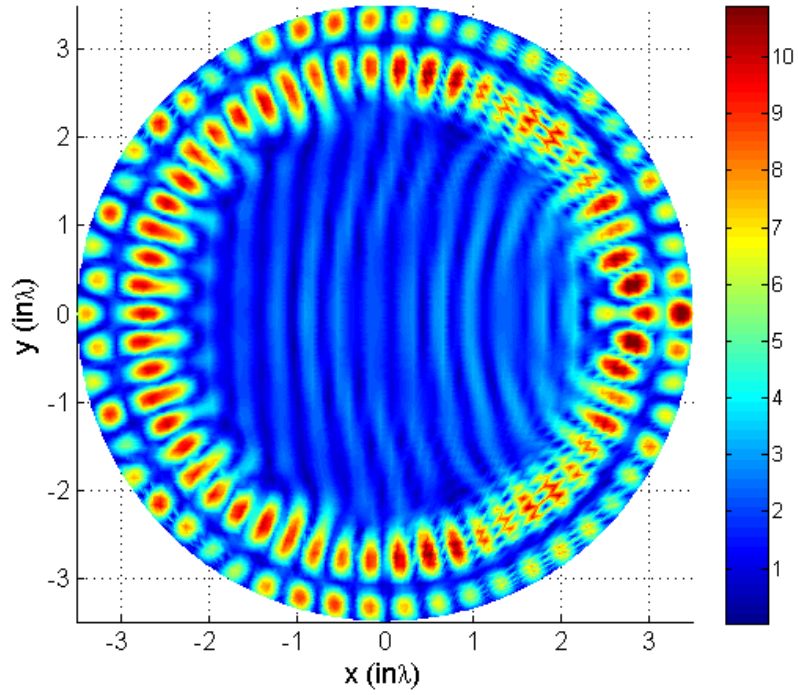


Figure 6. 13 The magnitude of the total magnetic field inside the cylinder at $R = 3.5\lambda$ and $n = 1.6905$.

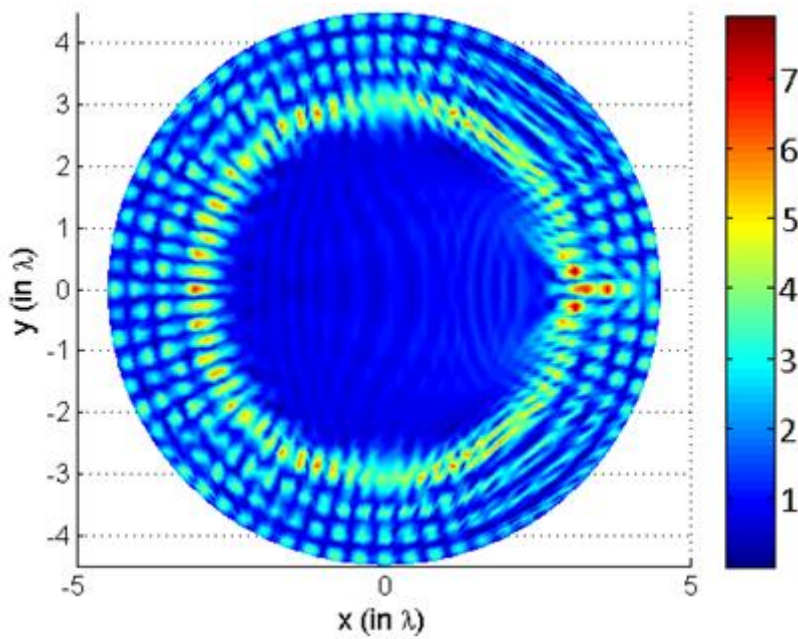


Figure 6. 14 The magnitude of the total magnetic field inside the cylinder at $R = 4.5\lambda$ and $n = 1.8911$.

6.5 Conclusions

The formulation of perfectly matched layer is also utilized together with SEM formulation. In addition, accuracy of SEM is demonstrated by solving for the scattered field from perfectly conducting cylinders. With the use of SEM, we could accurately perform field analysis of photonic nanojets in dielectric lossless micro cylinders. Strong light focusing at the shadow side of the micro-cylinder is reported. Advantageous features of SEM allow the observation of commonly reported nanojet scenarios as well as the least pointed out transition region where resonance mode appears under certain conditions. The creation of whispering gallery mode types is plainly observed. One may be unaware of these special modes under the case of plane wave illumination with FDTD method that needs a coupling technique to excite the resonance the mode.

Previously reported results are exactly reproduced in the current study that validates the accuracy of the formulation and implementation of the numerical analysis based on SEM. The most important is the observation of the unique light distribution property that is associated with a resonance mode behavior. Depending on the parameters of the micro-cylinder, radius (R) and refractive index (n) strong field enhancement occurs and different number of rings appears within the cylinder. These features can be attributed to whispering gallery modes supported in micro-discs. The captured whispering gallery modes by spectral element method have also been verified using solution by Mie theory.

CHAPTER 7

CONCLUSIONS

We have solved in this work the partial differential equations that govern the free space region when interaction between electromagnetic fields exists, and the equations that govern electromagnetic radiation and scattering by using SEM. In addition, domain truncation based on the PML is employed in the process. The numerical simulation is carried out in frequency domain.

In most of practical engineering problems, the geometry of the region of interest is irregular. This means that discretization of the problem into elements of regular shapes is impossible. Spectral element method gives the capability of using deformed elements; and hence, a freedom in modeling irregular problems. For this reason, we illustrated the accuracy of this numerical method for single-deformed element case in order to emphasize the effect of elemental deformation and aspect ratio. This last point is important, since while discretizing a problem into elements having various aspect ratios, the element with the largest aspect ratio is going to effect the overall accuracy of spectral element method. Based on this illustration, we conclude that elements forming an electromagnetic problem should be chosen such that their aspect ratios are close to unity as much as possible in order to preserve the high accuracy offered by spectral element method.

To realize and appreciate the accuracy of spectral element method, we carried out a comparison between this method and its well-known counter parts such as finite difference and finite element methods. The comparison included two major targets; the first is the accuracy. For this purpose, we applied these numerical methods to solve specific problems and the corresponding error calculations are subjected to a

specific error measure. From the illustrated examples, it is clear that the accuracy of spectral element method is much higher than that of its counter parts.

The second is to assess the condition number of the matrices formed by these three numerical methods. It was clear that conditioning of the system matrices formed by spectral element method is less than that of the other methods with or without the application of the perfectly matched layer due to the smaller size of the system matrices for the same accuracy. In addition, the condition number in the case of spectral element method when the perfectly matched layer is applied was less than that of the case without PML is introduced.

In the context of the perfectly matched layer formulation presented in this work, the optimum values of the attenuation factor are provided. This optimality is obtained under the assumption that the PML thickness is of one wavelength of the incident plane wave. As discussed in this thesis, the trade-off between having a fast field decay (so that the field vanishes at the outer boundary of the PML) and being able to resolve this decay from the computational viewpoint is the key behind the idea of optimizing the values of the attenuation factor. The second supporting point is that since the elemental discretization of the PML region is of regular shapes and the grids are of Gauss-Legendre-Lobatto (GLL) type, the attenuating factor depends on the number of GLL points in the longitudinal direction of propagation. Here, it is worth to note that there is a particular optimum value of the attenuation factor at which the error is minimized.

Based on these optimized values of the attenuation factor, we have presented the corresponding maximum relative difference between the analytical solution of the point source problem and the solution obtained by the spectral element method. The numerical solution is obtained by directly imposing the analytical solution on the exterior boundary of the computational domain without introducing the perfectly matched layer. Several numerical experiments are performed such as the radiation problem on curved-side boundaries and scattering by an infinitely-long perfect

conducting cylinders of both circular and square shapes in order to test the optimality of the proposed attenuation factors. This comparison shows that the proposed attenuation factors for several numbers of points per wavelength are in fact optimum.

Providing the optimal attenuation factors is one of the main results in this work. However, these values are specific to the case where the spectral element method is used. Due to different character of finite difference method or finite element method these optimal values generally will not be applicable with those methods. The optimum values of the attenuation factor are then utilized to numerically solve the scattered field by a dielectric micro cylinder. The resulting solution at specific choices of cylinder diameter and the refractive index of the cylinder gives the so-called photonic nanojet. Several demonstrations of photonic nanojets are presented and discussed for different diameters and refractive indices.

The accuracy of the spectral element method is very high as it can be observed from the presented numerical demonstrations when compared with its counter parts such as finite element or finite difference methods. Here, it is important to ask the following question which is very interesting for an engineer: Does an engineer need to solve the problem with a relative error of 10^{-10} or even 10^{-5} ? In fact, many text books answer this question by “No”. In some sense, this answer seems to be logical since an electrical engineer, for instance, seeks an accuracy of 10^{-3} while designing an electrical motor or generator for example. Hence, low-order finite element method or finite difference method are very suitable and do meet engineering purposes. However, based on Chapter 6, the answer to the above question is “Yes”, we do indeed need high accuracy in some cases. That is, when low-order numerical methods are used to study electromagnetic scattering by dielectric microspheres or micro cylinders, whispering gallery mode will be missed. So, if the engineer design the material based on the numerical solution from a low-order method, and if whispering gallery mode takes place in the final implementation, the whole design will be in jeopardy.

Further, the resulting linear, symmetric system of equations formed by spectral element method is also solved iteratively. The conjugate gradient method, biconjugate gradient, and the generalized minimum residuals are implemented to solve the resulting system. In addition, several preconditioners such as Jacobi, incomplete LU factorization, and symmetric successive over relaxation are utilized, investigated and compared in this thesis. It is observed that for large problems, the preconditioned iterative methods for solving the resulting system of equations are more desirable when compared with direct methods. As a future work, devising a specific preconditioner from the context of the given PML formulation will be valuable when large problems with complex geometries are encountered.

REFERENCES

- [1] Sadiku, Matthew NO. Numerical techniques in electromagnetics. CRC press, 2000.
- [2] Basic Electromagnetic Theory, D.T. Paris and F.K. Hurd, McGraw-Hill, New York, 1969, p. 166.
- [3] M. Kuzuoglu, and R. Mittra, "A systematic study of perfectly matched absorbers," *Frontiers in Electromagnetics*, IEEE Press, 2000.
- [4] J. P. Berenger, "A Perfectly matched layer for the absorption of electromagnetic waves," *Journal of Computational Physics*, vol. 114, pp.185-200, 1994.
- [5] Z. S. Sacks, D. M. Kingsland, R. Lee, and J. F. Lee, "A perfectly matched anisotropic absorber for use as an absorbing boundary condition," *IEEE Transactions on Antennas Propagation*, vol. 43, pp. 1460-1463, 1995.
- [6] D. H. Werner and R. Mittra, "New field scaling interpretation of Berenger's PML and its comparison to other PML formulations," *Microwave and Optical Technology Letters*, vol. 16, pp. 103-106, 1997.
- [7] C. W. Steele, A spectral method for field computation, *IEEE Transactions on Magnetics*, vol. mag-19, no. 6, November, 1983.
- [8] O. Z. Mehdizadeh and M. Paraschivoiu, "Investigation of a two-dimensional spectral element method for Helmholtz's equation," *Journal. of Computational. Phys.*,vol. 189, pp. 111–129, 2003.
- [9] J. Lee, T. Xiao, and Q. H. Liu, "A 3-D spectral-element method using mixed-order curl conforming vector basis functions for electromagnetic fields," *IEEE Transactions On Microwave Theory and Techniques*, vol. 54-1, pp. 437-444, January 2006.
- [10] J. Lee and Q. H. Liu, "A 3-D spectral-element time-domain method for electromagnetic simulation," *IEEE Trans. On Microwave Theory and Technique*, vol. 55-5, pp. 983-991, May 2007.
- [11] J. Lee, J. Chen, and Q. H. Liu, "A 3-D Discontinuous Spectral Element Time-Domain Method for Maxwell's Equations", *IEEE Transactions on Antennas and Propagation*, vol. 57, no. 9, September, 2009.

- [12] A High-Precision Integration Scheme for the Spectral-Element Time-Domain Method in Electromagnetic Simulation”, IEEE Transactions on Antennas and Propagation, vol. 57, no. 10, October 2009.
- [13] Y. Botros, J. Volakis, Preconditioned generalized minimal residual iterative scheme for perfectly matched layer terminated applications, Microwave and Guided Wave Letters, IEEE 9, 1999.
- [14] Shin, Wonseok, and Shanhui Fan. "Choice of the perfectly matched layer boundary condition for frequency-domain Maxwell's equations solvers." Journal of Computational Physics 231. No. 8, 2012.
- [15] A. Heifetz, S-C. Kong, A. V. Sahakian, A. Taflove, and V. Backman, "Photonic nanojets," J. Comput. Theor. Nanosci. 6, 1979–1992, 2009.
- [16] A. V. Itagi and W. A. Challener, "Optics of photonic nanojets," Journal of Optics Society, vol. 22, No. 12, 2005.
- [17] David B. Davidson, Computational electromagnetics for RF and Microwave Engineering, 2nd edition, Cambridge university press, 2011.
- [18] C.A. Balanis, Advanced Engineering Electromagnetics. John Wiley & Sons, 1989.
- [19] A. Taflove and S. C. Hagness, Computational Electrodynamics: The Finite-Difference Time-Domain Method. Norwood, MA: Artech, 2000.
- [20] Halpern, Laurence, and Lloyd N. Trefethen. "Wide-angle one-way wave equations." The Journal of the Acoustical Society of America 84.4 (1988): 1397-1404.
- [21] Bettess, Peter. "Infinite elements." International Journal for Numerical Methods in Engineering 11.1 (1977): 53-64.
- [22] Towers, M. S., Andrew McCowen, and John AR Macnab. "Electromagnetic scattering from an arbitrary, inhomogeneous 2-D object-a finite and infinite element solution." Antennas and Propagation, IEEE Transactions on 41.6 (1993): 770-777.
- [23] Bettess, Peter. "More on infinite elements." International Journal for Numerical Methods in Engineering 15.11 (1980): 1613-1626.
- [24] A.T. Patera. A spectral element method for fluid dynamics: Laminar flow in a channel expansion. Journal of Computational Physics, 54:468–488, 1984.
- [25] Deville, Michel O., Paul F. Fischer, and Ernest H. Mund, eds. High-order methods for incompressible fluid flow. Vol. 9. Cambridge University Press, 2002.

- [26] Karniadakis, George, and Spencer Sherwin. Spectral/hp element methods for computational fluid dynamics. Oxford University Press, 2013.
- [27] S. J. Hesthaven, S. Gottlieb, and D. Gottlieb, Spectral methods for time-dependent problems, Cambridge University Press, 2007.
- [28] O. Deville, F. P. Fischer, and E. Mund, High-order methods for incompressible fluid flow, Vol. 9. Cambridge University Press, 2002.
- [29] J. W. Gordon, and A. C. Hall, "Transfinite element methods: blending-function interpolation over arbitrary curved element domains," Numer. Math, vol. 21.2, pp. 109-129, 1973.
- [30] D. W. Pepper and J. C. Heinrich, Finite Element Methods: Basic Concepts and Applications, 1st ed. USA: CRC Press, 1992, ch. 4, pp. 56.
- [31] M. Picasso, "An adaptive algorithm for the Stokes problem using continuous, piecewise linear stabilized finite elements and meshes with high aspect ratio", Applied Numerical Mathematics, vol. 54, pp. 470–490, August, 2005.
- [32] V. Prachitham1, M. Picasso, and M. Gijs, "Adaptive finite elements with large aspect ratio for mass transport in electroosmosis and pressure-driven microflows", International Journal of Numerical Methods in Fluids", vol. 63, pp. 1005-1030, 2010.
- [33] S. Dong and Z. Yosibash, "A parallel spectral element method for dynamic three-dimensional nonlinear elasticity problems", Journal of Computers and Structures, vol. 87, pp. 59-72, 2009.
- [34] D. Rh. Gwynllyw and T. N. Phillips, "Iterative Methods with Dynamic Preconditioning for Moving Spectral Element Technique Applied to the Journal Bearing Problem", Proceedings of the Third International Conference on Spectral and High Order Methods, pp. 277-286, 1996.
- [35] Barrett, Richard, et al. Templates for the solution of linear systems: building blocks for iterative methods. Vol. 43. Siam, 1994.
- [36] Saad, Yousef. Iterative methods for sparse linear systems. Siam, 2003.
- [37] Lanczos, Cornelius, Solution of systems of linear equations by minimized iterations, Journal of Research of the National Bureau of Standards, 49 (1952), pp. 33–53.
- [38] R. FLETCHER, Conjugate gradient methods for indefinite systems, in Proceedings of the Dundee Biennial Conference on Numerical Analysis 1974, G. A. Watson, ed., New York, 1975, Springer Verlag, pp. 73–89.
- [39] W. Kahan, Gauss Seidel methods of solving large systems of linear equations,

PhD thesis, University of Toronto, 1958.

[40] Yousef Saad, and Martin H. Schultz, "GMRES: A Generalized Minimal Residual Algorithm for Solving Nonsymmetric Linear Systems", *SIAM J. Sci. Stat. Comput.* Vol. 7, No. 3, July 1986.

[41] Z. Chen, A. Taflove, and V. Backman, "Photonic nanojet enhancement of backscattering of light by nanoparticles: a potential novel visible-light ultramicroscopy technique," *Opt. Express* 12, 1214-1220, 2004.

[42] S. Lecler, Y. Takakura, and P. Meyrueis, "Properties of a three-dimensional photonic jet," *Opt. Lett.* 30(19), 2641–2643, 2005.

[43] A. Devilez, B. Stout, N. Bonod, and E. Popov, "Spectral analysis of three-dimensional photonic jets," *Opt. Express* 16, 14200-14212, 2008.

[44] P. Ferrand, J. Wenger, A. Devilez, M. Pianta, B. Stout, N. Bonod, E. Popov, and H. Rigneault, "Direct imaging of photonic nanojets," *Opt. Express* 16, 6930-6940, 2008.

[45] M.-S. Kim, T. Scharf, S. Mühlig, C. Rockstuhl, and H. P. Herzig, "Engineering photonic nanojets," *Opt. Express* 19, 10206-10220, 2011.

[46] Z. Wang, W. Guo, L. Li, B. Luk'yanchuk, A. Khan, Z. Liu, Z. Chen, and M. Hong, "Optical virtual imaging at 50 nm lateral resolution with a white-light nanoscope," *Nature Commun.* 2, 218, 2011.

[47] V. R. Dantham, P. B. Bisht, C. K. R. Namboodiri, "Enhancement of Raman scattering by two orders of magnitude using photonic nanojet of a microsphere," *J. Appl. Phys.* 109, 103103, 2011.

[48] S.-C. Kong, A. Sahakian, A. Taflove, and V. Backman, "Photonic nanojet-enabled optical data storage," *Opt. Express* 16, 13713-13719, 2008.

[49] A. M. Kapitonov and V. N. Astratov, "Observation of nanojet-induced modes with small propagation losses in chains of coupled spherical cavities," *Opt. Lett.* 32, 409-411, 2007.

[50] Özlem Özgün, "Finite Element Modeling of Electromagnetic Radiation/Scattering Problems by Domain Decomposition,". Diss. Middle East Technical University, 2007.

VITA

PERSONAL INFORMATION Name, Surname: Ibrahim, Mahariq Email: ibmahariq@gmail.com Nationality: Palestinian. Date and Place of Birth: 5 Feb 1980, Alsamoo, Palestine		
EXPERIENCE <ol style="list-style-type: none"> 1- Teaching Assistant in Palestine Polytechnic University (PPU) from 10/ 2003 –9/ 2005 2- Expert in Finite Element Analysis / METU-2006-2009 3- Machines design and analysis (Brushless DC motors, SR Motor, Induction motors) / METU 2008-2011. 4- Course Assistant: Finite Element Method, Numerical Solutions of PDEs / METU 2012-2014. 		
EDUCATION		BSc1(998-2003)
Major: Industrial Automation Engineering. Dept. of Electrical & Computer Eng. Palestine Polytechnic University BSc Project: 7-Level Diode-Clamped, PWM-BASED 3-ph Inverter Using PC as a controller.		86.2% with distinction
		MSc (2006-2009)
Electrical machines and Powerelectronics – METU Thesis: A NORMALIZED SET OF FORCE AND PERMEANCE DATA FOR DOUBLY-SALIENT MAGNETIC GEOMETRIES BY FEM		3.1/4.0
		PhD
After he passed PhD qualification exam in both major (electrical machines & powerelectronics) and minor (Power systems) (14 courses are covered), Mahariq didn't continue because of his supervisor for supervision reasons. METU		3.8/4.0 EE
Mahariq then switched to the department of Engineering Sciences He worked in the field of <u>Computational Electromagnetics</u> supervised by Prof. Dr. <u>Mustafa Kuzuoğlu</u> and Prof. Dr. Hakan Tarman. Thesis Topic: Two Dimensional Modelling of Electromagnetic Scattering and Radiation Problems by Spectral Element Method. Graduation Date: 14 July 2014		3.79/4.0 ES
PUBLICATIONS		<i>(additional manuscripts are under preparation in the field computational electromagnetics and photonics)</i>
<ul style="list-style-type: none"> • I. Mahariq, H. I. Tarman, and M. Kuzuoğlu, "On the Accuracy of Spectral Element Method in Electromagnetic Scattering Problems," International Journal of Computer Theory and Engineering vol. 6, no. 6, pp. 495-499, 2014. • I. Mahariq, M. Kuzuoğlu, and H. I. Tarman, "On the Attenuation of Perfectly Matched Layer in Electromagnetic Scattering Problems with 		

Spectral Element Method”, Applied Computational Electromagnetic Society Journal, under review.

- I. Mahariq, H. Kurt, H. I. Tarman, and M. Kuzuoğlu, “Photonic Nanojet Analysis by Spectral Element Method”, IEEE Photonics Journal, reviewed.
- I. Mahariq, and I. Arpacı. "Challenges and Opportunities in Nuclear Energy: Promising Option in Turkey?" International Journal of Electrical, Robotics, Electronics and Communications Engineering Vol:7 No:2, 2013.
- I. Mahariq, “A Set of Force and Permeance Data for Switched Reluctance Machines by Finite Element Method”, 3rd International conference on nuclear and renewable energy resources, Istanbul, May 2012.
- I. Mahariq, “Time Relativity from the view of Quran and Special Relativity”, 3rd International Conference on the Scientific View of Quran, Morocco, Tetouan Sep 2010.

Mahariq received TUBITAK scholarship in 2010 for his PhD studies.
Mahariq received ISDB scholarship during his MSc program.